OCEAN DYNAMICS SOUTH SHORE OF OAHU, HAWAI'I: FROM
MEAN CIRCULATION TO NEAR-INERTIAL WAVES AND
SUBMESOSCALE.

A DISSERTATION SUBMITTED TO THE
GRADUATE DIVISION OF THE
UNIVERSITY OF HAWAI'I AT MĀNOA
IN PARTIAL FULFILLMENT OF THE
REQUIREMENTS FOR THE DEGREE OF

DOCTOR OF PHILOSOPHY

IN

OCEANOGRAPHY

AUGUST 2018

By

Alma Carolina Castillo Trujillo

Dissertation Committee:

Pierre Flament, Chairperson
Brian Powell
Oceana Francis
Mark Merrifeld
Jim Potemra

We certify that we have read this dissertation and that, in our opinion, it is satisfactory in scope and quality as a dissertation for the degree of Doctor of Philosophy in Oceanography.

DISSERTATION
COMMITTEE

_____

Chairperson

_____

_____

_____

_____

Para todo mal el mar,

para todo bien, también,

ACKNOWLEDGMENTS

ABSTRACT

Recent analytical and numerical studies have shown that submesoscale processes (approximately order one Rossby and Richardson number) in the ocean are important contributors to the fluxes of potential vorticity and are vital for the transfer of energy from the larger mesoscale to the smaller scales. My doctoral dissertation examines submesoscale processes and their interactions with other motions using ocean surface velocities observed from High Frequency Doppler Radar (HFR) at a ~1.5 km resolution alongside a Regional Ocean General Circulation Model (ROMS) producing ocean velocities at a ~4 km spatial resolution.

In the first part of the dissertation I examine vortical motions. I focused on deriving the surface vorticity balance south of the island of Oahu, Hawaii using the HFR surface ocean velocities and ROMS product. The first order terms in the balance were advection of vorticity, vortex stretching and a residual which included the wind stress curl and the divergence of eddy fluxes. A depth integrated vorticity balance was also made assuming an equivalent barotropic flow resulting in bottom pressure torque as a first order term in areas of shallow topography. It was also found that this shallow topography modified the canonical westward Hawaiian Lee Current flowing south of the Hawaiian Archipelago.

The second part describes the spatial variations of surface Near Inertial Oscillations (NIOs) observed in the presence of large Rossby number submesoscale flows. Sea Surface Height (SSH) observations were used alongside HFR and ROMS to study the NIOs spatial variability and frequency characteristics in the presence of the submesoscale (HFR and ROMS) and mesoscale flows (SSH). It was found that the frequency and wavelength of the NIOs are modified by the high Rossby number submesoscale flow. The amplitudes of the NIOs, on the contrary, are modified by the submesoscale flow. In particular, the small-scale gradient of vorticity and divergence fields derived by the HFR surface velocities appear as lead contributors to the damping and growth of the NIOs. These results have implications to the global energy budget of the ocean since the decay and growth of surface NIOs contributes to the generation of internal waves and mixing in the interior. Furthermore, the

estimated zonal NIO's wavelength appears impacted by the coast as well as the Laplacian of the vorticity. An energy budget for the NIO taking into account the influence by the mean background flow is also computed.

The third part of this dissertation describes the submesoscale process at scales of 5 to 40 km. Submesoscale positive vorticity filaments are routinely observed from the southwest coast of Oahu. These filaments sometimes roll into vortices with diameters of ∼30 km and Rossby numbers $O(1)$. They are generated by barotropic shear instabilities and are amplified by the shear of the mean background flow. It is suggested that frontogenesis and PV by bottom drag formed the necessary shear to produce the instability. Kinetic energy wavenumber spectrum estimates at scales between 5 to 40 km are consistent with isotropic interior quasigeostrophic turbulence. Ageostrophic motions account for a part of this variance, in particular, at scales of less than 10 km. There is a slight seasonality in the spectrum estimates, with larger variance in winter and spring due to the observed submesoscale eddies. Other physical regimes may be part of this variability, future studies with high resolution models and three dimensional observations around the Hawaiian archipelago are recommended.

TABLE OF CONTENTS

x

LIST OF TABLES

LIST OF FIGURES

xiv

xviii

CHAPTER 1
INTRODUCTION

The ocean circulation encompasses a wide range of scales. The most energetic flows are eddies with horizontal scales of a few hundred kilometers (mesoscale). These mesoscale eddies are well understood and have been routinely studied with satellite observations and global numerical models. These motions are mostly anisotropic with vertical velocities much smaller than their horizontal velocities because of the earth rotation and stable dense stratification suppressing vertical motions.

Recent numerical and observational studies have shown a very dynamical eddy field at scales between 1 to 100 km, which drives vertical velocities one or two orders of magnitude than the 1 m/day associated with the divergence of the mesoscale flow. These vertical velocities generate fluxes of physical and chemical tracers between the mixed layer and the ocean interior which are important for to the biological production at the ocean surface. This regime usually called the submesoscale, has recently drawn much attention from the perspective of its role in the turbulent cascade of energy (McWilliams 2016).

Submesoscale features can be observed as filaments, fronts and eddies. They are characterized by Rossby number $O(1)$ and horizontal spatial scales smaller than the first baroclinic deformation radius (Thomas et al. 2008; Capet et al. 2008). The dynamics of submesoscale processes in the surface mixed layer have been explained by frontogenesis (Capet et al. 2008; Gula et al. 2014), baroclinic instabilities (Callies et al. 2015) and mesoscale straining (Shcherbina et al. 2013). Analysis and interpretation of submesoscale currents has mostly been approached in an open-ocean context where submesoscale currents most commonly reside.

Submesoscale observations are sparse because in situ measurements have a limited ability to observe submesoscale processes. At present, high-resolution numerical models provide the most feasible route for explanation of submesoscale dynamics in a variety of oceanographic settings. However; High Frequency-doppler Radars (HFR), geostationary color imagery

and the future SWOT, are instruments that can be used to realistically investigate the submesoscale flow.

The ocean dynamics around the Hawaiian islands are characterized by a combination of coastal and open-ocean processes. Coastal circulation around the islands is typically characterized by complex oceanic responses to wind stress, tides, heat fluxes and bathymetry conditions (e.g., Chavanne et al., 2010). The canonical circulation around the islands is described by the westward Hawaiian Lee current (HLC) south of the islands and the westward North Hawaii Ridge Current (NHRC) flowing north of the archipelago. Mesoscale eddies have been routinely observed by satellite observations (Yoshida et al. 2011), numerical models (Calil et al. 2008) and drifters (Victoria Futch, personal communication). They are generated by the wind stress curl in the lee of islands (Chavanne et al. 2002) and Von Karman instabilities off the Big Island of Hawaii. These eddies generally drift westward at approximately the first baroclinic Rossby wave speed and contribute to the canonical circulation. The only submesoscale study for Oahu was done by Chavanne et al. (2010) using 3 months of HFR surface velocities. It investigated the interaction between a submesoscale eddy of ∼10 km and a front off the west coast of Oahu.

In this study, two years of HFRs measuring surface currents at resolutions of ∼1.5 km and one hour are used to study the mesoscale to submesoscale surface circulation off the south shore of Oahu, Hawaii. This integrated analysis using maps of concurrently observed HFR surface currents, gliders, satellite and wind measurements can provide insights for pure observational based submesoscale process studies. Furthermore, two years of model data around the Hawaiian Island are used to compare with the observations.

The purpose of this study is twofold; to characterize the submesoscale regime around an island and highlight its potential importance in contribution to horizontal and vertical material, and to explore the governing ocean dynamics of the submesoscale currents south shore of Oahu, Hawaii at different spatial and temporal scales. This thesis is organized as follows; Chapter 2 explores the mean circulation and its interaction with local topography. Chapter 3 investigates the spatial and temporal variability of the near inertial oscillations

and Chapter 4 describes the submesoscale flow and its interaction with the lower frequency regime. Chapter 5 compares and validates observations and model.

CHAPTER 2
VORTICITY BALANCE SOUTH SHORE OF OAHU HAWAII DERIVED BY HIGH-FREQUENCY RADIO DOPPLER CURRENT OBSERVATIONS

2.1   Introduction

Among ocean current measurements, only high-frequency radio (HFR) Doppler current meters are able to map currents at both high spatial resolution (on the order of the km), and temporal resolution (on the order of an hour), therefore they can uniquely estimate the momentum and vorticity balances of the upper ocean. Estimating the momentum balance requires knowing the pressure field either through hydrography or altimetry, both which cannot sample at the same high resolutions as the HFRs. We can, however, estimate the vorticity balance without the need for the pressure gradients using only HFRs.

In this study, our objective is to investigate how the mean surface vorticity balance may be estimated and analyzed from an array of HFRs. We will first review the theoretical derivation of the surface vorticity balance and its expression in terms of measurable quantities. We then will apply the concept to an area where the vorticity forcing signal is known to be strong; south of the island of Oahu, Hawaii (Chavanne et al. 2010b).

The Hawaiian Islands are a prime region to study the vorticity balance since the mountainous islands present a barrier to the trade winds generating wind stress curl (Chavanne et al. 2002) which in turn produces cyclonic and anticyclonic eddies. South of the archipelago, (Yoshida et al. 2011) found the mesoscale variability induced not only by the wind stress curl but by the shear between the Hawaiian Lee Current (HLC) and the North Equatorial Current (NEC). The NEC bifurcates in to the North Hawaiian Ridge Current to the north and the HLC to the south of the islands. Furthermore, the HLC is seasonally modified by the trade winds and south westerly winds (Castillo-Trujillo 2014). The Hawaiian archipelago is a key region for generating mesoscale eddies in the western Pacific Ocean, a previous model study of the vorticity balance study around the Hawaiian

Islands (Azevedo Correia de Souza et al. 2015) showed that wind stress curl can produce enough advection of vorticity to enhance the canonical circulation around the Hawaiian archipelago and thus modify the north-Pacific ocean circulation.

To account for this surface frictional forcing, the vorticity balance residual will be compared to the wind stress curl from an assimilative atmospheric model in conjunction with the surface mixed layer depth from an ocean general circulation model (GCM).

The paper will be presented as follow; Section 2 describes the theoretical background. Data and methods are described in section 3. The HFR observations are described in section 4 and the surface vorticity balance is described in section 5. The results are discussed in section 6 and summarized in section 7.

2.2 Theoretical Background

The surface quasi-geostrophic vorticity balance equation involves quantities directly measurable by the HFR. Assuming hydrostatic balance and incompressibility the horizontal momentum equation is:

$$\partial_t \mathbf{u} + \mathbf{u} \cdot \nabla \mathbf{u} + f \times \mathbf{u} = \frac{1}{\rho} \nabla p + \mathbf{F} \tag{2.1}$$

in which $\mathbf{u} = [u(x,y), v(x,y)]$, p is pressure, ρ is density, ∇ is the two-dimensional del operator $(\partial/\partial x, \partial/\partial y)$ and $\mathbf{F}$ contains the forcing and dissipative terms. Taking the horizontal curl of equation (2.1) yields the surface vorticity conservation equation in which pressure effects are no longer explicit:

$$\partial_t \zeta + \mathbf{u} \cdot \nabla(\zeta + f) + (\zeta + f)\nabla \cdot \mathbf{u} = \nabla \times \mathbf{F} \tag{2.2}$$

On the L.H.S of equation 2.2 the first term is the rate of change of relative vorticity, the second and third term are the advection of relative and planetary vorticity ($\beta = df/dy$) and the fourth term is the vortex stretching. The $\nabla \times \mathbf{F}$ acts as the sources and sinks of vorticity due to external forcing and dissipation.

HFRs measure currents over a thin layer of depth $H_R \sim 0.7$ m (at 16 MHz) (Stewart and Joy 1974; Gurgel et al. 1999a; Röhrs et al. 2015). While this depth is ill-defined and there are no closed theoretical expressions for it, it is much smaller than the surface mixed layer depth, and thus the horizontal momentum and vorticity terms in (2) will be assumed constant within H_R. Neglected terms in (2) which can not be directly calculated by HFR observations include vorticity tilting and lateral stress divergences arising from the curl of the vertical momentum of advection.

2.3   Data and Methods

2.3.1   HFR surface currents

Two WERA HFRs (Gurgel et al. 1999a,b), with a range of 100 km and a range-resolution of 1.5 km, have been deployed on the south shore of Oahu, Hawaii from September 2010 to September 2012 (labelled as KAL and KOK as shown in Figure 2.1). A description of the principles of the WERA radars can be found in Gurgel et al. (1999a). The configuration of the radars (frequency 16 MHz, bandwidth 100 kHz) and the processing techniques were identical to those detailed by Chavanne et al. (2007, 2010a). The instrument setting and radar noise are discussed in Appendix A.

Figure 2.1a shows the location of the two radars in Kalaeloa (KAL, 21° 18N, 158° 5W) and Koko Head (KOK, 21° 26N, 157° 42W), covering the 670 m deep Kaiwi channel, and the shallow 50 m deep Penguin Bank. The two-year mean surface currents are overlaid over the color-coded mean vorticity and divergence (Figure 2.1a and 1b).

Figure 2.2a shows the rotary power spectra of velocity averaged over the entire domain. Similar to the results of Chavanne et al. (2010b), the slope of the continuum energy at superinertial frequencies is representative of the internal wave spectrum, with no rotary asymmetry. The diurnal and semidiurnal tides, and their harmonics, dominate the super-inertial band. In contrast, clockwise energy is larger than counterclockwise in the near-inertial band extending down to $0.7f$, the broadening of which reflects the influence of local

6

vorticity on the inertial frequency (Kunze 1985; Weller 1982). In the subinertial band of mesoscale motions, spectral energy follows the typical slope of about $\sim$-5/3 (Vallis (2006), p380).

Figure 2.2b shows the corresponding power spectra of divergence $\frac{\partial u}{\partial x} + \frac{\partial v}{\partial y}$ and local vorticity $\frac{\partial v}{\partial x} - \frac{\partial u}{\partial y}$ averaged over the entire domain. In the inertial and superinertial bands, divergence and vorticity have similar magnitudes. There is no distinct near-inertial peak, since inertial motions are spatially homogeneous to first order, responding mostly to local wind forcing. Below 0.7f, the magnitude of vorticity progressively overwhelms divergence, as expected in flows increasing in geostrophic balance at increasingly longer periods.

Since this study is focused on the mean surface vorticity balance, temporal filtering of the HFR time series is essential to separate the mean motions from the higher frequency oscillations. The filtering was performed in two steps. First, the tidal harmonics were removed using the t_tide algorithms (Pawlowicz et al. 2002) . Secondly, a butterworth low-pass finite impulse response filter with a cut-off frequency of 0.33 cpd (T = 3 days) was used to extract the subinertial mesoscale flow, thus rejecting inertial oscillations, and high-frequency waves.

All quantities (velocity, velocity gradients and mean and eddy vorticity terms) were computed from these low-passed currents. The L.H.S of equation 2.2 can be entirely calculated from these velocity and vorticity gradients while the R.H.S can be estimated as a residual from the L.H.S of equation 2.3 or calculated explicitly from the atmospheric model and GCM product as it will be shown in section 5.3.

Surface velocity gradients are typically in the $O(10^{-8} \text{ s}^{-1})$ while relative vorticity gradients are in the $O(10^{-12} \text{ m s}^{-1})$. Both velocity and vorticity gradients are highly variable throughout the HFR spatial domain. Values increase up to 10 times the typical values close to the coast and away from the HFR coverage due to the GDOP (Appendix A and B).

2.3.2 Wind Measurements

While wind stress is the primary upper ocean forcing, the coarse resolutions of satellite winds (ASCAT, 25 km) and global model winds (NCEP-NARR, 32 km) do not usefully match the HFR surface velocity observations. In contrast, the network of land-based meteorological stations and ocean buoys is also too sparse to calculate gradients. Therefore, a local implementation of the Weather Research Forecast (WRF) model (Tu and Chen 2011), assimilating data from satellite, aircrafts and buoys, will be used to provide the surface wind field at spatio-temporal resolutions matching the radar grid.

The HNL airport daily wind observations and the WRF wind-model grid point closest to the HNL station are significantly correlated with an r-value of 0.60. WRF Wind stress is computed using Large and Pond (1981), standard methods. Figure 2.1d shows the 2-year mean surface wind stress (September 2010 through September 2011; same as HFR data), overlaid over the color-coded mean wind stress curl. The wind stress field shows the dominance of the northeasterly tradewinds, while the wind stress curl field reveals the influence of mountainous island topography. In particular, positive wind stress curl yielding upward Ekman pumping (cyclone-generating) is observed over Penguin Bank and the Kaiwi channel, while negative wind stress curl yielding downward Ekman pumping (anticyclone-generating) is observed in the south-west coast of Oahu (Chavanne et al. 2010b). This pattern is also reflected on the divergence field (shown on Figure 2.1b), where the two-year mean divergence is mostly positive (negative) where wind stress curl is negative (positive).

2.3.3 Ocean Model Surface Layer

The assimilative GCM is based on the Regional Ocean Modeling System (ROMS), a free-surface, hydrostatic, primitive equation model discretized with a terrain-following vertical coordinate system (Shchepetkin and McWilliams 2005). The assimilation system is based on previous work (Azevedo Correia de Souza et al. 2015; Janeković et al. 2013; Matthews et al. 2012; Powell et al. 2009). It uses four-dimensional variational (4D-Var) assimilation to integrate data from HFR radial currents, satellites, autonomous gliders, Argo drifters,

and other in-situ measurements. Barotropic forcing is from the Oregon State University TOPEX/Poseidon Global Inverse Solution (TPXO) tidal constituents, (Egbert and Erofeeva 2002) and the lateral forcing is provided by the coarser resolution global HYCOM. The surface forcing uses the high-resolution winds from the 1.5 km WRF atmospheric model described in sec. 3.2.

The model was run to overlap with the HFRs time series from September 2010 to September 2012 at 4 km resolution over a domain covering the Hawaiian Islands (-153° to -163° and 17° to 24°), with 32 terrain-following vertical levels: 9 levels span the upper 200 m in deep water, with more levels near-surface as the slope ascends towards the islands. The model output provides estimates of the temperature, salinity, density, currents, and tides at a 3-hour temporal resolution. The mixed layer depth, most important for our objective, was estimated as the depth where density varies 0.125 kg m^{-3} from the surface.

Figure 2.1d shows the spatial distribution of the 2-year temporal mean of mixed layer depth (H_s). Note the large spatial variations of H_s over the domain, ranging from ∼35 m just West of Penguin Bank, to ∼55 m south west coast of Oahu. These variations are, in part, the response of the ocean to the patterns of wind stress curl (Figure 2.1c), through one-dimensional mixed-layer deepening and Ekman transport divergence, and in part due to the geostrophic signature of the mean currents, which may not be solely locally wind-driven.

2.4   Description of HFRs observations

Figure 2.1a shows the time-averaged HFR surface velocities from 2010 to 2012; a westward drift is observed, intensifying southward away from the island, with typical speeds of 25 cm s^{-1}, corresponding to the local expression of the HLC (Lumpkin 1998; Lumpkin and Flament 2013). The time-mean relative vorticity has typical values in the $O(10^{-6}$ s$^{-1})$, reflecting the topography with positive (cyclonic) vorticity ∼+0.25f immediately west of Penguin Bank, and negative (anticyclonic) vorticity ∼-0.26f closer to the coast of Oahu. The total ζ values over the two-year period are slightly more negative (53%) than positive (47%). There is a slight preference for positive ζ (57%) in the Kaiwi channel, while the

opposite is true for Penguin Bank with 65% of the total vorticity values being negative vorticity.

We chose two areas of approximately 20 km^2 (Figure 2.1d) where GDOP is low (Appendix A) such that each region is representative of i) an area of $\sim$600 m depth with mean negative wind stress curl (region A) and ii) a shallow bank $\sim$200 m depth with mean positive wind stress curl (region B). Northeasterly trade-winds are observed throughout most the year with south-west wind events in winter and spring(Figure 2.3c and 3d). As shown by Castillo-Trujillo (2014), during southwesterly winds, the surface currents on region B exhibit frequent eastward reversals while during northeasterly winds the surface current is mostly north-west (Figure 2.3b). On the other hand on region A (Figure 2.3a) periodical south-west current reversals are seen throughout the time record which do not seem related to any wind event but were also seen in Chavanne et al. (2010b) HFR observations west coast of Oahu.

2.5   Surface vorticity balance

2.5.1   Low frequency time-varying balance

The time-varying balance in region A is a combination of advection of vorticity, vortex stretching and its residual (Figure 2.4a), while in region B (Figure 2.4b) the balance is mostly composed of vortex stretching and residual and to a lesser extent to advection of vorticity. The residual in region A occurs because either stretching and advection of vorticity are out phase when of opposite sign or because stretching mostly dominates compared to advection of vorticity. Except from March to June 2012 when advection of vorticity is larger than vortex stretching. In contrast, in region B the residual occurs because the strong stretching is opposed by the residual and sometimes weak advection. The advection of planetary vorticity is an order of magnitude smaller and does not contribute to the balance in any of the areas. In both regions, typical values of advection of vorticity and vortex stretching are around 0.5×10^{-9} s^{-2} with maximum values at 1×10^{-9} s^{-2}.

Although the tendency term $\frac{\partial \zeta}{\partial t}$ is two orders of magnitude smaller than the rest of the terms in equation (2.2) (Figure 2.4c), variations of $\frac{\partial \zeta}{\partial t}$ are generated by changes in time over different leading-order terms. For example, in June 2011 (region A) advection of vorticity and vortex stretching contribute to the term while in March 2012 (Region B) vortex stretching and the residual are the main contributors.

Eddy Kinetic Energy (EKE) and relative vorticity peaks stand out through out the time series with events lasting between 30 to 45 days (Figure 2.4d and 2.4e). The largest EKE events are found in Spring 2012 with values of up to ~ 0.10 m^{2}s^{-2}. This event is also seen as an increase in positive relative vorticity with values of around $1f$. Region A has the largest relative vorticity values reaching up to $1f$ while Region B values are never larger than $\pm 0.5f$. Only in region A, a slight seasonality is observed in relative vorticity where large positive events are seen in winter months from December to March.

2.5.2 Time-mean balance

To quantify the effect of eddy vorticity forcing on the mean flow, the standard Reynolds decomposition of velocity into a time mean and time-dependent eddy component is applied as $\mathbf{u} = \overline{\mathbf{u}} + \mathbf{u}'$ where $\overline{\mathbf{u}}$ is the two-year time-mean and $\mathbf{u}'$ are the deviations from the mean. The relative advection of vorticity $\overline{\mathbf{u}} \cdot \nabla \overline{\zeta}$ and vortex stretching $(\overline{\zeta} + f)\nabla \cdot \overline{\mathbf{u}}$ are separated from the advection of eddy vorticity, $\overline{\mathbf{u}' \cdot \nabla \zeta'}$ and stretching of eddy vorticity, $\overline{\zeta' \nabla \cdot \mathbf{u}'}$. To quantify these Reynolds stresses and quantify its contribution to to the mean balance they are combined as the divergence of the eddy flux of relative vorticity, $\nabla \cdot \overline{\mathbf{u}'\zeta'}$. Equation 2.2 becomes:

$$\overline{\mathbf{u}} \cdot \nabla \overline{\zeta} + (\overline{\zeta} + f)\nabla \cdot \overline{\mathbf{u}} = \nabla \times \overline{\mathbf{F}} - \nabla \cdot \overline{\zeta' \mathbf{u}'} \tag{2.3}$$

Equation 2.3 expresses that in the absence of dissipation and mixing into the deeper layers, mean advection of relative vorticity is balanced by mean vortex stretching, divergence of the eddy flux of relative vorticity, and an external forcing. The advection of planetary vorticity and the tendency term are negligible since they are two orders of magnitude smaller

than the leading-order terms.

The HFR derived terms in equation 2.3 are plotted on Figure 2.5; there is an anti-correlation between mean advection (Figure 2.5a) and mean vortex stretching (Figure 2.5b) of vorticity with negative (positive) values of advection of vorticity in the west (east) of the HFR domain. In certain areas, however, close to Penguin Bank and north of the Kaiwi Channel, advection does not seem capable of inducing the observed vortex stretching, indicating an external source of vorticity beside advection of PV anomalies.

The residual from $\overline{\mathbf{u}} \cdot \nabla \overline{\zeta}$ and $(\overline{\zeta} + f)\nabla \cdot \overline{\mathbf{u}}$ (denoted as R_1 in Figure 2.5c) resembles the vortex stretching pattern but is only about one third of its size, except where vortex stretching was larger than advection of vorticity as in the Penguin Bank area.

Figure 2.5g shows the divergence of eddy flux of relative vorticity. It mostly follows the leading order terms pattern with positive (negative) values in the north-west (south-east) of the HFR spatial domain and its main contributor is the advection of eddy vorticity (Figure 2.5e). This indicates that in addition to advection of vorticity, the eddy forcing could have cause compression of the vortex stretching term in the north-west corner of the HFR spatial domain suggesting motions such as eddies can play a role in mean vorticity budget.

2.5.3 Vorticity balance integrated over the mixed layer depth

If the dominant external forcing in the mean surface vorticity balance is the vertical turbulent flux of horizontal momentum, with wind stress τ as the surface boundary condition, the forcing term in equation 2.3 becomes $\frac{1}{\rho}\nabla \times \overline{\tau_z}$. Integrating the forcing term over a mixed layer depth H_s, below which the turbulent stresses are neglected (Stern 1965; Price et al. 1986) and assuming the rest of the terms in equation 2.3 are constant yields:

$$\overline{\mathbf{u}} \cdot \nabla \overline{\zeta} + (\overline{\zeta} + f)\nabla \cdot \overline{\mathbf{u}} = \frac{1}{\rho \overline{H_s}}\nabla \times \overline{\tau_s} - \nabla \cdot \overline{\zeta' \mathbf{u'}} \tag{2.4}$$

where τ_s is wind stress at the surface. $\nabla \times \overline{\mathbf{F}}$ in equation 2.3 was calculated from the equation residual, in equation 2.4 it is explicitly computed from a combination of the WRF derived wind stress (Figure 2.1c) and the mixed layer depth H_s derived by the ROMS

product (Figure 2.1d).

The first term on the R.H.S of equation 2.4 (Figure 2.5d) shows the wind stress curl variations due to the island-shadow of the trade winds (Chavanne et al. 2002, 2010b) with positive values in most of the HFR domain, except in the north-west of the area near the coast. It is not expected that the residual from equation 2.3 will exactly resemble the modeled surface frictional forcing term since the residual includes all of the unquantified terms and noise and the spatial and temporal resolutions of both model (4 km, 3 hours) and HFR observations (1.5 km, 1 hour) are not the same. Nevertheless, the wind stress curl term has the same order of magnitude $O(10^{-10}$ s$^{-2})$ as advection of vorticity and vortex stretching, thus consistent with the typical values of the residual. In addition, over the Penguin Bank at $\sim-157.8^o$ there is an increase in positive wind stress curl in the modeled surface frictional forcing term (Figure 2.5d) that it is reflected in the positive advection of vorticity (Figure 2.5a) and negative vortex stretching (Figure 2.5b).

2.6 Discussions

2.6.1 Surface Vorticity Balance

The HFR surface vorticity budget (2.2) was estimated as a time-varying and time-mean balance revealing flow dynamics south of Oahu, Hawaii. The leading-order terms in the time-mean surface (Figure 2.4) are relative advection of vorticity, vortex stretching and the residual, and to a lesser extent the eddy forcing. The residual is leading-order, since it includes the unquantified terms such as wind stress curl and in certain areas of the HFR spatial domain, bottom pressure torque. The time-mean balance revealed certain aspects of the surface circulation around Oahu. In most of the HFR spatial domain there was an anti-correlation between advection of vorticity and vortex stretching (Figures 5a and 5b) suggesting surface circulation due to PV anomalies such as mesoscale eddies. In some areas, however, advection of vorticity did not produce vortex stretching of the correct sign, such as in Penguin Bank implicating forcing by bathymetry or higher-frequency eddy motions.

We will now discuss the implications of these terms in the mean vorticity budget by selecting two areas where the advection of vorticity and vortex stretching had a larger residual. The time-mean surface vorticity balance representative of regions of positive and negative wind stress curl south of Oahu, Hawaii (Figure 2.1d) is summarized in Figure 2.6. There are two different processes generating advection of vorticity over the HFR spatial domain since each region resulted in negative (region A) and positive (region B) mean values. In region A, advection of vorticity has a larger correlation with the residual ($r = 0.79$) compared to vortex stretching ($r = 0.51$) while in region B, vortex stretching has a positive and larger correlation ($r = 0.88$) with the residual compared to advection of vorticity ($r = -0.48$). This correlation difference could be attributed to the influence of the non-measured HFR vorticity terms such as dissipation of stress in Region A and bottom pressure torque in Region B where topography is shallow.

For both regions, if the residual is compared to the frictional forcing term derived from the combination of the WRF and ROMS products, values are the same of order of magnitude $O(10^{-10})$ s^{-2}, even with the differences between the HFRs, WRF and ROMS sampling and spatial smoothing.

Our analysis does not include dissipation of stress into the deeper layers, but in Azevedo Correia de Souza et al. (2015) vorticity balance, about 40% of the surface forcing is released to the deeper ocean through bottom stress. We can not quantify this term from HFR observations, but, for region A where bathymetry is about 600 m it can be estimated. If the residual includes the surface frictional forcing (calculated from the model is 0.50×10^{-10} s^{-2}) and the bottom stress, then it can be calculated as the difference between the model surface frictional forcing and the residual (1.06×10^{-10} s^{-2}), that is (0.50×10^{-10} s^{-2}), which is consistent with Azevedo Correia de Souza et al. (2015) results. With the inclusion of the eddy vorticity forcing in to the balance the residual will increase to 0.90×10^{-10} s^{-2}.

In region B; bathymetry is around 200 m and there is a positive source of advection of vorticity and eddy vorticity forcing that balance negative vortex stretching. Because the magnitude of the vortex stretching term is larger than advection of vorticity, the difference

14

could be attributed to bathymetric forcing and not to dissipation of stress to bottom layers such as suggested above for Region A. Thus, the residual will include not only the frictional forcing term but bottom pressure torque. This is can be quantified from Figure 2.6 as follows, if we assume the total residual R_2 including the eddy vorticity forcing (0.56×10^{-10} s^{-2}) includes bottom pressure torque, we can subtract the model surface frictional forcing term (0.59×10^{-10}) s^{-2}) from this total residual resulting in 0.02×10^{-10} s^{-2}. This closure of the vorticity budget could reveal the total residual not as surface frictional forcing but as bathymetric forcing. We will explore this further below.

The surface vorticity balance in this study does not necessarily represent the vorticity terms on a longer or larger spatio-temporal scale. Azevedo Correia de Souza et al. (2015) model results, although at a slightly lower spatial resolution (4 km), proposed the wind stress curl as a mechanism capable of producing advection of vorticity throughout the Hawaiian islands and even though they did not find vortex stretching as a first-order term, they did find -similar to us- that advection of vorticity and eddy vorticity forcing act as leading-order terms in the balance. In our study, the divergence of eddy fluxes of relative vorticity is about 30% smaller than mean advection of vorticity (Figure 2.6) and its inclusion in to the vorticity budget reduced the residual in Region B but not in Region A, precluding a clear examination of the term. Nevertheless, it is clear that it does affect the budget and a longer time series on a larger area could reduce this uncertainty.

2.6.2 Depth integrated vorticity balance in Penguin Bank

We will now further assess the influence of bottom pressure torque term in the vorticity budget, in particular in Region B where stretching of vorticity was larger than mean advection of vorticity. This can be estimated assuming the vertical distribution of the mean flow around the island of Oahu is governed by a function D(z) which is 1 at the surface and decays exponentially with depth as $D(z) = e^{z/H_o}$, where z is depth measured in meters from the ocean surface, positive upward, and H_o is the e-folding depth. Integrating equation 2.3 from the surface to the sea floor using D(z) and wind stress as the surface

frictional forcing leads to:

$$d_1\mathbf{u} \cdot \nabla\zeta + d_o(f + \zeta)\nabla \cdot \mathbf{u} = \frac{1}{\rho}\nabla \times \tau_s - \frac{1}{\rho}\nabla \times \tau_b + J(P_b, H) \qquad (2.5)$$

Where $d_o = \int_{-H}^{0} D(z')dz$ and $d_1 = \int_{-H}^{0} D^2(z')dz$. The subscript s refers to quantities at the surface, and b to those at the sea floor. The coefficients indicate that advection of vorticity will decay faster than vortex stretching with depth and their surface anti-correlation can be modified in the vertical as shown by Hughes (2005).

In shallow regions, the difference between advection of vorticity and vortex stretching will be bigger than in regions where bathymetry is large. Table 1 shows the depth integration balance coefficients as a function of the e-folding depth and bathymetry. Both d_o and d_1 increase non-linearly with the e-folding depth when the bathymetry inceases. If H_o is larger than 200 m and bathymetry is larger than 1000 m, the depth-integrated vortex stretching will increase two orders of magnitude from its surface values while the depth-integrated advection of vorticity will increase only one order of magnitude.

Using the vertical structure fit found with ADCP observations west coast of Oahu by Chavanne et al. (2010b), the e-folding depth is H_o=~100 m. In region B were depth is around 200 m, d_o=86 m and d_1=49 m, therefore the depth-integrated vortex stretching will increase 50% from the mean surface vortex stretching values whereas the depth-integrated advection of vorticity will increase one order of magnitude from the mean surface advection of vorticity. In contrast, in region A where bathymetry is around 600 m, $d_o = 100$ m and $d_1 = 50$ m, that is, the depth-integrated vortex stretching will be 20% larger than in region B while the depth-integrated advection of vorticity will increase one order of magnitude as in Region B. Thus, both the depth-integrated advection of vorticity and vortex stretching in the L.H.S of equation 2.5 will result in $O(10^{-8})$ s^{-2}. As in the previous section, we calculated surface frictional forcing as $\nabla \times \tau = 1 \times 10^{-5}$ Pa m^{-1} resulting in values in the $O(10^{-8})$ s^{-2} as advection of vorticity and vortex stretching.

The second term on the R.H.S of (5) is the vorticity produced by bottom stress (τ_b). Previous studies have shown this term to be important in shallow regions (Csanady 1978;

Brink and Allen 1978) but the lack of direct observations of bottom stresses does not allow for an accurate estimation. It is important to notice that in coastal and shallow areas like Penguin Bank this term could contribute to the balance and thus be part of the residual.

The contribution of vorticity by bottom pressure torque ($J(P_b, H)$) to the depth-integrated vorticity balance can be estimated assuming the two-year mean HFR surface velocities are geostrophic. In this case; $J(P_b, H)$ is equal to $f\mathbf{u}_{bg} \cdot \nabla H$, where $\mathbf{u}_{bg}$ is the bottom geostrophic velocity and ∇H is the spatial gradient of bathymetry. For areas shallower than the e-folding depth (H_o), the bottom geostrophic velocity will roughly equal the HFR surface mean velocity. Using the H_o of 100 m, in areas around Penguin Bank ($\sim$50 m) where spatial variations of depth (∇H) are about 1 m every 100 m, bottom pressure torque would result in values in the $O(10^{-8}\text{ s}^{-2})$ if surface velocities are larger than $\sim$15 cm s^{-1}, which was the case throughout the time period analyzed (Figures 3a and 3b). This result indicates that the large vortex stretching values seen north of Penguin Bank at around $\sim$ 157.7^{o}W observed in the mean surface vorticity balance (Figure 2.5) could be induced in part by the bottom pressure torque and are part of the residual.

2.6.3   Topographic steering of HFR surface flow by Penguin Bank

As shown by the depth-integrated balance, bathymetry can influence the mean flow if spatial gradients of bathymetry are large enough such as in the Penguin Bank region. This section evaluates if the Penguin Bank steers the HFR-derived surface velocities by means of Potential Vorticity (PV).

Assuming a fully barotropic flow, a PV conservation can be written as $J(\psi, \frac{f}{H}) = 0$ requiring flow to follow contours of f/H where H is ocean depth and f is the Coriolis parameter. If f/H were conserved along streamlines, then angular separation between the 3-day low-passed HFR-derived surface velocities ($\mathbf{u}$) and $\nabla(f/H)$ will be 90°. If the angle between $\mathbf{u}$ and $\nabla(f/H)$ is mostly at right angles over the two-year period with a small standard deviation, it is an indication of topographic steering of a barotropic flow (Thomson and Freeland 2003; LaCasce et al. 2008). For the area south of Oahu, this PV constrain

will incite a clockwise circulation around the ~ 50 m Penguin Bank and a counter-clockwise circulation around the ~ 700 m Kaiwi channel.

Figure 2.7 shows the standard deviation and median of the separation angle over the two-year time period. The smallest standard deviation (90°) was found south-west of Penguin Bank while towards the Kaiwi Channel the standard deviation increased to 120°. These large standard deviation values indicate that either the mean surface flow is less influenced by topography or the assumption of a barotropic flow is not valid. As shown above, Chavanne et al. (2010b) found an e-folding depth of 100 m indicating that for shallow areas the assumption of a barotropic flow can be valid. South-wesst of Penguin Bank, the standard deviation was less than 90° and the median angle was found at around 90° (Figure 2.7b, red lines), indicating flow was mostly constrained by topography. In contrast, over Penguin Bank, standard deviation varied between 60° and 120° with a median angle around 45°. This is mostly due to flow modified by a combination of surface forcing (as shown above) and instrument noise (Appendix B).

Figure 2.8 shows the histograms of separation angles from the selected area shown Figure 2.7a (black) and the region limited by the red dashed line (red). The histogram computed over the Penguin Bank area shows a bimodal distribution suggesting there are two distinct processes modifying the surface circulation. As expected, the histograms calculated over the area where median was 90° (Figure 2.8 red) most of the angles were found at around 90° indicating topography steering by the Penguin Bank bathymetry is the main process modifying the surface circulation. This topographic steering can also be observed in the surface current time-series (Figure 2.3b), where in Region B, northward surface components are frequent throughout the two-year time period.

2.7   Summary

HFRs observations reveal the regional dynamics south of Oahu through its mean surface velocity and vorticity structure. The two-year mean surface velocities exhibit a westward flow and mean Ro in the $O(0.2f)$. Maps of advection of relative vorticity and vortex

stretching were produced at scales down to 2 km revealing spatial variations of vorticity due to bathymetry and wind stress curl.

The most striking feature of the mean surface vorticity balance is the anti-correlation between advection and stretching of vorticity, revealing flow driven by the mean advection of PV anomalies from other latitudes. The divergence of the eddy flux of relative vorticity was also estimated, resulting in values $\sim 50\%$ smaller than the leading-order terms (advection and vortex stretching) and following a similar pattern as advection of vorticity suggesting an influence of eddies in the mean vorticity budget. The residual from these terms was interpreted as the sum of unquantified terms and noise. Of the unquantified terms, we estimate that wind stress curl is the most significant contributor to the residual, in agreement with previous work by Chavanne et al. (2010b) and Azevedo Correia de Souza et al. (2015).

In shallow regions, however, bottom pressure torque accounts for most of the residual since vortex stretching is larger than advection of vorticity. An estimation of the depth-integrated vorticity equation assuming an equivalent barotropic flow was made. We found that bottom pressure torque could act a first-order term when spatial variations of topography are large enough such as the case of Penguin Bank. In addition, a PV analysis showed that bathymetry gradients can sometimes steer the surface circulation such as in Penguin Bank.

2.8   Appendix A: HFR settings and Data processing

The frequency-modulated continuous-wave (FCMW) HFRs were operated yielding a range resolution of 1.2-1.5 km and averaging times of 9-12 min yielding a time resolution of 15 min with each site transmitting while the other was quiet. The transmit antenna formed a beam toward the ocean, a null in the direction of the receive antennas to reduce the direct path energy. The instruments were operated in beam-forming mode with linear arrays of 8 receive antennas, yielding an azimuthal resolution of $\sim 7°$ when steering the beam normal to the receive array and degrading higher incidence angles; above 60 ° the sidelobes are too

large to obtain uncontaminated measurements (Gurgel et al. 1999b).

Vector currents were mapped on a 2-km cartesian grid by least square fitting the zonal and meridional component to radial measurements from both sites within a 2 km radious. A major problem is the geometric dilution of precision (GDOP), which amplifies measurement errors when the angles between the different radial directions available are closer to 0° or 180°. Following Lipa and Barrick (1983) an Chavanne et al. (2007), we use the principal axes of the covariance matrix of the vector currents, to discard poorly constrained estimates as follows.

The currents were assumed to be constant within the search radius, where N is the number of radial measurements available:

$$m_i = n_{ix}u + n_{iy}v + e_i i = 1, ... N \tag{2.6}$$

or

$$\mathbf{m} = \mathbf{N}\mathbf{w} + \mathbf{e} \tag{2.7}$$

where $\mathbf{m}$ is the vector of radial measurements, $\mathbf{N}$ the N x 2 matrix of the unit radial vectors, $w = [u, v]^T$ the current vector and $\mathbf{e}$ the N x 1 vector of measurements noise and model errors.

An estimate of $\mathbf{w}$ can be obtained by minimizing the sum of squared errors:

$$J = \sum_{i=1}^{N} e_i^2 = \mathbf{e}^T\mathbf{e} \tag{2.8}$$

Solution is :

$$\tilde{\mathbf{w}} = (\mathbf{N}^T\mathbf{N})^{-1}\mathbf{N}^T\mathbf{m} \tag{2.9}$$

The covariance of A4 is:

$$\mathbf{C}_{\tilde{w}\tilde{w}} = (\mathbf{N}^T\mathbf{N})^{-1}\mathbf{N}^T\mathbf{C}_{ee}\mathbf{N}(\mathbf{N}^T\mathbf{N})^{-1} \tag{2.10}$$

where C_{ee} is the covariance of C. If the errors have the same variance and are independent of each other then

$$\mathbf{C}_{ee} = \sigma^2 \mathbf{I} \tag{2.11}$$

where $\mathbf{I}$ is the unit matrix. Then the covariance of $\tilde{\mathbf{w}}$ becomes:

$$\mathbf{C}_{\tilde{w}\tilde{w}} = \sigma^2 (\mathbf{N}^T \mathbf{N})^{-1} \tag{2.12}$$

This expression of $\sigma = 1$ becomes the GDOP. Figure 2.9a shows the principal axes of $\mathbf{C}_{\tilde{w}\tilde{w}}$. In the present study data with GDOP greater than 4 was discarded. This high value was required since the HFR configuration increased the GDOP substantially close to the coast and away from the sites. This GDOP is seen in the HFR-derived surface currents variance ellipses and Eddy Kinetic Energy (EKE) derived from HFRs and as expected, it is not observed in the ROMS surface currents interpolated in to the HFRs since the model assimilates the HFR radial components (Figures 2.9b and 2.9c). In most of the HFR coverage, the axis of maximum variance is parallel to the coast, except close to the coast and away from the HFRs sites where GDOP poorly constrains the meridional and zonal component increasing the instrument noise. However, in areas where GDOP is small, in both model and observations ellipses increase away from the coast.

2.9 Appendix B: Vorticity Balance errors

The surface vorticity balance terms standard deviations over the two-year time period are shown on Figure 2.10. Values close to the coast and away from the HFR sites were GDOP is large (Appendix A) increased up to 4 times (Figure 2.10a to 2.10e) compared to Figure 2.10f derived by ROMS and WRF models. The largest values were found close to the south shore of Oahu and north of Penguin Bank. To reduce the uncertainty of the HFR-derived vorticity terms, values where GDOP is larger than 4 (Figure 2.9a) are removed when calculating the time-mean vorticity balance. When the residual includes the divergence of the eddy flux of relative vorticity (denoted as R_2 in Figure 2.10e) the variability is enhanced not only by

the large GDOP values but by the large noise when calculating the eddy vorticity forcing terms, thus increasing the noise in the total residual R_2.

The anti-correlation between advection of vorticity and vortex-stretching is more than just a visual interpretation (Figure 2.5a and 2.5b). The small scale geophysical and instrument noise plus the filtering and smoothing can modify this anti-correlation since smoothing reduces the amplitude of the signal and can increase the regression coefficient (Hughes 2005). For this study, using the 30-day low-passed data reduced the variance of each term in the vorticity equation, and increased the correlation coefficient between the terms compared to the 3 and 7 day low-passed data.

Table 2.1: Depth Integrated balance coefficients assuming an equivalent barotropic flow as a function of the e-folding depth H_o for various bathymetries of 50, 200 and 1000 m.

H_o	50 m	200 m	1000 m
$d_o(-50)$	32	44	49
$d_o(-200)$	49	126	181
$d_o(-1000)$	50	199	132
$d_1(-50)$	22	39	48
$d_1(-200)$	25	86	165
$d_1(-1000)$	25	100	432
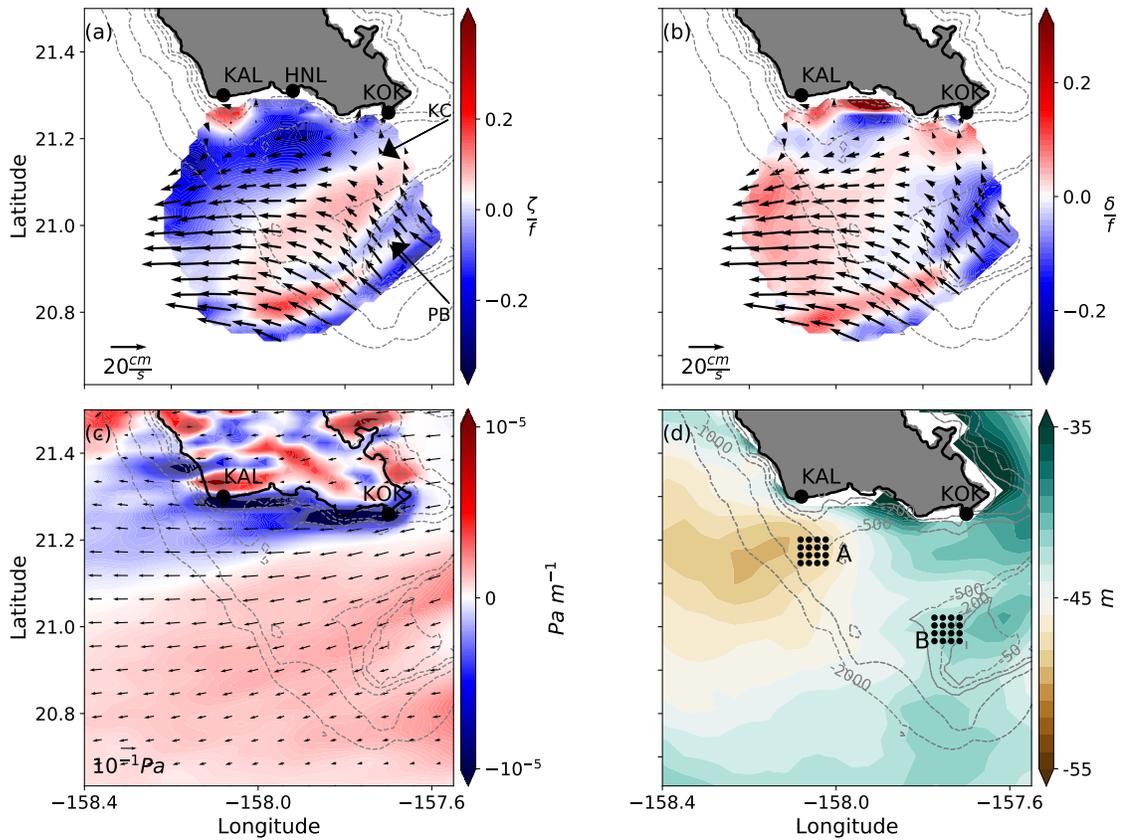
Figure 2.1: Time-averaged HFR surface currents overlaid over the time-averaged (a) relative vorticity and (b) divergence normalized by f. Arrows indicate the Kaiwi Channel (KC) ($\sim$ 600 m depth) and Penguin Bank (PB) ($\sim$ 50 m depth), (c) WRF wind stress vectors overlaid over wind-stress curl $Pa\,m^{-1}$ and (d) mixed layer depth (m) computed from ROMS. Figures show the temporal mean from September 2010 to September 2012. Black dots indicate the HFR sites Kalaelola (KAL) and Koko Head (KOK) and the Honolulu airport meteorological station (HNL). Bathymetry is shown at 50, 500 and 1000 m.
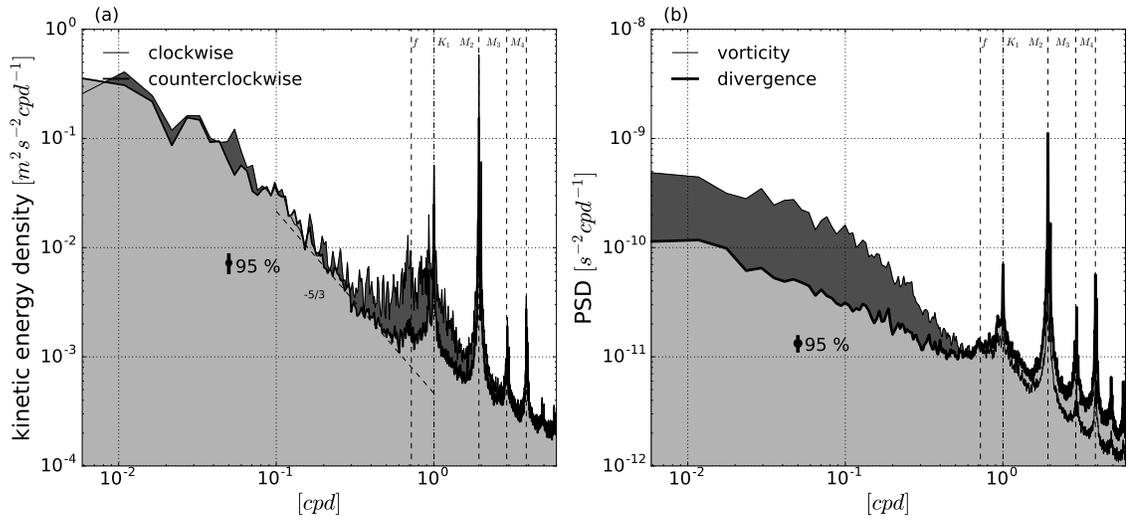
Figure 2.2: (a) Rotary power spectra for September 2010 to September 2012, spatially averaged over grid points where GDOP is lower than 4 (Appendix A). Clockwise and counterclockwise components are plotted with thin and thick lines respectively. The slanted dashed line shows the -5/3 spectral slope. (b) As with (a) but for vorticity (thin line) and divergence (thick line). The 95% confidence limits is shown in both figures.
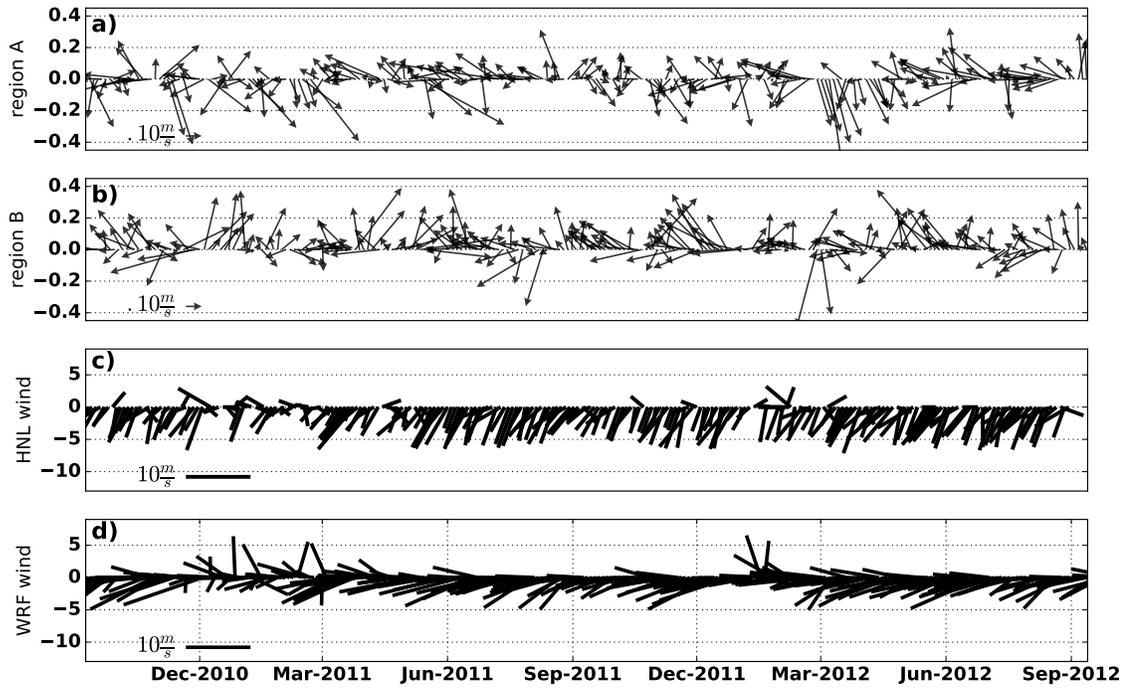
Figure 2.3: Time series of spatially averaged HFR detided surface currents from (a) region A and (b) region B, defined in Figure 2.1d. c) Honolulu airport wind vectors and (d) WRF wind vectors spatially averaged over the HFR spatial domain in Figure 2.1.

26
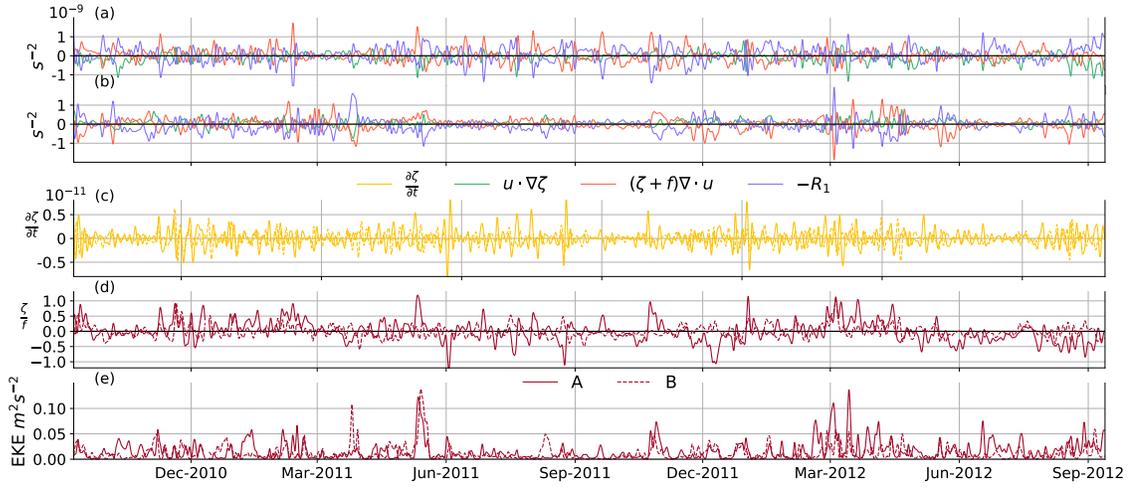
Figure 2.4: Time series of spatially averaged advection of vorticity (green line), vortex stretching (orange line) and sum of these terms defined as R_1 (purple line) for (a) region A and (b) region B, units are in the $O(10^{-9})$ s^{-2}. (c) Time series of normalized relative vorticity (red line) and (d) change of rate of relative vorticity (yellow line) in 10^{-11} s^{-2}, (e) eddy kinetic energy. Solid and dashed lines represent spatial average over regions A and B defined in Figure 2.1d. All quantities are calculated from the 3-day low-pass HFR surface currents.
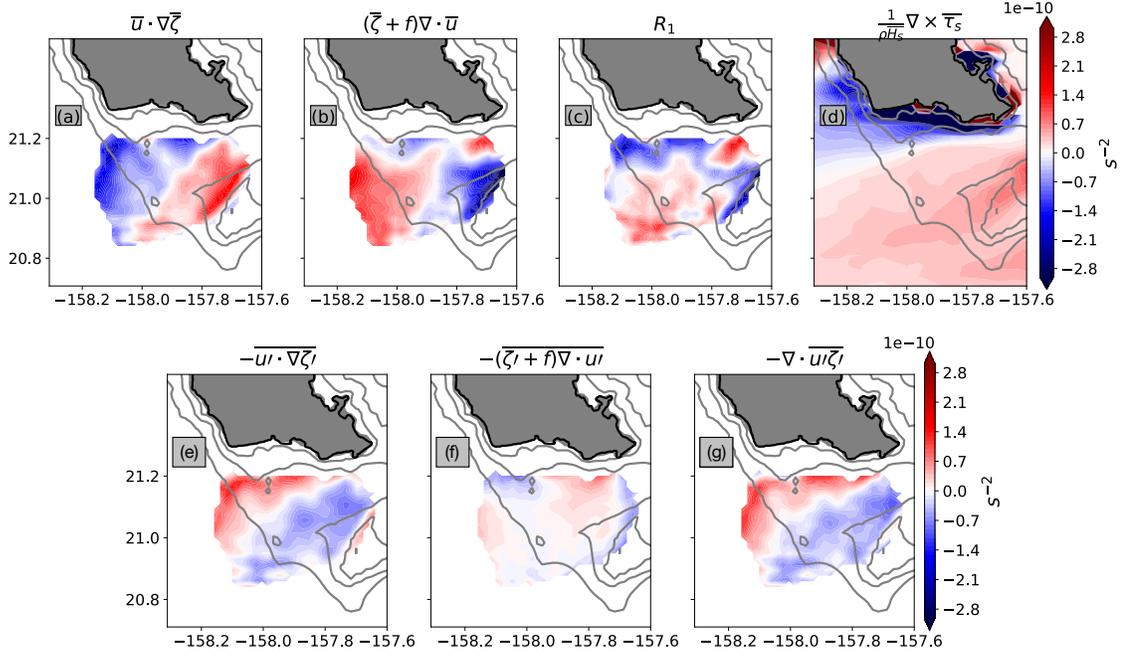
Figure 2.5: Temporally averaged vorticity terms from September 2010 to September 2012 derived by HFR surface currents (all panels except (d)) and a combination of ROMS-derived surface layer depth and WRF-derived wind stress curl. (a) Advection of mean vorticity by the mean flow ($\overline{\mathbf{u}} \cdot \nabla \overline{\zeta}$), (b) vortex stretching by the mean flow (($\overline{\zeta} + f)\nabla \cdot \overline{\mathbf{u}}$), (c) residual from (a) and (b) and (d) surface frictional forcing ($\frac{1}{\rho H_s}\nabla \times \tau_s$). (e) Advection of eddy vorticity ($\overline{\mathbf{u}' \cdot \nabla \zeta'}$), (f) stretching of eddy vorticity ($\overline{\zeta'\nabla \cdot \mathbf{u}'}$) and (g) sum of (e) and (f) as divergence of the eddy flux of relative vorticity ($\nabla \cdot \overline{\mathbf{u}\zeta'}$). Values where GDOP is higher than 4 were removed from all panels except (d), see Appendix A.
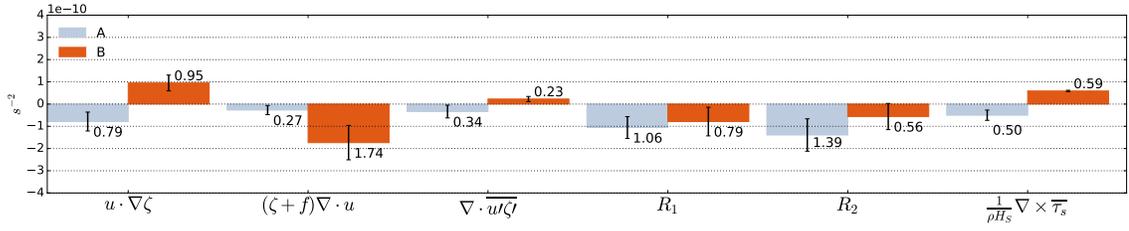
Figure 2.6: Mean Vorticity terms from equation (4) for regions A and B denoted in Figure 2.1. R_1 indicates residual of mean advection of vorticity ($\overline{\mathbf{u}} \cdot \nabla \overline{\zeta}$) and vortex stretching (($\overline{\zeta} + f)\nabla \cdot \overline{\mathbf{u}}$). R_2 indicates $R1$ plus divergence of eddy flux of relative vorticity ($\nabla \cdot \overline{\mathbf{u}\zeta'}$). Standard deviation over each of the regions is shown in black lines.
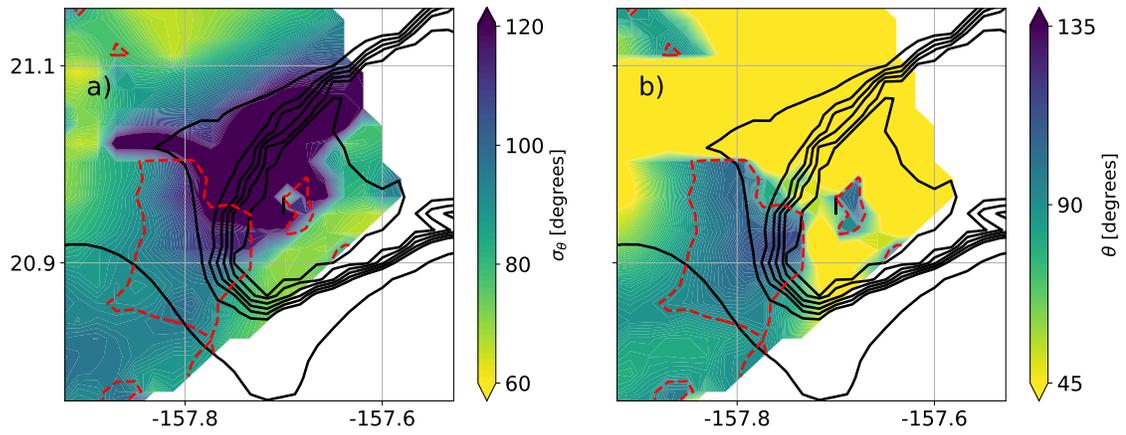
Figure 2.7: (a) Standard deviation and (b) median of separation angle over the two-year record from September 2010 to September 2012. Separation angle is defined in degrees between the 3-day low-passed HFR surface currents and $\nabla(f/H)$. A positive angle is a clockwise angle between the surface flow and $\nabla(f/H)$. A value of 90° indicates flow is strictly constrained by bathymetry assuming a barotropic flow.
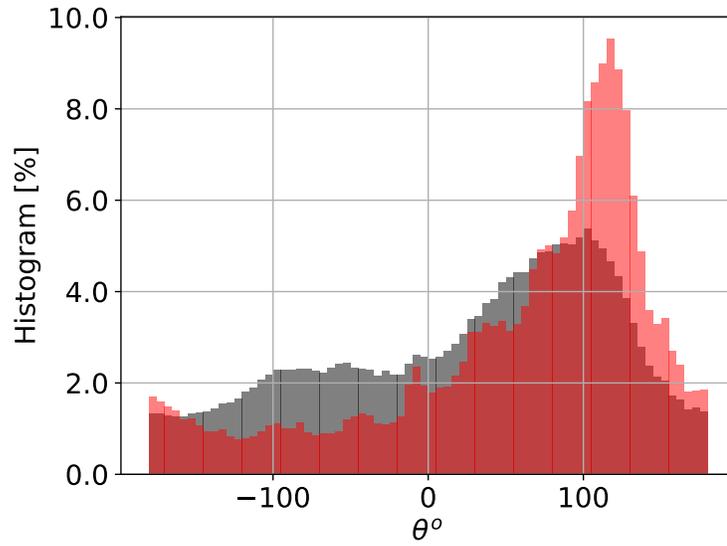
Figure 2.8: Histograms of separation angle between HFR surface currents and $\nabla(f/H)$ for the region shown in Figure 2.7 (black) and the region limited by the red line in Figure 2.7 (red). Angles were calculated from the 3-day low-passed surface currents assuming a barotropic flow.
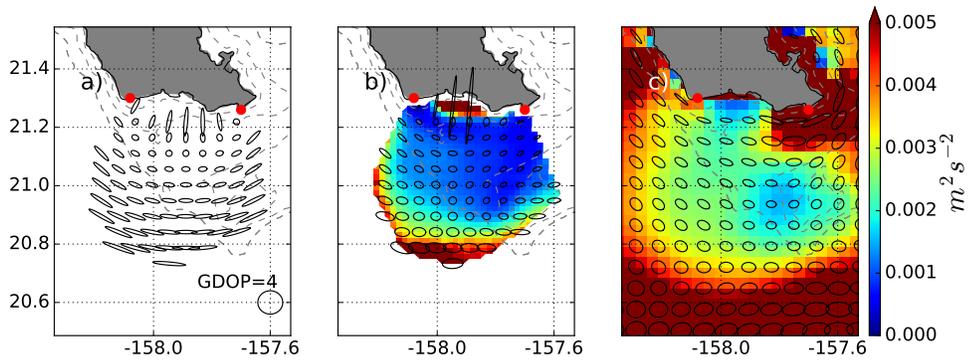
Figure 2.9: (a) GDOP over the HFR domain, GDOP=4 is shown on the right-bottom corner. (b) Variance ellipses from the HFR surface currents and (c) Variance ellipses from the ROMS surface currents interpolated into the HFR domain. Colorbar indicates the EKE derived by HFR and ROMS variance ellipses in (b) and (c) respectively. Red dots indicate the HFR sites KAL and KOK. Bathymetry is shown as dashed grey lines at 50, 500 and 1000 m.
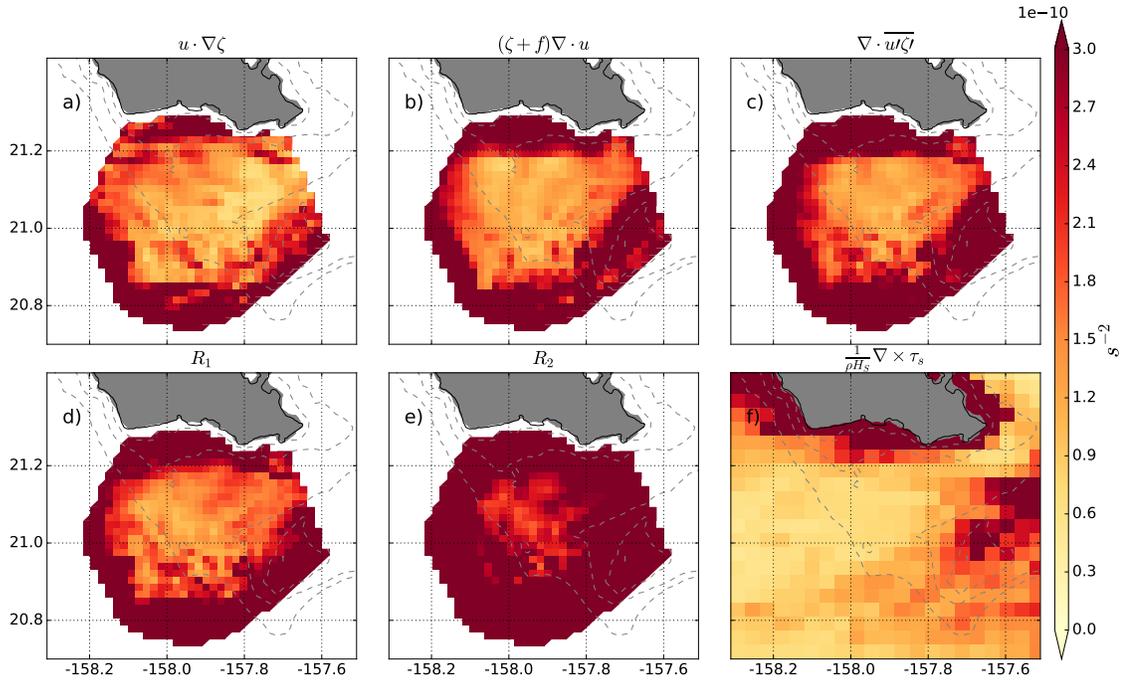
Figure 2.10: Standard Deviation of HFR and model derived vorticity terms from September 2010 to September 2012. (a) Advection of relative vorticity ($\mathbf{u} \cdot \nabla \zeta$), (b) vortex stretching $(((\zeta + f)\nabla \cdot \mathbf{u}))$, (c) divergence of the eddy flux of relative vorticity $((\nabla \cdot \overline{\mathbf{u}\prime\zeta\prime}))$, (d) residual of (a) and (b) (R_1) and (e) residual of (a), (b) and (c) (R_2) and(f) surface frictional forcing $(\frac{1}{\rho H_s}\nabla \times \tau_s)$.

33

CHAPTER 3
NEAR INERTIAL OSCILLATIONS OFF THE SOUTH SHORE OF OAHU

3.1 Introduction

Near-inertial oscillations (NIOs) are ubiquitous in the ocean. They are forced mainly by the wind and have a frequency close to the local Coriolis parameter f. Mid-latitude storms (D'Asaro 1985), hurricanes (Firing et al. 1997) and typhoons (Yang and Hou 2014) contain strong inertially rotating wind components that produce near-inertial energy at the ocean surface. This energy can sometimes propagate to the ocean interior through near-inertial waves (NIW) [e.g., *Soares et al.,* 2016] and contribute to the abyssal diapycnal mixing (Alford and Gregg 2001) and to the energy budget of the ocean.

This near-inertial energy is expected to propagate mostly towards the equator where f becomes small, except in cases where the near-inertial energy is generated at a frequency larger than the critical latitude when it is then allowed to propagate poleward. It is therefore more common to observe NIOs at a frequency larger than f.

Through horizontal convergences and divergences which pump the stratified base of the mixed layer, surface NIOs generate near-inertial internal waves (NIW) near the local Coriolis frequency. NIWs can be an important nutrient supply to coastal ecosystems (Lucas et al. 2014) since the mixed layer deepening produces phytoplankton dispersion (Franks 1995). Furthermore, because of their strong vertical shear, NIOs are a major contributor to the upper-ocean mixing (Jochum et al. 2013). The spatial variability of the amplitude and frequency of the surface NIOs can therefore modify the NIW generation and propagation characteristics.

Although the NIOs have been widely studied in terms of their generation and propagation in the vertical (Fu 1981; Kunze and Sanford 1984, 1986; D'Asaro et al. 1995), the horizontal variability has been less explored (Chereskin et al. 1989; Klein et al. 2003; Kim et al. 2015; Whitt and Thomas 2015) due to the lack of spatial observations.

The sub-inertial flow (Weller 1982), the bathymetry, coast (Millot and Crépon 1981; Pettigrew 1981; Shearman 2005) and wind (Whitt and Thomas 2015) can contribute to the spatial and temporal variability of the NIOs. In addition, NIOs can interact with the mean background flow either by subtracting or adding energy to it and so have been proposed as an important component of the ocean kinetic energy budget linking larger scales to smaller scales (Ferrari and Wunsch 2009; Danioux et al. 2008; Whitt and Thomas 2015; Jing et al. 2016).

The Hawaiian Islands are a prime area to study the interaction between NIOs and other dynamical processes such as sub-inertial flow, bathymetry and coast. The canonical circulation is comprised by the westward Hawaiian Lee Current flowing south of the island archipelago and the persistent trade-winds which cause cyclonic and anticyclonic eddies in the lee of the islands due to the wind stress curl generated by the island-mountains (Castillo-Trujillo 2014). From September 2010 to September 2012, two High Frequency doppler Radars (HFRs) measured the surface currents off the south shore of Oahu Hawaii (Figure 3.3.1b) at a 2 km spatial and 1 hour temporal resolution. A ROMS assimilating the radial components of the HFR as well as other existing observations in the area (Figure 3.1c) is used in conjunction with the HFR observations. In addition, the HFR spatial domain (Figure 3.1b) encompasses the 50-m Penguin Bank and the 700-m deep Kaiwi channel which could also contribute to the NIOs variability.

The goal of this paper is to characterize the spatial and temporal scales of NIOs observed in HFR and ROMS surface currents. We will also compare previous theoretical and numerical theories describing the NIO characteristics at scales observed in the HFRs and ROMS. We will first describe the statistics of the observed near-inertial oscillations in terms of their spatial and temporal variability. We then describe the largest near-inertial event and investigate the scales at which NIOs interact with the background flow in conjunction with satellite altimetry.

This paper is organized as follows. Section 2 describes the data and methods. Section 3 describes the horizontal structure and seasonality of the NIOs while section 4 focuses

on describing the near-inertial event. Section 5 discusses the model and observations discrepancies and the NIOs spatial scale implications.

3.2   Data and Methods

3.2.1   HFRs surface currents

Two WERA HFRs, with a range of $\sim$100 km and a range-resolution of 1.5 km, were deployed on the south shore of Oahu, Hawaii from 2010 to 2012 to measure surface currents. A description of the principles of the WERA radars can be found in Gurgel et al. (1999a), Gurgel et al. (1999b), the configuration of the radars (frequency 16 MHz, bandwidth 100 kHz) and the processing techniques were identical to those detailed by Chavanne et al. (2007), Chavanne et al. (2010).

Figure 3.1a shows the location of the two radars in Kalaeloa (KAL, 21° 18 N, 158° 5 W) and Koko head (KOK, 21° 26 N, 157° 42 W). Figure 3.1b shows the HFR spatial domain defined as the area with at least 60% of the useful data over the two-year period, covering the 670-m deep Kaiwi channel, and the shallow 50-m Penguin bank.

Figure 3.2 shows the variance preserving spectra averaged over the HFR spatial domain for the HFR and ROMS surface currents. The diurnal and semidiurnal tides, and their harmonics, dominate the super-inertial band. Clockwise energy is larger than the counterclockwise energy in a band centered around the local Coriolis frequency of 0.71 cpd (33.4 hrs period) and extending from the 0.3 cpd down to the semidiurnal tide (M2) in the HFR observations, and down to the M3 tidal harmonic in the ROMS simulations.

This study is focused on the near-inertial currents within the $\pm$ 0.2f band centered around f. Temporal filtering of the radar time series is therefore essential to separate these motions from those outside the near-inertial band. First, the tidal constituent estimation algorithm (t_tide) (Pawlowicz et al. 2002) was used to extract the astronomically-coherent tide from the raw HFR and ROMS data. Secondly, a band-pass finite impulse response filter (FIR) with cut-off frequencies of 1/27 and 1/40 hours^{-1} ($\pm$0.2f), denoted as dashed

lines in Figure 3.2) was used to extract the near-inertial currents.

A wavelet power spectrum (wavelet transform amplitude squared) was also computed over the near-inertial currents using a Morlett window (Gaussian times a sinusoid) with a frequency $\omega = 6$ and a frequency discretization around the inertial band of 0.04 cpd for both model and observations. The time series were normalized to unit variance to ensure the scale was directly comparable with each other. The near-inertial event described in section 4 was selected after a Monte Carlo test (see Torrence and Compo (1998) and Appendix A) deemed it the most significant event in the record.

3.2.2 Wind data

Measurements of wind speed and direction were obtained from the NDBC (NOAA DATA Buoy Center) 51003 meteorological buoy 30-km located south-west of the HFR domain (shown on Figure 3.1a). A local implementation of the Weather Research Forecast (WRF) model (Tu and Chen 2011) for the area around Oahu, assimilating data from satellite, aircrafts and buoys, is also used to provide the surface wind field at spatio-temporal resolutions matching the radar grid (Figure 3.1d).

The correlation between the wind buoy and the closest WRF model grid point was significant (0.93) at 95% significant level. Wind stress was computed following Large and Pond (1981) as $\tau = \rho C_d \mathbf{U}_w \mathbf{U}_w$ where ρ is the density of air, C_d is the constant drag coefficients and $\mathbf{U}_w$ is the wind speed at 10 m above sea level. Wind speed observations from the buoy were adjusted to 10 m for the neutral wind stress calculations using a log-layer factor.

3.2.3 Model

The assimilative oceanic model used here is based on the Regional Ocean Modeling System (ROMS), a free-surface, hydrostatic, primitive equation model discretized with a terrain-following vertical coordinate system (Shchepetkin and McWilliams 2005). The assimilation system is based on previous work (Azevedo Correia de Souza et al. 2015; Janeković et al.

2013; Matthews et al. 2012; Powell et al. 2009). It uses four-dimensional variational assimilation (4D-Var) to integrate daily data from HFR radial currents, satellites, autonomous gliders, Argo drifters, and other in-situ measurements. Barotropic forcing is from the TOPEX-POSEIDON tidal constituents, and the lateral forcing is provided by the coarser resolution global HYCOM. The surface forcing uses high-resolution winds from the 1.5-km WRF atmospheric model described in sec. 2.2. The ocean model was run at 4-km resolution over a domain covering the Hawaiian Islands ($153°$W to $163°$W and $17°$N to $24°$N), with 32 terrain-following vertical levels: 9 levels span the upper 200m in deep water, with more levels near-surface as the slope ascends towards the islands. The model provides estimates of temperature, salinity, and currents. The mixed layer depth, an important parameter for this study was estimated as the depth where density varies 0.125 kg/m^3 from the surface (de Boyer Montégut et al. 2004).

3.3 Description of the Near-Inertial Oscillations

The near-inertial band accounts for $\sim$5% of the total current energy in the south shore of Oahu, based on the HFR surface current variance-preserving spectra for the two years of data and spatially averaged over the HFR domain (Figure 3.2a). Clockwise energy accounts for 85% of the total near-inertial band, an indication of NIOs in the northern hemisphere.

Bursts as large as $\sim$15 cm s^{-1} are observed in the HFR near-inertial currents. The clockwise component of these bursts has values ranging from 5 to 10 cm s^{-1} while the counter-clockwise component of around 2 to 3 cm s^{-1} (Figure 3.3a). There are around 15 events with magnitude larger than 5 cm s^{-1}, found mostly from December to March and are generally observed following strong bursts of winds (Figure 3.4). In general, these near-inertial events have a duration of 5 to 7 days and were precluded by large wind bursts rotating $\sim$400$°$ in the last 48 hours before the events.

Similar to the HFR observations, the near-inertial band calculated from the model (ROMS) accounts for $\sim$4% of the total variance (Figure 3.2b). The near-inertial amplitudes over the two-year time period overlapped with the HFR time series are larger than the

HFR near-inertial currents with maximum events greater than 20 cm s^{-1} (Figure 3.3b). The clockwise component of these events ranges from 5 to 20 cm s^{-1} while the counter-clockwise component is less than 5 cm s^{-1} throughout the time series. Note that the largest near-inertial events in the observations don't always overlap with the events observed in the ocean model.

3.3.1 Seasonal Variability

Near-inertial current variability is highly episodic but in general is stronger in winter (Figure 3.3a). Amplitudes larger than 10 cm s^{-1} are mostly found from December to March while during the rest of the year amplitudes are usually less than 5 cm s^{-1}. This seasonality is not observed in the ROMS near-inertial currents where amplitudes larger than 10 cm s^{-1} are observed throughout the time series with some events having values larger than 20 cm s^{-1} (Figure 3.3b).

The seasonality in the HFR data is also seen in the wavelet power spectrum averaged over the near-inertial band (Figure 3.5a) where significant (see Appendix A) near-inertial events in winter have amplitudes at least 5 times larger than the rest of the year. In contrast, the wavelet power spectrum averaged over the near-inertial band calculated from the ROMS shows significant events larger than 10 cm s^{-1} throughout the year (Figure 3.5b).

The HFR observations indicate that the near-inertial band accounts for 25% of the total KE In winter, 12% in spring and 17% in summer. If the variance is calculated only for winter and over the four sub-regions shown in Figure 3.1b, the near-inertial variance accounts for 60% of the total energy in the north and west regions while 40% in the south and east regions. The ROMS surface current spectra averaged over the HFR spatial domain and near-inertial band results only in 3% of the total currents and in contrast with the HFR results, there is no spatial variability when computing the variance over the four regions.

This near-inertial current variability observed from the HFRs follows the seasonal cycle of the wind (Figure 3.4). Wind stress variability from the NDBC buoy located 80-km southwest of Oahu is plotted on Figure 3.4b. There is a slight seasonal cycle in the

39

meridional component of the wind stress variability with amplitudes about twice as large in winter than the rest of the year. This seasonality is also observed in the wind-vector time series (Figure 3.4a) where wind frequently rotates from the north-east to the south-west from December to March (Castillo-Trujillo 2014). The WRF wind vector time series also show a seasonal cycle (Figure 3.4c) with south-west winds from December to March and north east trade winds for the rest of the year . Modeled and observed winds shifts are associated with atmospheric frontal passages common from December to March in the Hawaiian Islands (Tu and Chen 2011).

Bursts of near-inertial currents are usually preceded by short duration wind events of at least 10 m s^{-1}, particularly in the HFR near-inertial currents (Figure 3.3a), however, not all wind bursts are associated with an increase on the near-inertial currents. In the ROMS simulations (Figure 3.3b), there are several near-inertial events observed throughout the time-series that are not associated to any wind burst (Figure 3.4).

Another potential explanation for the increase in near-inertial variability is the mixed layer depth since an inverse relationship between the mixed layer depth and the near inertial current amplitude (deeper mixed layer is associated to smaller near-inertial amplitude) is expected (Price et al. 1986; Shearman 2005). The mixed layer depth computed from the ROMS over the HFR spatial domain has a seasonality with maximum values in winter and minimum values in summer. Nevertheless, an underestimation of the mixed layer depth by the model could be related to the larger near-inertial amplitudes observed in the model relative to the HFR observations. This will be discussed in more detail in section 5.

3.4 Case study: Description of a Near Inertial event

A near-inertial event was selected from the model and observations band pass surface currents time series (Figure 3.3). This event was chosen for further analysis for two reasons: i) it was significant and well above background near-inertial amplitudes in both model and observations according to the wavelet power spectrum, and ii) the HFR data coverage and quality was better than the other significant events.

The detided surface currents from HFR and ROMS were complex demodulated at f to produce information on the phase and amplitude of the selected near-inertial event observed from March 4-12 2012 in the band-pass time series (Figure 3.3). The spatial scales of the near-inertial event are given by the spatial correlation between grid points and are in the order of ~20 km in the HFR observations and ~40 km in the ROMS simulations, similar to Kim and Kosro (2013) results. To illustrate this spatial variability, demodulated currents were averaged over the four sub-areas shown in Figure 3.1b (north, south, west and east).

The amplitude of the HFR observed near-inertial event began to grow, in all sub-regions, in March 4 and remained at its maximum (15 cm s^{-1}) from March 7 to March 10. From March 10 to March 13 the amplitude decreased down to ~5 cm s^{-1} (Figure 3.6a). The largest amplitudes were observed in the north, at around 18 cm s^{-1} while the rest of the sub-regions had maximum amplitudes of around 10 cm s^{-1}. These spatial differences are also detected in the wavelet power spectrum averaged over the near-inertial band (Figure 3.5a) where near-inertial amplitudes 3 times larger than the rest of the regions are observed in the north region.

In comparison, ROMS maximum amplitudes over the near-inertial event were ~15 cm s^{-1}. The near-inertial amplitude began to grow in March 2 and remained at its maximum until March 12. There is little spatial variability between the sub-regions except from March 9 to March 12 where the south and west had larger amplitudes than the rest of the areas.

A positive (negative) value of the change in phase with time of the demodulated currents indicates motion at a frequency less (more) than the local inertial frequency (-0.71 cpd) (Weller 1982; Gough et al. 2010). Figure 3.6b shows the time series of the difference in phase between the observed near-inertial amplitudes and the demodulated currents at f. From March 6 to March 8 there was a negative slope of less than 2%f which translates to an actual frequency of ~ 0.67 cpd or 0.9f, while after March 8 the phase remained constant.

The model phase remained constant during the near-inertial event with a small positive slope of less than 0.1f. Since this slope is similar to the frequency resolution of the demodulation, it is not possible to identify the frequency of the near-inertial event from

this method (Figure 3.7b).

A complex demodulation at trial frequencies from 0.7f to 1.2f was computed from the detided HFR and ROMS currents over March 2012 to extract the frequencies of maximum amplitudes and phase with respect to the local inertial frequency during the event (Figure 3.8 and 3.9). The results from the HFR currents showed the largest amplitudes at ∼16 cm s^{-1} in the north region at ∼0.8f from March 6 to March 8, consistent with the negative phase slope observed in Figure 3.6b. A maximum amplitude from March 6 to March 8 at ∼0.9f is also observed in the east region but with values of around 12 cm s^{-1}. All regions, except the north presented two near-inertial energy maxima, one from March 6 to March 8 and one from March 9 to March 11. As with the HFR results, the ROMS demodulated currents at trial frequencies did exhibit two near-inertial amplitude maxima (Figure 3.9) but the largest amplitudes were found in the west and south sub-regions in contrast to the maximum amplitudes found in the north sub-region in the observations and model amplitudes never exceeded 10 cm s^{-1}. Furthremore, maximum amplitudes were generally observed at frequencies larger than f except in the south region.

3.4.1 Slab layer model

Rotating winds bursts were observed before the March 2012 event in both the WRF model and NDBC buoy. To evaluate if indeed the wind generated the NIO described above, the slab layer model (Pollard and Millard Jr 1970; D'Asaro 1985) is computed and compared to the demodulated currents at f. This model has been successful in simulating wind-generated near-inertial motions (Alford and Whitmont 2007; D'Asaro 1985) at different locations in both high and low latitudes. The model represents the transfer of momentum from wind stress into a forced surface layer layer ("slab") viz.:

$$\frac{\partial u_m}{\partial t} - f v_m = \frac{\tau_x}{\rho_o H} - r u_m \tag{3.1a}$$

$$\frac{\partial v_m}{\partial t} + f u_m = \frac{\tau_y}{\rho_o H} - r v_m, \tag{3.1b}$$

where u_m and v_m are the zonal and meridional components in the mixed layer forced by the wind, r is the damping coefficient, τ_x and τ_y are the wind stress east and north ward components, H is the mixed layer depth and ρ_o is density of seawater. u_m and v_m were solved iteratively using the interpolated-into-HFR WRF wind model to produce a time series of slab layer model currents during March 2012. The Ekman transport velocity $\mathbf{u}_E = \frac{\tau_x + i\tau_y}{(r+if)\rho_o H}$ is removed from the solution. The damping term was chosen as r=3 days, and is consistent with previous work (Pollard and Millard Jr 1970; D'Asaro 1985; Kim et al. 2014; Whitt and Thomas 2015) and yields the best match between the demodulated and slab model currents. The mixed layer depth H used is derived from the ROMS simulations as explained in section 2.3 and is interpolated in to the HFR grid points.

Time series of the WRF wind stress used to solve equation 3.1 alongside the slab layer model and ROMS and HFR demodulated currents during the near-inertial event are plotted in Figure 3.10a and 3.10b. Both model and observed near-inertial amplitudes increase simultaneously with the slab layer model from March 6 to March 13 in all sub-regions, indicating a wind generated near-inertial event. Nevertheless, there are spatial variations between the slab layer model maximum amplitudes and the ROMS and HFR demodulated currents maxima. The largest slab layer model amplitudes were observed in the north and south sub-regions at around 20 cm s^{-1}. The model demodulated current in all four sub-regions were never larger than 12 cm s $^{-1}$, while the observed demodulated currents had a maximum of 20 cm s^{-1} only in the north region. Two maxima at around 12 cm s^{-1} were observed in the model and observed demodulated currents (March 7 and March 10), these maxima were not observed in the slab layer model.

RMS between the slab layer model and the ROMS and HFR demodulated currents over the near-inertial event are shown in Figure 3.16. RMS larger than 10 cm s^{-1} (HFR) and 6 cm s^{-1} (ROMS) were observed in the shallow 50 m Penguin Bank area. The lowest RMS (5 cm s^{-1}) were observed in the north and west of the HFR spatial domain in both model and observations while south of the HFR spatial domain (at 157.9°W and 20.45°N) maximum RMS values were seen in both model and observations. Smaller RMS values are not expected

between the slab model response and the HFR and ROMS near-inertial currents mainly because of the (1) presence of a lateral boundary such as the coast (Shearman 2005) (2) the variations in mixed layer depth which could be incorrect in the model (Plueddemann and Farrar 2006) and the (3) NIOs interacting with the background flow.

The spatial scales of the wind storms could impact the spatial scales of the observed NIOs (Weller 1982). The WRF wind model used as a surface forcing in the slab layer model and ROMS presented spatial and temporal variations of wind stress over the near-inertial event that could impact the spatial and temporal variability of the near-inertial amplitudes. The WRF model decorrelation spatial scales were found at $\sim$20 km, this variability is observed in the wind stress wavelet power spectrum, where maximum energy varies over frequency and space. There are two "blobs" of maximum energy around f; one from March 1 to March 3 which likely caused the near-inertial event and one from March 6 to March 8 which could either reinforce or dampen the already generated near-inertial event (Whitt and Thomas 2015). In the wavelet power spectrum extracted from the buoy situated at 19°N, two energy maxima are also observed from March 4 to March 7 and from March 9 to March 12. This time lag between the wind WRF model and buoy observations maximum amplitudes indicates a south-ward propagation of the wind storm at 50 km day^{-1}.

3.4.2 ROMS and HFR comparison

Maps of observed and modeled daily averaged near-inertial amplitudes over the event are shown in Figures 3.11 and 3.12 (first column). The spatial structure of the near-inertial amplitudes between model and observations differs significantly. The observed near-inertial amplitudes were largest at -157.80° and 21.10° while the model near-inertial amplitudes increased offshore. Both model and observations show the NIO propagating southward and a dampening of the energy in the 50-m shallow Penguin Bank. The observed near-inertial maxima are observed at 20 cm s^{-1} while the modeled underestimates these amplitudes by about 5 cm s^{-1}.

The mean background flow calculated from the 3 day low pass currents is shown on

Figures 3.11 and 3.12 (second column). Overall the model underestimates the vorticity values by 25% but follows a similar structure as the observations. In contrast, the spatial structure of the divergence (Figures 3.11 and 3.12, third column) is quite different between model and observations, with model values 50% greater than observations. The gradient and Laplacian of vorticity calculated from model and observations have a similar spatial structure over the near-inertial event (Figures 3.11 and 3.12, fourth and fifth column) but with the model overestimating observations around 60%.

Over the HFR spatial domain, 3 contours of 20° of phase extracted from the demodulated currents at f are observed in both model and observations. The HFR-derived phase lines follow the contours of vorticity after March 7, and after March 8 they are organized by the gradient and Laplacian of vorticity. This correspondence between phase lines and background flow is also observed in the model.

Since GDOP is a significant source of noise to the HFR-derived surface vector currents, demodulation was also performed on the KAL and KOK radial currents (Figure 3.13 and 3.14). As with the vector currents, the maximum near-inertial amplitudes are found in the north region with maximum values of about 20 cm s^{-1}. This maximum propagates southward from March 7 to March 10 consistent with the near-inertial currents observed in Figure 3.11 (first column). In addition, minimum values are found over Penguin Bank and in the north-west corner of the HFR spatial domain were vorticity gradients had maximum values.

3.4.3   Modification of the NIOs by the mean flow

NIOs interact strongly with the mesoscale and sub-mesoscale mostly by refraction and trapping of propagating NIOs (Kunze 1985) and two-way nonlinear energy transfers between fronts (Whitt and Thomas 2015). The amplitudes and peak frequencies of NIOs can be modified by geostrophic adjustment, background vorticity, horizontal density gradient, and tidal-inertial oscillations (Pollard 1980; Weller 1982; Kunze 1985; D'Asaro et al. 1995; D'asaro 1995*a,b*; Elipot et al. 2010).

We now turn our attention to examine the near-inertial event characteristics as a function of the mean background flow. The aim of this section is to determine if the frequency and amplitude of the NIO interact with the mean background flow in the observations and model as previous numerical and theoretical studies have predicted. The mean background flow is defined as the sub-inertial flow calculated from the 3 day low pass HFR and ROMS and daily ssh surface currents. A 1/3 day cut-off frequency is used since it is the frequency where the rotational component of the flow is more energetic than the divergence of the flow (Figure 2.2, Chapter 2).

The mean background flow can modify the NIOs in various ways, either by shifting their frequency (Weller 1982; Kunze 1985; Chavanne et al. 2012) or modifying their amplitude (Stern 1965; Niiler 1975; Stern 1975). Several studies have analyzed the interaction between a geostrophic flow and NIOs, but most of them assumed the background flow had small Ro or its spatial scale was much smaller or larger than the NIOs.

Over the course of the near-inertial event the field of eddy-like motion observed from the 3 day low pass data translated towards the south east at a rate of 5 km/day in the HFR observations and at 10 km/day in the ROMS simulations. The background vorticity is slightly lower in the ROMS simulations than in the HFR observations. Figure 3.11 and 3.12 show spatial maps of daily averaged relative vorticity over the near-inertial event from the HFR and ROMS 3 day low pass surface currents. Both ROMS and HFR follow a similar pattern of high positive vorticity in the south-west corner of Oahu and high negative vorticity close to the shore. Positive and negative patches of around 30 km in both model and observations are observed with Rossby numbers of $\sim \pm 0.5f$.

Theoretical predictions

According to Kunze (1985), the theoretical frequency a NIO would have in the presence of a mean flow can be obtained deriving the dispersion relation a near-inertial internal wave would have in the presence of a quasigeostrophic flow. The derivation involves all non-linear terms since it assumes both wave and quasigeostrophic flow have similar spatial scales. A

complex dispersion relation was found assuming the solution is of the form of a plane wave where the real part is the Eulerian frequency minus the Doppler shift from the mean flow and where the effective inertial frequency of the NIO is $f_{eff} = \sqrt{f^2 + f\zeta - V_x U_y + U_x V_y}$. This equation states that in a region of positive vorticity, a near-inertial wave will experience an advective rotation in addition to the planetary vorticity. Chavanne et al. (2012) expressed a similar dispersion relation in terms of normal $S_n = U_x - V_y$ and shear $S_s = V_x + U_y$ strain as $f_{eff} = \sqrt{(f + \zeta/2)^2 - (S_n + S_s)^2/4}$ where f_{eff} is the natural frequency an NIO would have in the presence of mesoscale eddies.

In figures 3.8 and 3.9 the ROMS and HFR surface currents were demodulated at trial frequencies around $\pm 0.2f$. If the NIO frequency in the presence of a quasigeostrophic followed Kunze (1985) theoretical f_{eff}, the "real" frequency of the NIO will be found at the frequencies where the demodulated near-inertial currents had maximum values over the $\pm 0.2f$ band. Elipot et al. (2010); Shearman (2005) found a qualitative agreement between the observed frequency of NIOs and the predicted frequency shift by Kunze (1985) comparing drifters with satellites and ADCP observations and Kim and Kosro (2013) with HFR surface currents off the Oregon coast.

Over the course of the near-inertial event the HFR-derived f_{eff} varied between 1.2f to 0.7f (Figure 3.8, black line). It slightly followed the contours of maximum amplitudes from the demodulated currents at trial-frequencies. For example, in the west region, maximum amplitudes were found at around $10 \, \text{cm s}^{-1}$ at f and at 1.1f, consistent with the HFR-derived f_{eff}. The largest discrepancy between f_{eff} and the frequency of maximum near-inertial amplitude was found in the north region where f_{eff} is at around 1.1f while the maximum near-inertial amplitude was found at around 0.8f.

The ROMS demodulated currents at trial frequencies had an inferior correspondence between frequencies at maximum near-inertial amplitudes and f_{eff} than in the HFR results (Figure 3.7). ROMS-derived f_{eff} over the event varied similar to the HFR observations between 1.2f and 0.7f (Figure 3.9, black line) but had less temporal variability than in the observations with most of the f_{eff} values over the near-inertial event having frequencies

larger than f.

NIOs could be interacting with a background flow at spatial scales larger than the HFR and ROMS resolution as shown by (Elipot et al. 2010) drifter and satellite observations. A time series overlapping with the HFR time period from Sep 2010 to Sep 2012 from ssh observations (Topex/POSEIDON) is used to extract geostrophic velocities and compute f_{eff} from their gradients using second order central differences in the interior and second order one-sided differences at the boundaries.

The satellite derived f_{eff} time-averaged from March 1 to March 13 is computed and plotted on Figure 3.15a. f_{eff} does not linearly increase towards the poles as f since it also depends on vorticity and strain. Typically, f_{eff} varies on spatial scales of about 50 km^2 moving throughout the HFR domain in the lapse of $\sim$ 10 km/days. f_{eff} varied between 1.06f to f over the satellite grid points over the HFR spatial domain (Figure 3.15b). Although these values do not coincide with the frequencies of maximum near-inertial amplitudes observed in the HFR and ROMS demodulated currents (Figures 3.8 and 3.9), the ROMS-derived near-inertial currents (Figure 3.9) have maximum amplitudes at frequencies larger than f. This is expected since the model resolution is lower than the HFR and should have a better correspondence with the geostrophic satellite-derived surface currents.

Kunze (1985) also noted that since regions of negative vorticity, f_{eff} is lower than f, the internal wave spectrum is enlarged and potentially more energy can be input by the wind at the ocean surface. Thus, if the waves were generated in regions of negative vorticity, trapping would occur since the lower f_{eff} of the NIOs would prevent propagation outside anticyclonic regions contrary to regions of positive vorticity. The only possible trapping in regions of anticyclonic vorticity can be observed in Figure 3.8 where from March 7 to March 8 the HFR-derived demodulated near-inertial currents were maximum in the north region at $\sim$0.8f. In the north region, f_{eff} does become less than f after March 7 in both model and observations (not satellite) but only when calculated from the HFRs it reaches values of around 0.85f.

The divergence of the background flow could also amplify or dampen the NIOs and

contribute to its spatial variation. Weller (1982), derived the classic slab layer model equations described in section 4.2 but with the inclusion of a quasigeostrophic flow in the mixed layer.

$$\frac{\partial u_m}{\partial t} - f v_m + 2 u_m U_x + v_m U_y + u_m V_y = \frac{\tau_x}{\rho_o H} \tag{3.2a}$$

$$\frac{\partial v_m}{\partial t} + f u_m + 2 v_m V_y + u_m V_x + v_m U_x = \frac{\tau_y}{\rho_o H} \tag{3.2b}$$

where (u_m, v_m) are the near-inertial currents in the mixed layer, (U, V) the divergent quasi- geostrophic flow, (τ_x, τ_y) the wind stress and ρ_o and H the sea water density and mixed layer depth. Equation 3.2 is only valid if the gradients of divergent flow are constant over the mixed layer depth and the magnitude of the background flow is large compared to that of the NIOs ($U >>> u$).

The analytical solution depends on the roots of the auxiliary equation

$$\lambda^2 + 3\lambda(U_x + V_y) + 2(U_x + V_y)^2 + U_x V_y + f^2 + f(V_x - U_y) - U_y V_x = 0 \tag{3.3}$$

where

$$\lambda_{1,2} = -\frac{3}{2}(U_x + V_y) \pm \frac{1}{2}(-4f^2 - 4f(V_x - U_y) + (U_x - V_y) + 4U_y V_x)^{\frac{1}{2}} \tag{3.4}$$

The solutions have the general form $u = Ae(\lambda t)$ and $v = Ae(\lambda t)$. They are dependent on the vorticity which shifts the frequency (as Kunze (1985)) and the divergence which could amplify or dampen the NIO. For example, at a latitude of 21°N, a divergence of -1×10^{-5} s^{-1} would increase the NI amplitude by 8% after one day and by 80% after 7 days. The divergence calculated from the 3 day low pass HFR currents shows after March 8 (Figure 3.11, third column), a correspondence between a convergence of -1×10^{-5} s^{-1} and a maximum near-inertial energy in the north region at 157.80°W. This correspondence is not observed in the ROMS simulations (Figure 3.12, third column), although the north region

does present a region of convergence half the size of the HFR divergence in March 8, the maximum amplitudes are observed away from the coast and are only larger than 10 cm s^{-1} close to the coast before March 8 2012.

Van Meurs (1998) expanding the asymptotic solution by D'asaro (1995b) found that the presence of the mesoscale vorticity gradients by a quasigeostrophic flow can affect the generation and evolution of near-inertial currents in the mixed mixed layer. He assumed the mesoscale field is stationary and unlike Kunze (1985) there is no assumption of WKB approximation which states that the scales of near-inertial currents are much smaller than the scales of the geostrophic flow. The vorticity gradients can separate higher near-inertial modes and thus increase the decay time scales as $t_n^3 = \frac{3\pi}{f_o \nabla \zeta^2 R_n^2}$ where n is the vertical mode number and R_n is the Rossby radius of deformation of mode n. This shows a faster decay of near inertial energy in regions of high vorticity gradient. Since vorticity gradients can locally reach values larger than β, the presence of a mesoscale field can affect the temporal and spatial scales of the near inertial motions. Through a numerical model experiment he showed that spatially homogeneous near inertial currents quickly become spatially variable and this variability is strongly correlated to the vorticity gradients as the phase of the NIOs get "squeezed" in regions of high vorticity gradient and the energy disappears faster outside the mixed layer because the modes of the near-inertial currents get out of phase. Young and Jelloul (1997), Klein et al. (2004), Danioux et al. (2008) also found that NIO energy is organized by the Laplacian of the vorticity rather than vorticity itself.

The ROMS and HFR gradients of vorticity calculated from the 3 day low pass surface currents are in the order of 10^{-9} s^{-1} with the model results are around half an order of magnitude larger than the observations. In both model and observations the largest values are found in the north-west corner of the HFR spatial domain. This is also the region where the slab model response had the lowest correlation with the demodulated currents and the near-inertial amplitude observed in both ROMS and HFR was lower than in the rest of the HFR spatial domain. Using Van Meurs (1998) decay scale, $t_n^3 = \frac{3\pi}{f_o \nabla \zeta^2 R_n^2}$, and as in the HFR observations $\nabla \zeta$ of 3×10^{-9} s^{-1}, and typical R_n of 1000 km and $f_o = 1 \times 10^{-5}$ s^{-1}, the

decay scale results at 5.5 days, consistent with the observed NIO duration. Although the Laplacian of vorticity from satellite observations can not be calculated close to the coast, values south of Oahu were in the order of 10^{-10} (not shown) resulting in a decay scale in the order of 30 days, not consistent with the duration of the March 2012 near-inertial event and suggesting the submesoscale mean background flow is interacting with the NIOs.

Daily snapshots of phase maps calculated as the difference between the observed NIO and the motion at f are overlay in Figures 3.11 and 3.12. After March 7, phase-contours are more organized in space both in the model and observations suggesting the generation of a near-inertial event. From March 8 to March 12 phase lines are "squeezed" in the north-west (at 158°W and 21.15°N) corner of the HFR spatial domain where the gradients of vorticity were maximum. After March 7 phase line closely followed contours of vorticity and after March 8 they slightly followed the contours of the gradient of vorticity and the Laplacian of vorticity. This is more obvious in the observations than in the model. Elipot et al. (2010) found a linear dependence between vorticity and the gradient of vorticity from surface drifters which is not observed in the HFR and ROMS data. Klein et al. (2004) found through a numerical model that NIO KE is organized by the $\nabla \zeta$ after two inertial periods consistent with our results.

3.4.4 Energy Interactions

The observed NI spatial variability in Figures 3.11 and 3.12 could be related to the energy exchange between the background flow and the NIOs. For instance, It has been shown by Whitt and Thomas (2015) that the inclusion of an unidirectional geostrophic flow in the slab model can produce an irreversible exchange of energy between the NIOs and background flow. Similarly, Jing et al. (2017) that the inclusion of a non-divergent two dimensional flow in the slab model can also produce that irreversible exchange of energy if the spatial scales of the NIO and background flow are similar.

An energy equation can be calculated by multiplying equation 3.2a by u and equation 3.2b by v. Adding the results and integrating (over a NI event) with respect to time, the

following energy budget equation is obtained:

$$E_m(t) - E_m(0) = -\int_0^t (2u_m^2 UU_x + 2v_m^2 V_y + u_m v_m U_y + u_m v_m V_x + u_m^2 V_y + v^2 U_x)ds$$

$$+ \int_0^t \frac{\tau_x u_m + \tau_y v}{\rho_o H}ds - \int_0^t r(u_m^2 + v_m^2)ds, \quad (3.5)$$

where $E_m = (u^2 + v^2)/2$ is the total near-inertial KE in the mixed layer, the first, second and third term on the R.H.S are the lateral shear production (LSP) by the background flow, the wind work (WW) and the damping parameter (DAMP). We assume that over the mixed layer u_m and v_m are the demodulated currents at f while U and V are the 3 day low pass background currents in the mixed layer.

The LSP is non-zero when there is a time integrated Reynolds stress and non-zero shear from either U_x, U_y, V_x and V_y. Numerical models studies (Whitt and Thomas 2015) have shown that in a flow with Ro $O(1)$, LSP can contribute to the energy budget of inertial motions at a magnitude equal or greater than WW. The WW is computed from the WRF wind stress and an r of 1/3 days since it produced the best results between the HFR demodulated currents and the slab model response (section 4.1).

The HFR-derived total energy budget from the R.H.S of equation 3.5 over the near-inertial event is shown on Figure 3.17 (a, b and c); the LSP and DAMP are four orders of magnitude smaller than the WW term. There are spatial differences over the HFR spatial domain of around 10 km. Although LSP and DAMP are much smaller to produce a substantial or significant impact in the total NI energy budget, negative and positive LSP maxima larger than the rest of the HFR spatial domain are observed close to the coast at 158.00°W and 157.80°W where the maximum DAMP is also found (Figure 3.17a).

The integrated over the near-inertial event time series of the R.H.S of equation 3.5 are shown on Figure 3.17c. LSP began to grow after March 6 2012 at around 157.80°W (Figure 3.17a, triangle marker), indicating an loss of energy from the NIO to the background flow. On the contrary, at 158.00°W (Figure 3.17a, square marker), energy decreased after March

6 indicating - although negligible since LSP is four orders of magnitude smaller than WW - an exchange of energy from the background flow to the NIO. The integrated WW began to grow in March 6 and oscillated between 0.2 to 0.6 m^2s^{-2} throughout the event. The total KE began to grow after the second wind maximum in both selected areas on March 9 and remained constant after March 12. The DAMP term decreased after March 6 and remained constant after March 12.

The total ROMS-derived energy budget is plotted in Figure 3.18 (a, b and c). LSP and DAMP are one order of magnitude smaller than in the HFR $O(10^{-6})$ m^2s^{-2}, consistent with the less energetic NIOS, while the WW is a factor of 2 smaller. The DAMP parameter is the smallest close to the coast and in the Penguin Bank area suggesting the model is not correctly calculating NIOs in shallow areas. As with the HFR energy budget, KE began to grow after March 9 and remained constant after March 12, 2012 (Figure 3.18d). The DAMP parameter increased offshore due to the observed increase in ROMS near-inertial currents and WW.

Whitt and Thomas (2015) found that the submesoscale geostrophic flow is a source of energy for inertial motions when R_o are $O(1)$. Although in some areas we did observe an exchange of energy from the NIOs to the mean background flow, values were orders of magnitude smaller than the remaining terms in (5) to have an impact on the NIO energy budget. Forced/Dissipating inertial oscillations will tend to damp geostrophic flows more strongly in regions of anticyclonic vorticity than cyclonic vorticity. This could be possibly shown in the North region were observations showed an increase of NI energy when f_{eff} was lower than f (Figure 3.8a) and the integrated LSP over the event had negative maximum values.

3.5 Discussions

NIOs off the south shore of Oahu, Hawaii were described from HFR and ROMS surface currents. The NIOs were variable in time and space and their characteristics were dependent on the wind forcing and mean background flow. It is important to examine the NIOs

variability since it will affect the energy budget of the ocean. Any spatial variability in the distribution of near-inertial energy, will generate divergences that affect the decay of near-inertial currents in the mixed layer and thus propagation of NIW into ocean interior (Alford 2003; Soares et al. 2016). Two issues will be discussed in this section, the discrepancies between the observations and model and the effect of the spatial scales of the NIOs into the wavenumber and wavelength characteristics.

3.5.1   ROMS and HFR comparisons

The model (ROMS) used in this study has been successful in producing the mean-flow south of the Hawaiian Islands (Matthews et al. 2012; Azevedo Correia de Souza et al. 2015). The inclusion of the HFR radial currents from KAL into the 4D-Var assimilation, reduced the variability between model and observations and yielded a better estimate of the ocean circulation around Hawaii than without radial assimilation (Azevedo Correia de Souza et al. 2015). Nevertheless, at the near inertial band we found that model and observations differ significantly even with the inclusion of both KAL and KOK radials.

From September 2010 to September 2012 several near-inertial events in the model were not observed in the observations (Figure 3.3). The ROMS near-inertial amplitudes had averaged values of around 10 cm s^{-1} with sporadic events larger than 20 cm s^{-1} throughout the two-year time record while the HFR near-inertial currents amplitudes were larger than 15 cm s^{-1} only from December to March. The discrepancies between model and observations are mostly due to the physics missing in the model by the larger resolution of the model (4 km) compared to observations (1.5 km) and to the assimilation scheme (4D-Var) used in the ROMS.

Matthews et al. (2012) found that NIOs are impacted by the 4D-Var assimilation scheme used in the ROMS around the Hawaiian Islands without radial assimilation while Azevedo Correia de Souza et al. (2015) found a better agreement over the near-inertial band between model and observations when radials from KAL where assimilated. The 4D-Var reanalysis adjusts the wind forcing, boundary and initial conditions of the model run such that the

primitive equations best represent the observations. This often adds energy into the flow in the form near-inertial energy and produces spurious NIOs which are damped close to the coast (Matthews et al. 2012). This could be the cause of the large NIOs observed in the model and not in the observations throughout the time record and could blur the seasonality not observed in the model but present in the observations. For this region, historical XBT temperature records showed a larger thermocline from November to March (not shown), contrary to the near-inertial seasonality observed where larger NIOs are associated to a smaller mixed layer depth (Weller 1985). In addition, Eich et al. (2004) found from two moorings at the eastern side of Mamala Bay in the south shore of Oahu, that in summer the water column is highly stratified compared to winter, this is consistent with the mixed layer depth calculated from the ROMS. This implicates that the large NIOs observed throughout the year in the model are not a product of an incorrect model stratification but mostly a consequence of the assimilation process. The surface forcing is not a cause of error since the WRF model used to force ROMS also produced NIOs in the slab model that were significantly correlated with the ROMS and HFRs results. This implies that the near-inertial event analyzed in this study in section 4 was wind-generated and not a process of the assimilation scheme used.

There are spatial and temporal differences between the modeled and observed wind-generated NI event described in section 4. The ROMS surface currents are currents measured over a "surface" layer which varies over space becoming smaller closer to the coast compared to the HFRs which measure surface currents over a constant layer of around 0.5 m (Stewart and Joy 1974). This could have generated larger modeled NIOs close to the coast than offshore inconsistent with our results in Figure 3.12. The 4D-Var assimilation process dampens NI energy near the islands (Matthews et al. 2012) and it is likely the cause of the low NI energy observed in the model and not in the HFRs.

The mean background flow could also modify the spatial structure and frequency of the NIOs. In particular, the spatial resolution of the model (4 km) vs the HFRs (1.5 km) could be a factor in determining the amplitudes of the background currents, since the higher

spatial resolution in the HFRs will present more submesoscale energy than the ROMS. Both model and observations present a similar spatial structure in the observed vorticity with values larger than the model. On the contrary, the divergence and gradient and Laplacian of vorticity were overestimated in the model suggesting a modification of the NIO by an incorrect modeled mean background flow. In general, the assimilation process does increase about 50% the EKE close to the islands (Matthews et al. 2012) but has similar spatial and temporal patterns as observations.

The differences in spatial and temporal resolution could also have an impact on the differences in amplitudes between model and observations in the north region over the NI event (Figure 3.8 and 9). For example, the f_{eff} calculated from ROMS has lower Rossby numbers than the HFR, so the resonant frequency of the wind could not be the same in both ROMS and HFR. If the wind forcing is narrow banded in frequency space, then the inertial response to that forcing will vary in physical space since f_{eff} varies in space, thus wind forcing will excite NIOs at f_{eff} instead of f (Whitt and Thomas 2015) and result in NIOs with similar scales as f_{eff}. Thus, NIOs can exhibit elevated near-inertial energy because of the resonance of the winds at f_{eff} instead of f and if f_{eff} is is not correctly parametrized in the model, there will be no resonance between wind and f_{eff}, precluding an increase in NI energy.

Spatial characteristics

It has been shown (Weller 1982; D'Asaro et al. 1995) that the spatial scales and advection speed of wind storms are important factors in determining the initial wavenumber of NIOs, thus resulting in NIO spatial scales in the order of 1000 km. We have shown that the spatial and temporal variability of a NI event observed in model and observations has spatial scales in the order of $\sim$20 to 40 km and is dependent on the spatial scales not only of the wind but of the mean background flow. In this section we will discuss the implications of the observed NI variability into the wavelengths.

The zonal λ_x and meridional λ_y wavelengths over the near-inertial event in March

2012 are calculated by least-square fitting the phase extracted from the ROMS and HFR demodulated currents over the longitude and latitude range. Two zonal transects were selected (Figure 3.19 and 20 b and d); one at 21.12°N and one at 20.98°N (shown on Figure 3.1c). On the northern transect (21.12°N) , the average of the hourly least-square-fits over the near-inertial event resulted in a λ_x of 206 km with little temporal and spatial variability. In contrast, at the southern transect (20.98°N) the phase is more variable in space with an abrupt change in phase at 157.90°W and an average least-square fit over the near-inertial event of λ_x 185 km. The zonal wavelengths were also calculated from the model (Figure 3.20 b and d) but for the meridional transect from 158.50°W to 157.60°W. The northern transect (21.12°N) least-square-fit resulted in an average of λ_x of 22 km while the southern transect with a λ_x of 18 km. These values are small compared to the HFR results since they encompass the 50-m Penguin Bank where there is an abrupt change of phase at 157.70°W in both northern and southern transects. If the least-square-fit is performed only over the HFR transect in Figure 3.19, the λ_x for both zonal transects is of around 200 km, consistent with the HFR results and indicating that the shallow Bank modifies the phase as shown by (Millot and Crépon 1981; Shearman 2005).

Two meridional transects were selected to calculate λ_y; one at 157.96°W and one at -157.73°W (Figure 3.19 and 20 a and c). In both model and observations, the standard deviation of the λ_y was larger than the mean, indicating variability is too large to detect any "real" wavelength characteristic. This is expected since the coast can create complicated patterns to the near-inertial variability such as convergences and divergences of the NIOs (Millot and Crépon 1981; Shearman 2005). Nevertheless values over the NI event ranged between 20 to 300 km, indicating the order of magnitude is similar to λ_x. Although the spatial variability is large, the slope is in general constant over time. The spatial variations could be associated to physical factors. In particular the abrupt change of phase at 21.1°N observed in the HFRs results could be associated to the large gradients of vorticity modifying the phase lines (Figure 3.11 and 12) (Van Meurs 1998).

3.6 Summary and Conclusions

The spatial and temporal variability of the surface NIOs off the south shore of Oahu Hawaii were investigated from HFRs and an assimilative ROMS implementation. Larger amplitudes were found in winter months when sporadic south-westerly wind bursts larger than 10 m s^{-1} were observed. During these months, inertial oscillations accounted for 25% percent of the total surface currents variance, while during summer and fall inertial oscillations only accounted for 15%. This seasonality was not observed in the ROMS near-inertial currents due to the assimilation process and the sub-grid processes captured in the HFRs and not in the model. There is strong small scale (within the HFR spatial domain) variability, such as the north sub-region (Figure 3.1a), where near-inertial variability accounted to up to 50% of the total variance.

A wind generated near-inertial event was investigated in detail. It quickly became spatially variable, with spatial scales down to ∼20 km observed in the HFR surface currents. This event had a duration of around 4 inertial periods (∼6 days) and was precluded by strong rotating winds. The maximum near-inertial amplitudes were found at around 20 cm s^{-1} in the HFR observations and 15 cm s^{-1} in the ROMS simulation. The near-inertial amplitudes were underestimated in the ROMS particularly close to the coast due to the assimilation process which dampens NIOs in shallow areas. The slab layer model resolves a significant number of the observed and model near-inertial event characteristics, strongly supporting the role of wind forcing in the generation of NIOs. Nevertheless, certain features such as the amplitude spatial variability were not seen in the slab-layer model.

The maximum HFR-derived near-inertial amplitudes over the analyzed event were found in the north region where wind resonated at an f_{eff} lower than f due to the mean background flow. This was not observed in the ROMS near-inertial currents. The minimum near-inertial amplitudes over the HFR spatial domain were found at locations where the gradients of vorticity from the mean background flow from both model and observations were maximum. Furthermore, phase lines were squeezed in areas of maximum vorticity and gradient and Laplacian of vorticity

NIO wavelengths were estimated over the near-inertial event from the phase of the demodulated currents. The λ_x was slightly variable in space, possibly due to bathymetry and the mean background flow. The average wavelengths were found at at around 200 km in both observations and model. The meridional wavelength was possibly modified by the coast but the large spatial variability precluded an accurate estimation. Estimating these numbers is important for understanding the propagation of NI energy into the ocean interior. We also calculated an energy budget for the NIOs, where the wind work (the energy input by the winds) on the NIOs was two orders of magnitude larger than the energy extracted from the background flow (LSP), in contrast to previous numerical and theoretical studies (Whitt and Thomas 2015). To have a better understanding of the NIOs variability and its energy exchange with the background flow, future studies should take into account the bathymetry and background currents at scales similar to the HFR resolution.

3.7   Appendix: Wavelet power spectrum significance test

To estimate the significant near-inertial events we follow Torrence and Compo (1998) Monte-carlo method. At each HFR and ROMS spatial grid-point the de-tided time series are randomized 100,000 times and the normalized wavelet power spectrum is computed. From each wavelet power spectrum a time-slice of scale vs power at the center of the time-series is extracted. Each time-slice is sorted into increasing order of scales where the 95% threshold is selected as the confidence limit. Values below this threshold are selected as non-significant. Figure 3.5 shows the wavelet power averaged over the near-inertial band ($\pm0.2f$) for observations and model, dashed lines indicate the 95% significant threshold. The results for the wavelet analysis over the near-inertial band did not qualitatively change for different wavelet widths (6, 8, 10 or 12) or scaling parameters.The frequency resolution for the wavelet power spectrum was of 0.042 cpd.

At each time step during the event described in section 4, the frequency with the maximum wavelet power spectrum (peak ω) was computed and compared to f_{eff} estimated from the 3 day low pass surface velocity gradients at each HFR grid point. There is a 0.98

significant correlation between f_{eff} and peak ω, values of peak ω ranged between 0.7f to 1.26f with ~50% of the values at ±0.2f while f_{eff} values range between 0.56f to 1.4f with ~20% of the values between ±0.5f.

The difference between both quantities is defined as $DIFF = \frac{f_{eff}-peak\omega}{f}$. As expected, larger DIFF is correlated with a larger Ro. The maximum positive Ro correspond to a $|DIFF|$ of 0.4 cpd. In contrast, the maximum negative Ro have a $|DIFF|$ of around 0.6 cpd. A closer examination at DIFF can be observed on Figure 3.21, where Ro is plotted as a function of $DIFF$. There is a linear dependence between both quantities and a least squared fit approximation of $DIFF = 0.36\frac{\zeta}{f} + 0.01$ similar to Elipot et al. (2010) drifter analysis.
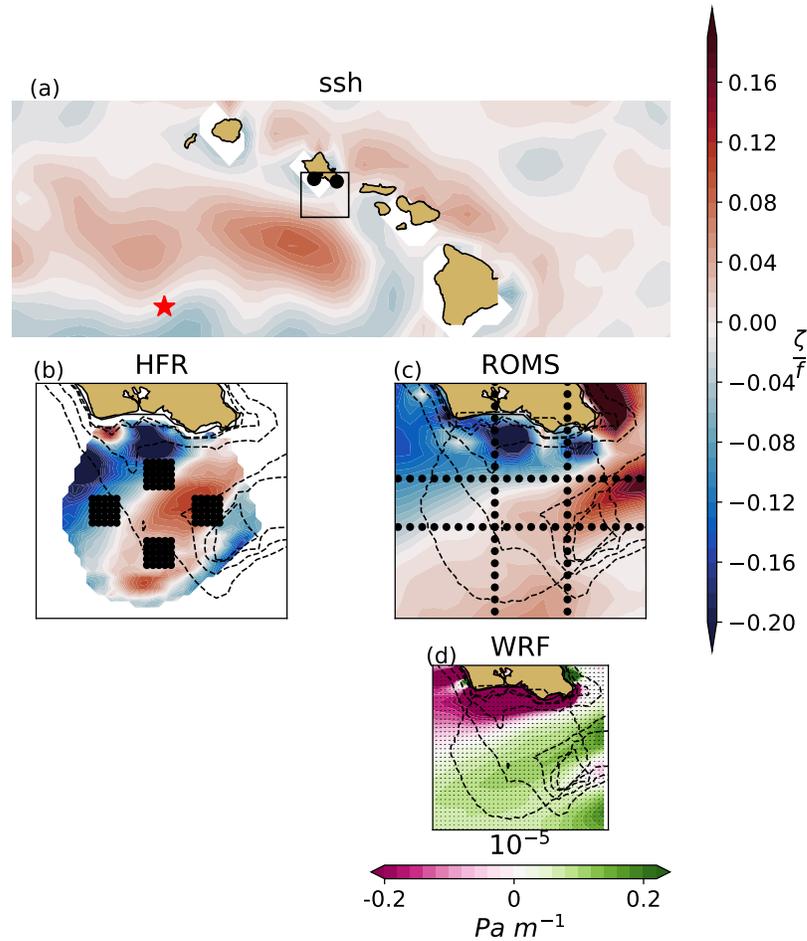
Figure 3.1: (a) AVISO SSH, (b) HFR and (C) ROMS relative vorticity normalized by f from September 2010 to September 2012. Black dots in (a) indicate the location of the two HFRs KAL and KOK. The red star indicates the location of the NDBC wind buoy. Black dots in (b) indicate the grid points over the four sub-regions used for further averaging; north, south, west and east. (d) Temporally averaged wind stress curl from the WRF model. The dashed line indicates the coverage of useful HFR data (60% of temporal coverage over the two-year period). Dashed black lines indicate the isobaths at 50, 500 and 1000 m.
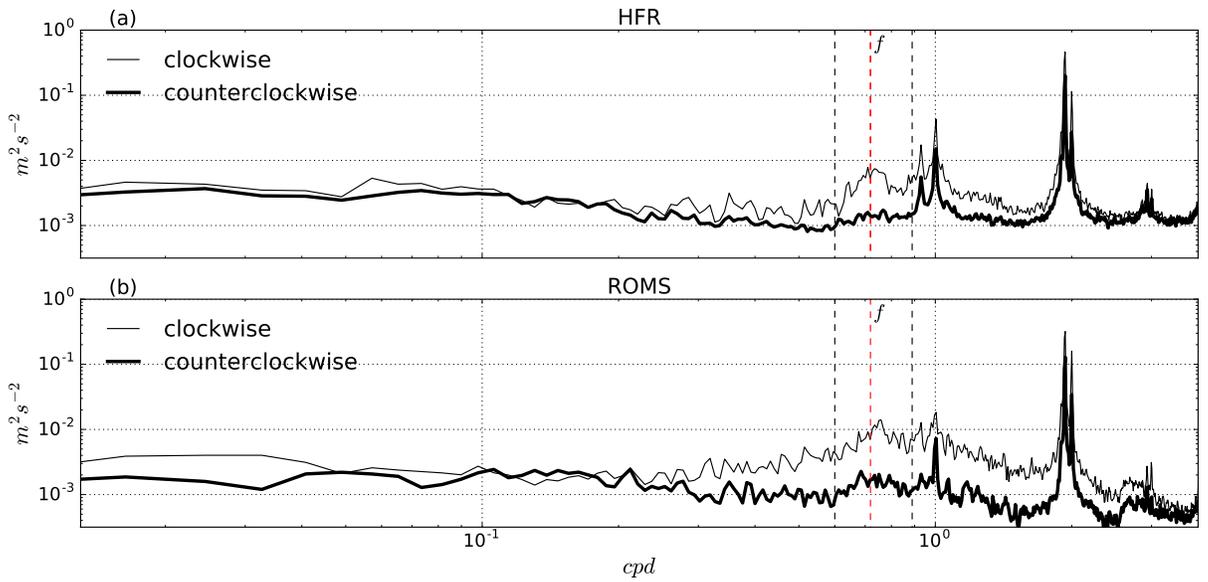
Figure 3.2: Variance preserving spectra for the two-year period from September 2010 to September 2012 averaged over the effective HFR spatial coverage denoted in Figure 3.1b from (a) HFR and (b) ROMS surface currents. The black dashed lines indicate the $\pm 0.2f$ near-inertial band and the red dashed line indicates the Coriolis frequency (f) for the HFR spatial domainof 0.71 cpd.
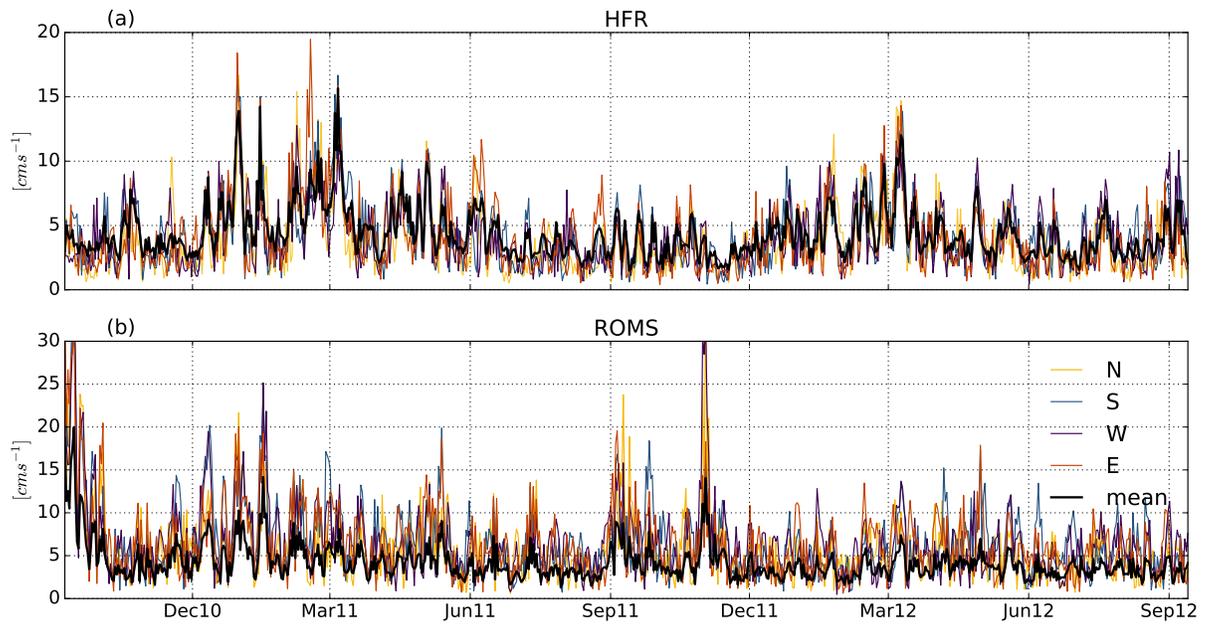
Figure 3.3: Time series of near-inertial current amplitude extracted from applying a band pass filter over the ±0.2f near-inertial band and then averaged over the four sub-regions denoted in Figure 3.1b as well as over the HFR spatial domain (black solid line) denoted in Figure 3.1b. Using (a) HFR and (b) ROMS surface currents.
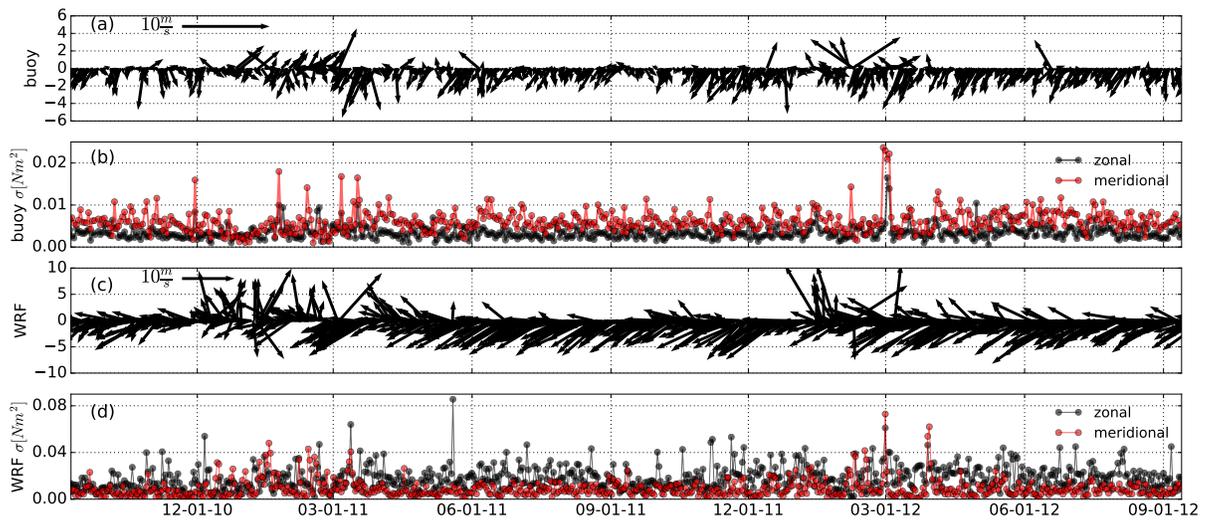
Figure 3.4: Time series of wind vectors from the NDBC buoy (a) and from the WRF grid point closest to the buoy at 19.28° (d). Also shown is the wind stress variability (as daily standard deviation) from the buoy (b) and from WRF (d).
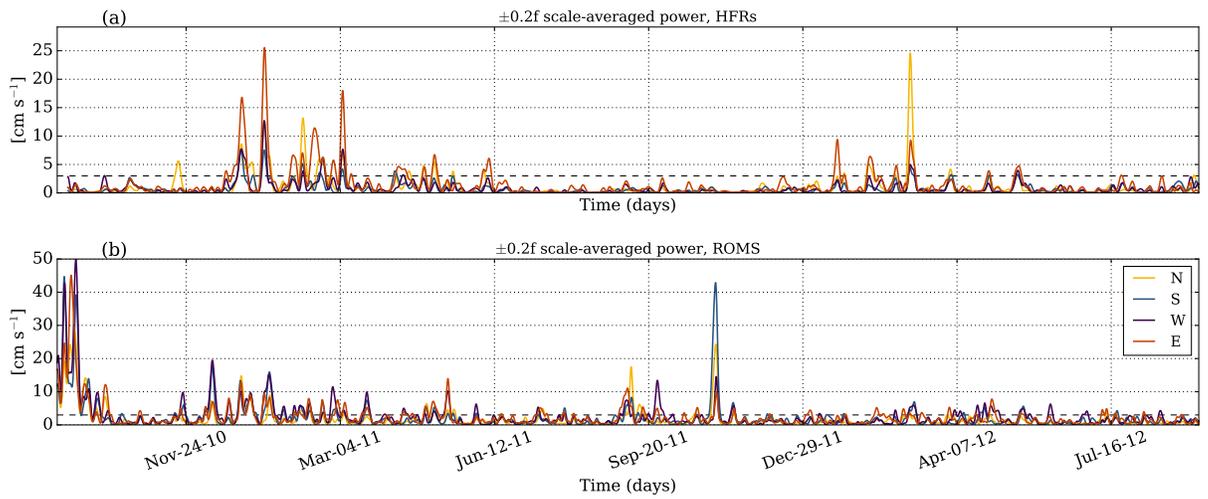
Figure 3.5: Wavelet power spectrum in the near-inertial band ($\pm 0.2f$) and averaged over the sub-regions in Figure 3.1b as calculated from (a) HFR and (b) ROMS surface currents. Note that, for visualization purposes, there is a different scale on the y axis of each panel. The dashed line indicates the 95% significant level explained in Appendix A.
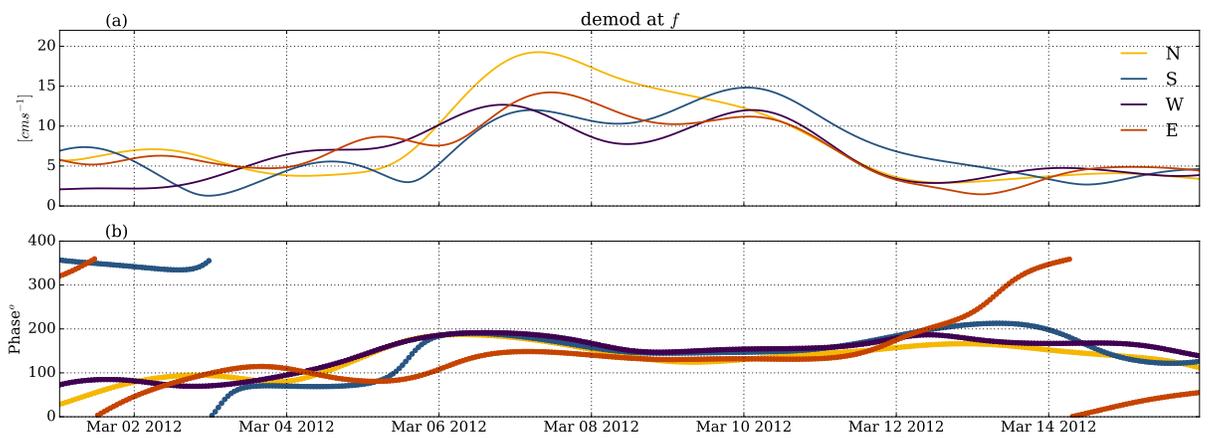
Figure 3.6: (a) Demodulated current amplitude and (b) phase using hourly detided surface currents averaged over the sub-regions shown in Figure 3.1b during the near-inertial event described in section 4.
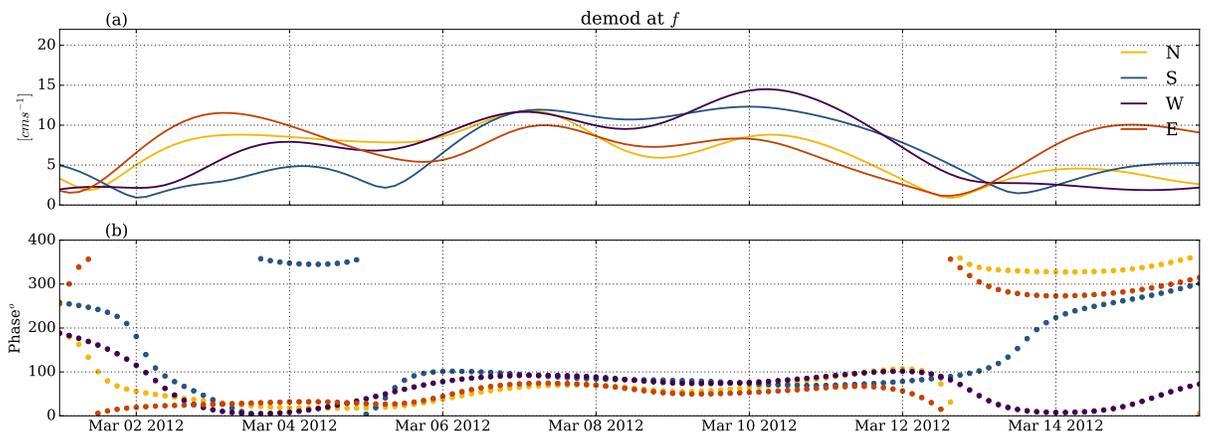
Figure 3.7: As Figure 3.6 but for ROMS surface currents interpolated into the HFR grid points.
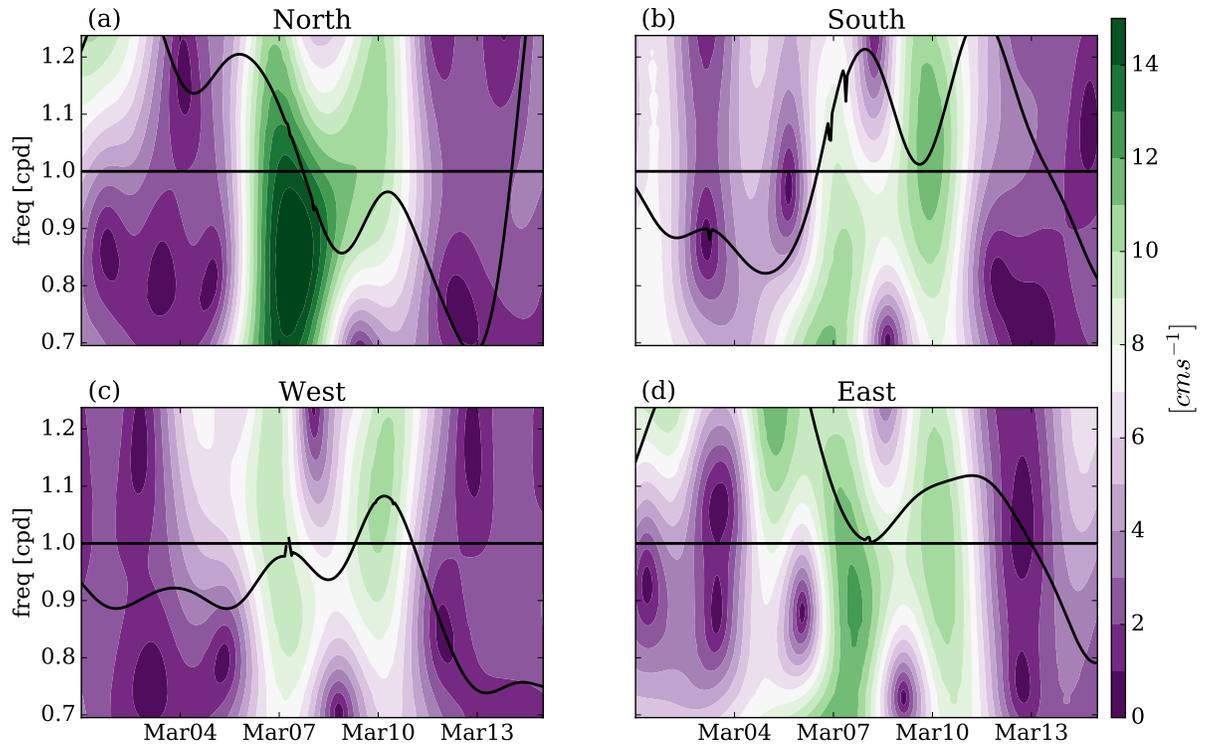
Figure 3.8: Demodulated hourly detided currents at trial frequencies $\pm 0.2f$ during the near-inertial event described in section 4. The demodulated currents are averaged over the four sub-regions (a) North, (b) South, (c) West and (d) East. The black solid line denotes the value of f_{eff} (Kunze 1985) calculated from the 3 day low pass surface currents.
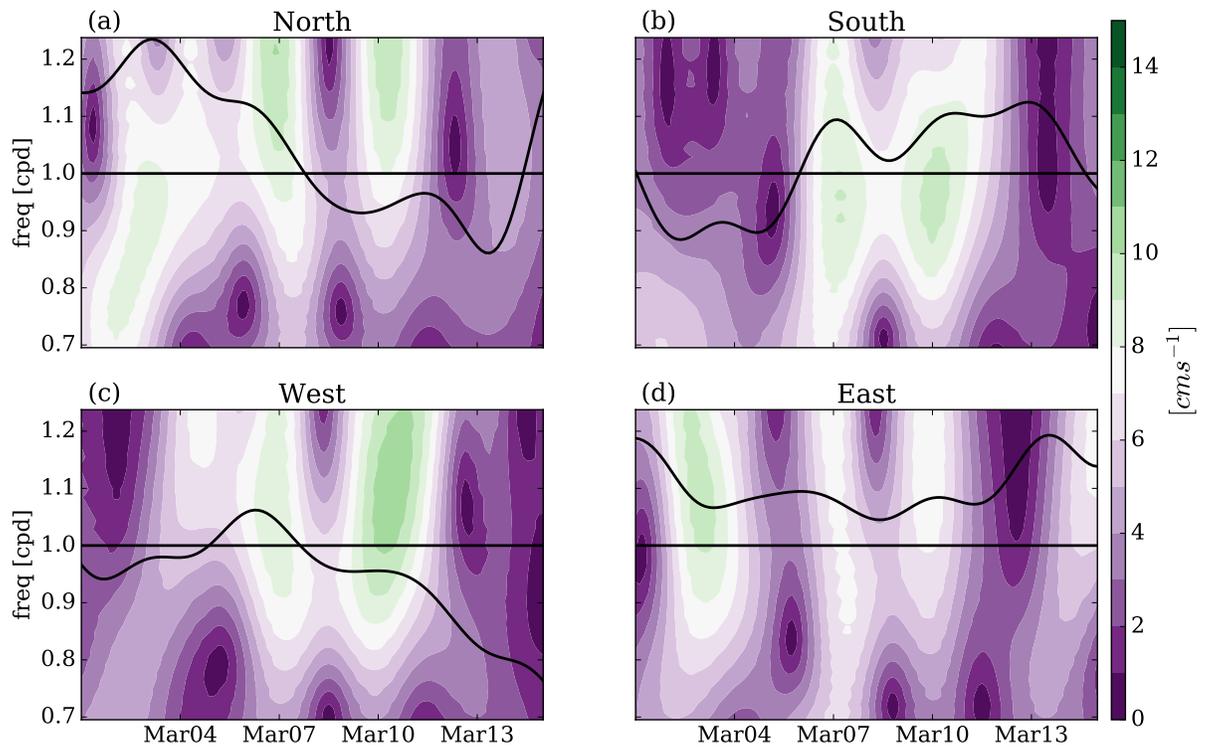
Figure 3.9: As with Figure 3.8 but for ROMS surface currents interpolated into the HFR grid points.
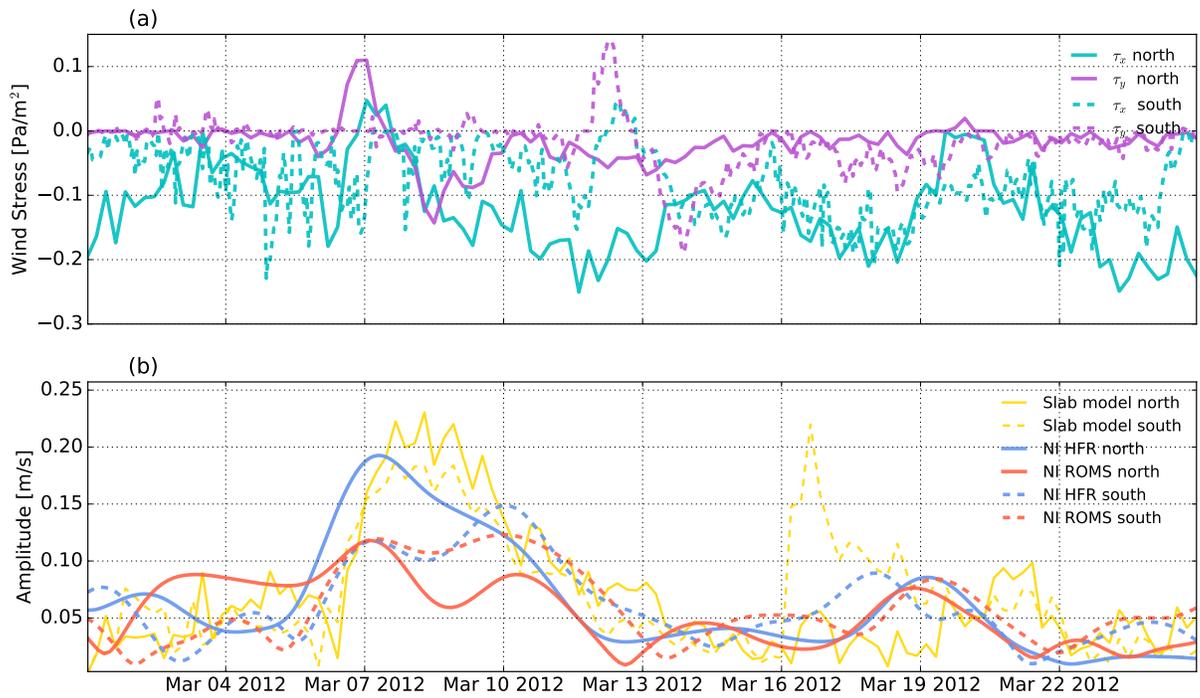
Figure 3.10: Time series of (a) wind stress vectors from the WRF wind model and (b) slab model currents. For comparison, demodulated HFR and ROMS currents for the north (solid line) and south (dashed lines) sub-regions are shown Figure 3.1b. Demodulated currents from sub-regions east and south are not shown since they are similar to demodulated currents at the south sub-region.
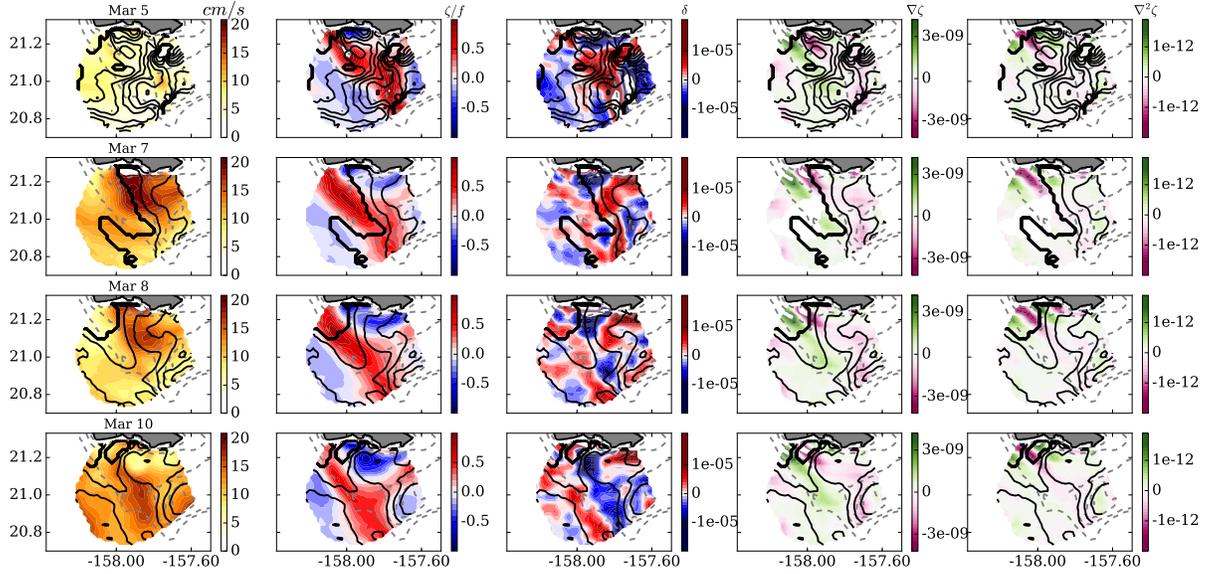
Figure 3.11: Snapshots of (first column) near-inertial amplitude extracted from the HFR hourly currents demodulated at f during the near-inertial event described in section 4. (second column) Snapshots of relative vorticity normalized by f, (third column) divergence, (fourth column) gradient and (fifth column) Laplacian of vorticity extracted from the 3 day-day low pass HFR surface currents. Black solid contours in all figures denote near-inertial phase lines every 20°. The dashed grey lines represent the isobaths at 50, 500 and 1000 m.
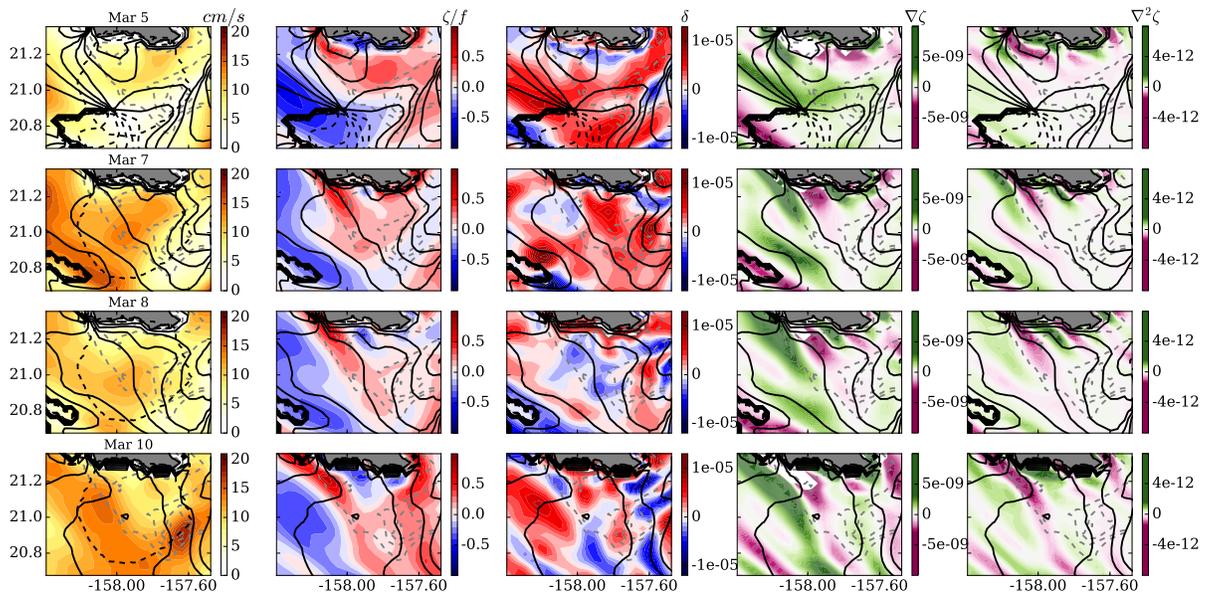
Figure 3.12: As with figure 3.11 but using ROMS surface currents. Dashed black lines in the first column indicate the 60% coverage of available data from the HFR.
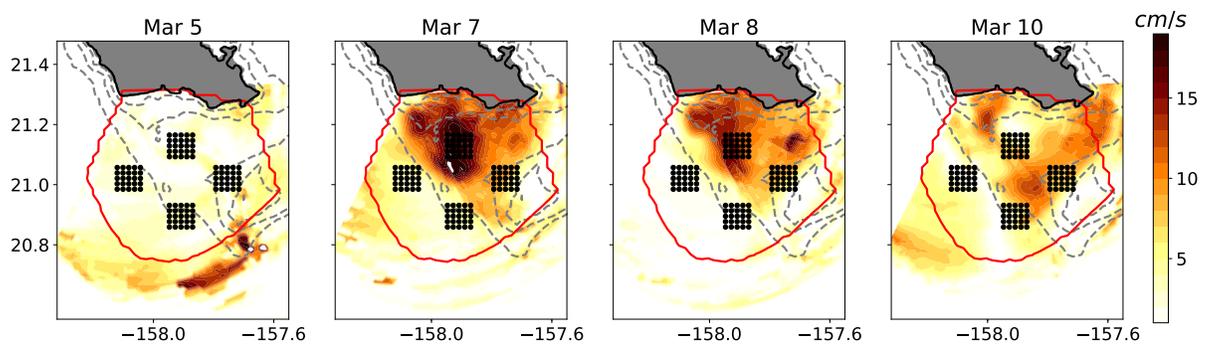
Figure 3.13: Snapshots of near-inertial amplitude extracted from the KAL HFR hourly radial currents demodulated at f during the near-inertial event described in section 4. Red lines indicate the coverage of useful HFR data (60% of temporal coverage over the two-year period).
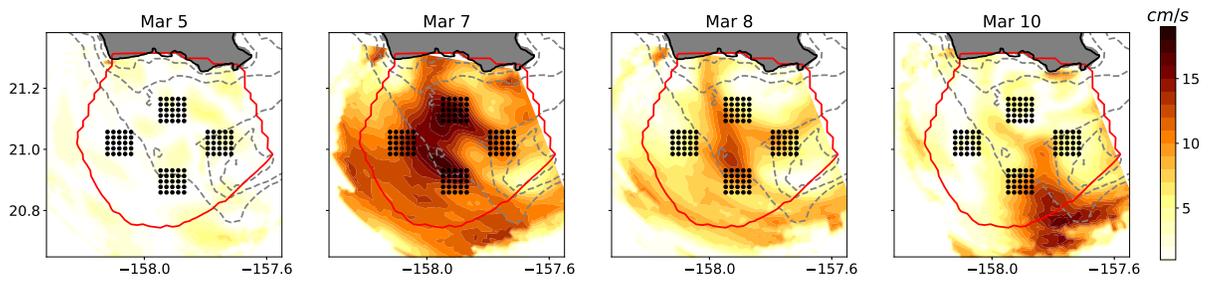
Figure 3.14: As with figure 3.13 but from KOK HFR hourly currents demodulated at f.
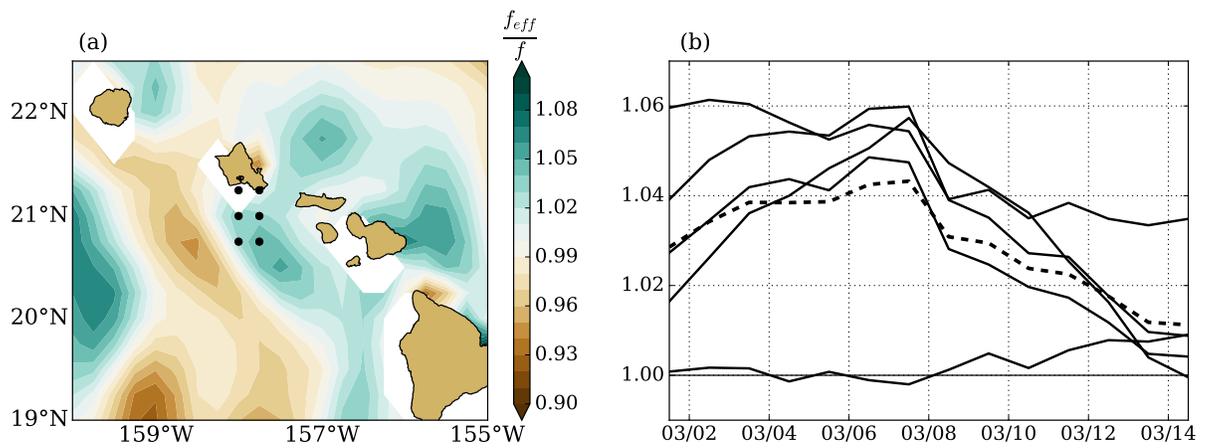
Figure 3.15: (a) f_{eff} averaged over the near-inertial event from March, 1-15 2012. The f_{eff} is calculated from the geostrophic currents extracted from SSH AVISO satellite observations. (b) Time series of satellite-derived f_{eff} from the SSH grid points falling into the HFR spatial domain shown in (a). The dashed black line indicate the average of the selected grid points shown in (a).
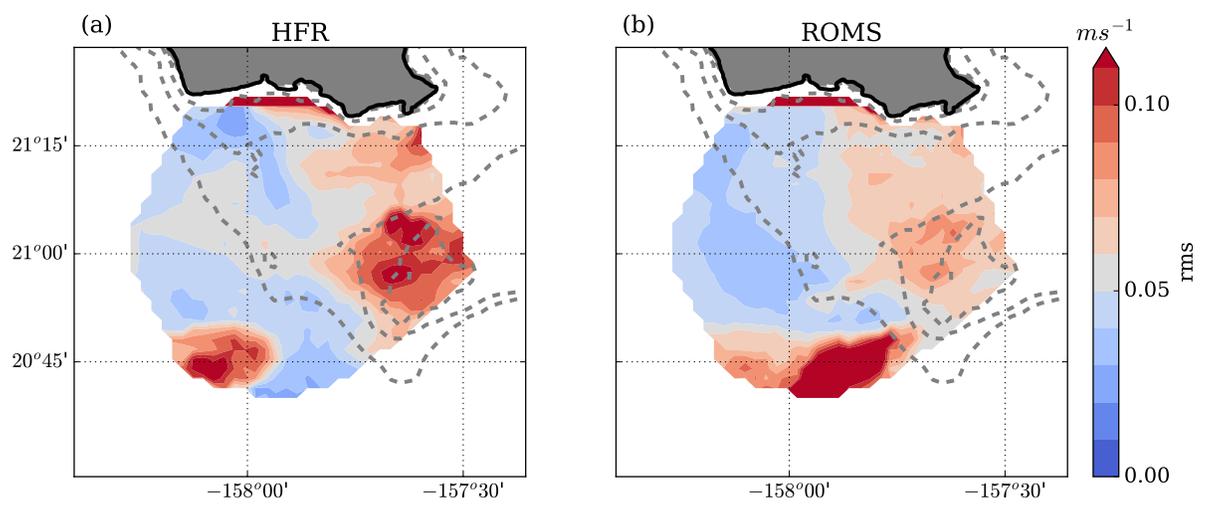
Figure 3.16: RMSD values between the slab layer model near-inertial currents and (a) HFR near-inertial currents, and (b) ROMS near-inertial currents, during the event in March, 4-12 2012.
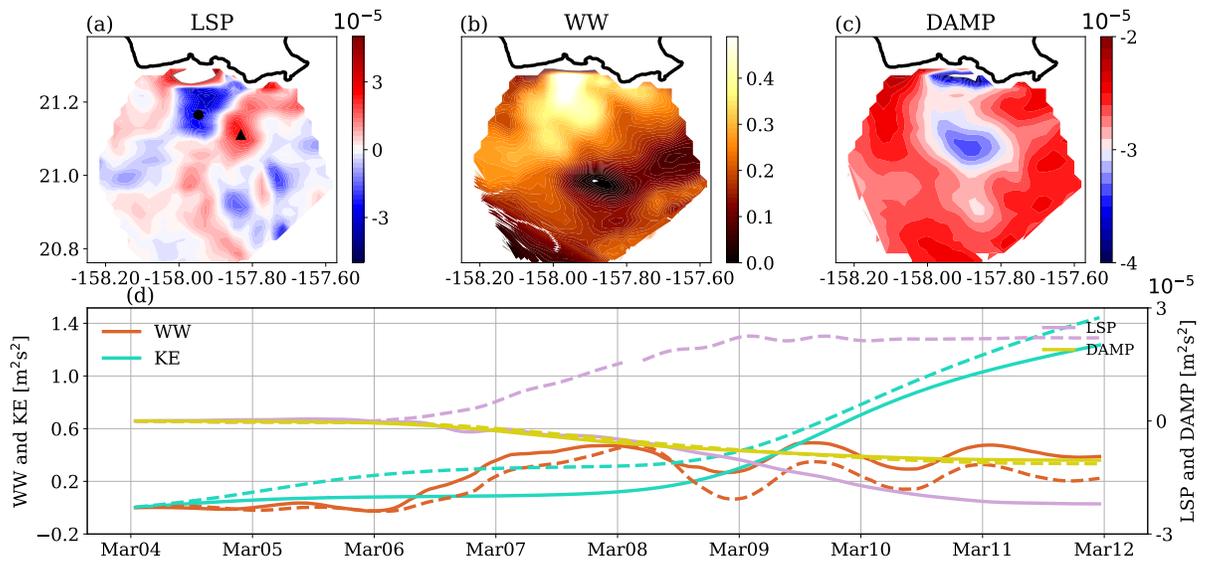
Figure 3.17: Integrated HFR-derived energy budget terms from the R.H.S of equation(5); (a)Lateral Shear Production (LSP), (b) Wind Work (WW) and (c) Damping (DAMP). (d) Time series of the energy budget terms at the grid points shown in (a) (triangle marker in (a) corresponds to dashed line time-series and circle marker in (a) correspond solid line time-series). Units are in m^{2}s^{-2}.
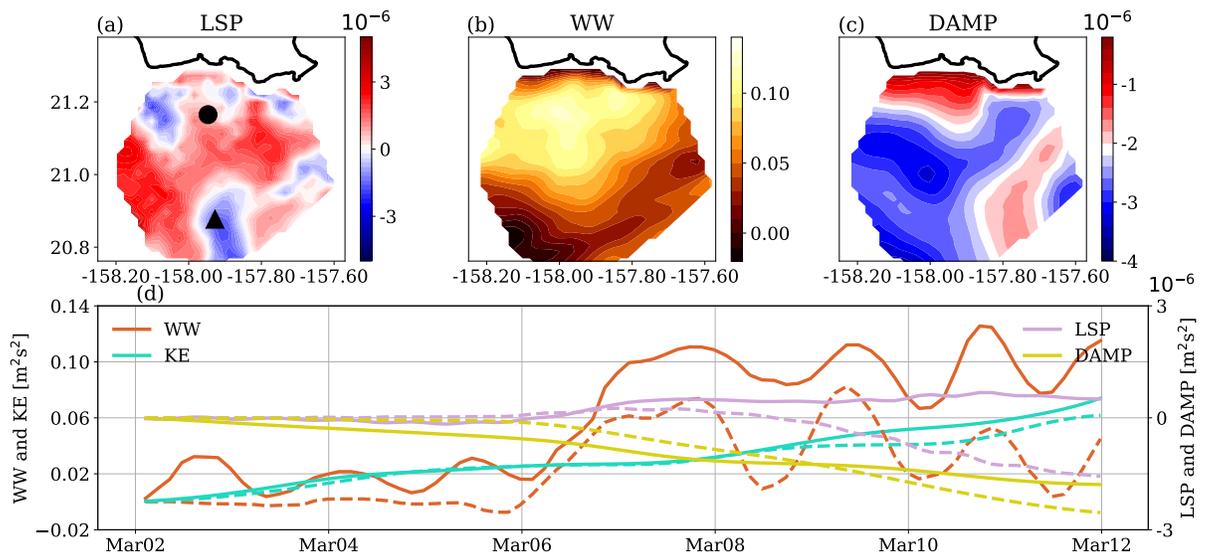
Figure 3.18: As with figure 3.17 but calculated from ROMS surface currents. Note that in (a) selected grid points are different from Figure 3.17a since the location of the maximum values between observations and model differs.
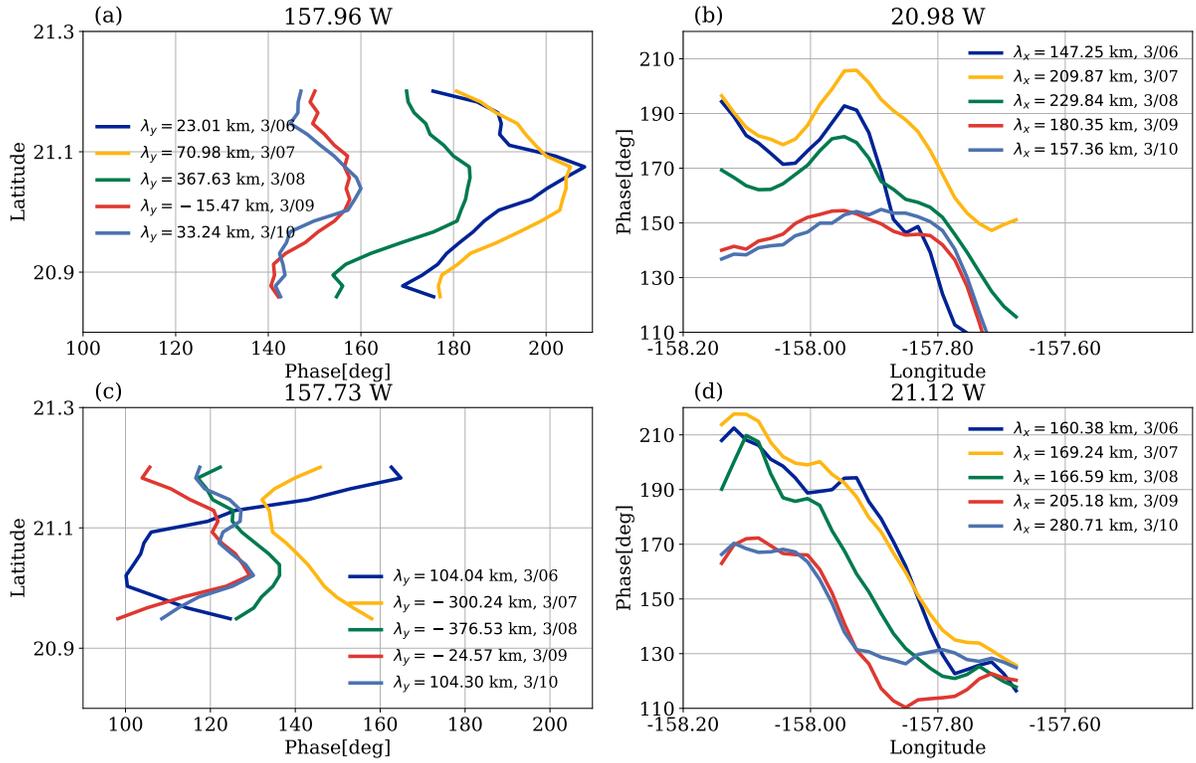
Figure 3.19: Zonal λ_x (a and c) and meridional λ_y (b and d) wavelengths estimated as the slope of the phase, calculated from a least-square-fit of the HFR surface currents demodulated at f. λ_y is calculated over the meridional transects at -157.96° (a) and -157.73° (c) and λ_x over the zonal transects at 20.98° (b) and 21.12° (d). These transects are shown on Figure 3.1c (note that only part of the transect that falls into the HFR spatial coverage in Figure 3.1c is used to calculate the phase). Colors indicate various snapshots at certain times during the near-inertial event in March 2012 described in section 4.
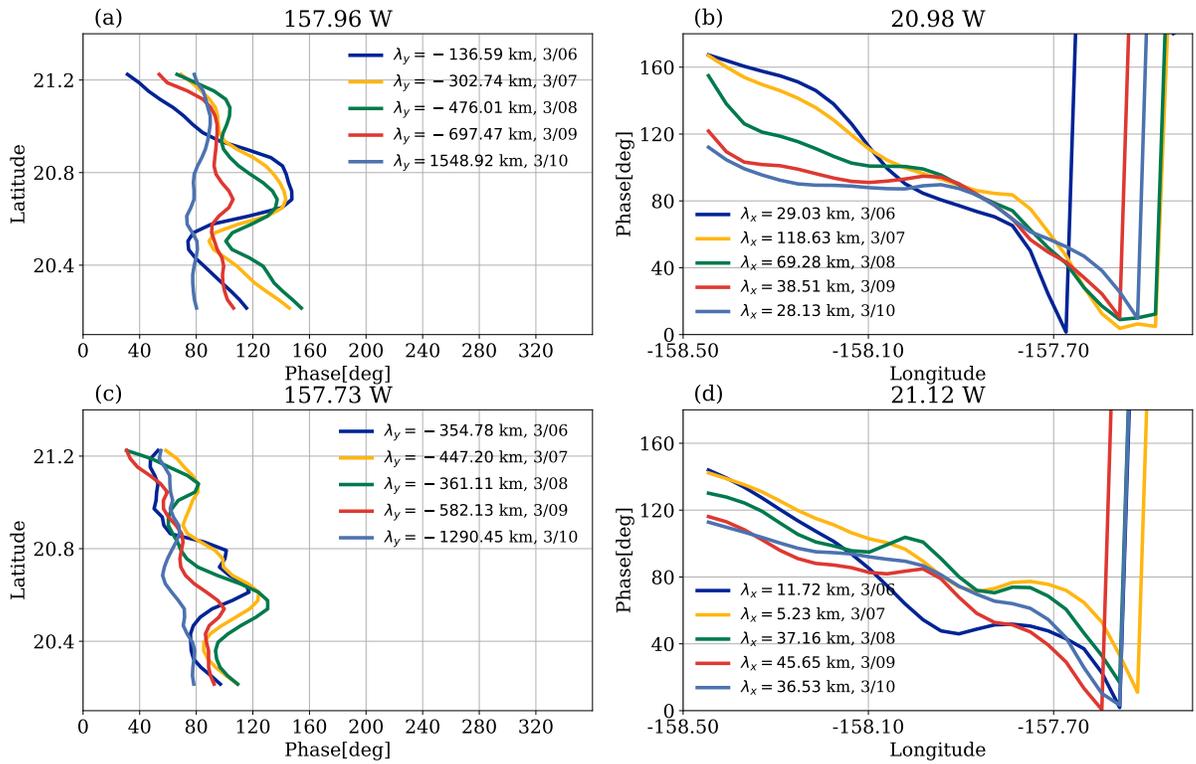
Figure 3.20: As with figure 3.19 but calculated using ROMS demodulated currents at f. Note the y and x axis cover the ROMS spatial coverage.
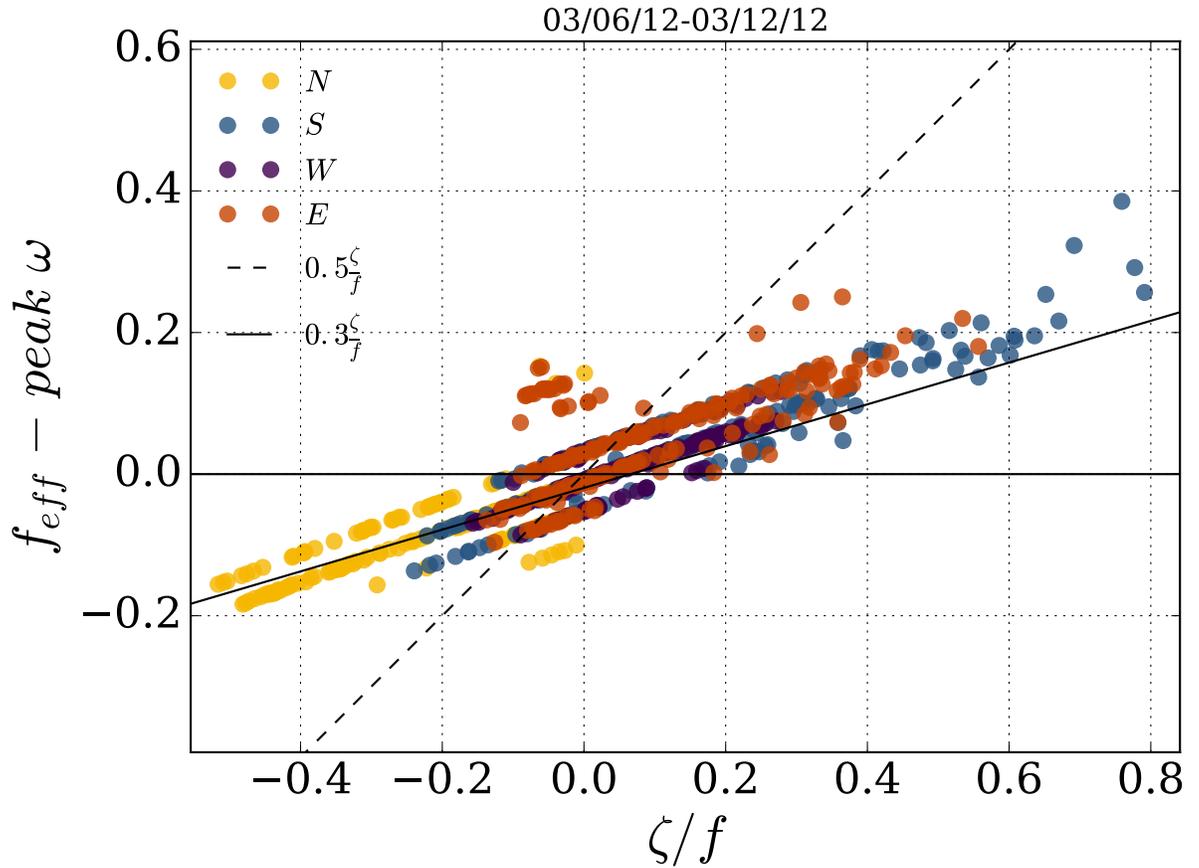
Figure 3.21: Rossby number versus $DIFF = \frac{f_{eff} - peak\omega}{f}$ for the areas selected in Figure 3.1b. Rossby number and f_{eff} are calculated from the 3 day HFR-derived low pass surface currents while peak ω is taken as the frequency where the wavelet power spectrum amplitudes are maximum during the near-inertial event. Dashed and solid black lines indicate the least-square fit of y=0.3$\frac{\zeta}{f}$ and y=0.5$\frac{\zeta}{f}$.

CHAPTER 4
INTERACTIONS BETWEEN SUBMESOSCALE EDDIES AND THE MEAN BACKGROUND FLOW.

4.1 Introduction

Submesoscale processes in the upper ocean are associated with the presence of lateral density gradients, vertical shear, weak stratification and a small Rossby radius based on the mixed layer depth. They have preferred spatial patterns of fronts, filaments, and vortices (McWilliams et al. 1998) and are associated with ageostrophic circulations. These ageostrophic circulations lead to large vertical velocities with orders of magnitude of about 10^{-3} m s^{-1}, an order of magnitude larger than the vertical velocities observed in the mesoscale circulation.

The submesoscale regime in the ocean is characterized by $O(1)$ Rossby numbers and horizontal spatial scales smaller than the first baroclinic deformation radius (Capet et al. 2008; Thomas et al. 2008). At these scales, breakdown between gradient wind balance and quasi-two dimensional mesoscale and three dimensional scale turbulence exist side by side (McWilliams et al. 1998). The resulting forward energy cascade provides a mean to dissipate large and mesoscale geostrophic energy or motions. That is, energy from the larger scales is transferred to a scale where mixing can occur and release potential energy to restratify the upper ocean (Capet et al. 2008). Submesoscale processes play an important role in the vertical flux of mass, buoyancy and tracers. They are crucial to the biological and chemical cycles of the ocean as they exchange nutrients and biogeochemical tracers between the interior and the surface mixed layer.

The submesoscale flow can exhibit locally unbalanced behavior like baroclinic instabilities with large Rossby numbers or by ageostrophic instabilities. Callies et al. (2015) found that the predominant dynamics of submesoscale processes are mesoscale eddy-derived surface frontogenesis and baroclinic instabilities in the mixed layer. Shcherbina et al. (2013) and Richman et al. (2012) found that other high-frequency motions like tides and mesoscale

straining can contribute to the submesoscale variability.

Most of the submesoscale dynamics studies have been made with models (Capet et al. 2008; Gula et al. 2014; Mahadevan and Tandon 2006; Molemaker et al. 2015; Dauhajre et al. 2017) with few observational studies (Soh and Kim 2018; Shcherbina et al. 2013; Mensa et al. 2018; Rocha et al. 2016). Submesoscale observations are limited because they require instruments to resolve processes with spatial scales smaller than 10 km and sample at high frequencies

The objective of this chapter is to describe submesoscale processes with spatial scales of less than 4 km from the two years of HFR and ROMS surface currents off the south shore of Oahu, Hawaii described in Chapters 2 and 3. We will first briefly describe the data used (Section 4.2), followed by a description of the submesoscale currents in the area (Section 4.3). We then focus on a positive vorticity filament routinely observed off the southwest coast of Oahu in both model and observations (section 4.4). The south west corner of Oahu (Barbers Point) can act as a headland. East of the headland the observed filament followed the 500 m isobath suggesting important topographic effects. Filaments like these sometimes can fragment into a train of submesoscale vortices as a result of an instability process (Gula et al. 2014). The generation and amplification process of this vortical feature are investigated with a local eddy-mean flow energy budget analysis. We will finish this study by exploring the kinetic energy wavenumber spectra to investigate the governing dynamics of the submesoscale in the area in an statistical sense, in particular if they are consistent with the local eddy-mean analysis of the observed filament. Conclusions and future work are presented in the last section (section 4.5).

4.2   Data and Methods

Two years of HFR data south shore of Oahu Hawaii from September 2010 to September 2012 alongside an implementation of an analysis and forecast system using the Regional Ocean Modeling System (ROMS) around the Hawaiian Islands are used in this study. Figure 4.1 shows the location of the two radars in Kalaeloa (KAL, 21°18 N, 158°5 W) and in Koko

head (KOK, 21°26 N, 157°42 W), covering the 670 m deep Kaiwi channel, and the shallow 50 m Penguin bank. Only HFR data within the thin blue line in Figure 4.1 is used in this chapter. The processing techniques were identical as those described in Chapters 2 and 3. The assimilative oceanic model used in this study (described in Chapters 2 and 3) is a free-surface, hydrostatic, primitive equation model discretized with a terrain-following vertical coordinate system (Shchepetkin and McWilliams 2005).

4.3   Submesoscale currents

Hourly surface currents off the south shore of Oahu Hawaii display rich submesoscale structures with scales of less than 20 km and lasting less than 24 hours. These patterns sometimes are interweaved with the low-frequency and large scale currents like the westward Hawaiian Lee Current described in Castillo-Trujillo (2014) and Chapter 2. In particular, in the southwest coast of Oahu close to the KAL site (Figure 4.1) a south-eastward flow with positive vorticity of up to 2f is observed during the two years of available HFR surface velocities.

This south-eastward flow west of Barbers Point (21.25°N, 158.2°W) detaches from the coast and generates areas of strong positive vorticity and shear. These regions of positive vorticity sometimes evolve into vortices that move southward until they are sheared away or disappear from the HFR spatial domain. These eddies have shapes and sizes that change while they propagate from their generation site at Barbers Point towards Penguin Bank. Similarly, weaker cyclonic eddies are sometimes observed in the model detaching from a positive vorticity filament with characteristics similar to observations but lasting less than two days and with maximum Rossby numbers of 0.5f.

Statistics of the HFR and ROMS surface currents from a region south of Barbers Point (A, 21.25°N, 158.2°W) and at the center of the HFR spatial domain (B, 21.25°N, 158.0°W) are plotted in Figure 4.2. Vorticity (Figures 4.2a and 4.2b) and divergence (Figures 4.2b and 4.2e) follow a normal distribution with vorticity (ζ/f) skewed to the anticyclonic side at region B while at region A only 60% is larger than 0. The strain (σ/f) at region A (Figure

4.2b) follows a χ distribution as observed in ADCP observations in the North Atlantic (Shcherbina et al. 2013) and ranges from 0 to 1.5f with 20% of the total larger than 0.5f. Region A shows larger positive vorticity, strain and divergence than in region B. At region B only 6% of the total strain (Figure 4.2e) is larger than 0.5 while only 20% of the vorticity is larger than 0.

As with observations, model vorticity (Figure 4.2g and 4.2j) and divergence (Figures 4.2h and 4.2k) follow a normal distribution while strain a χ distribution (Figures 4.2i and 4.2l). In general, smaller Rossby numbers are seen in the model statistics than in the observations. Nevertheless a similar spatial variability to the observations is seen in the model; at region A, 46% of the ζ/f is larger than 0 while 8% of the σ/f is larger than 0.5. At region B, 26% of the ζ/f is larger than 0 while only 1% of the σ/f is larger than 1.

Additional insight into the structure of submesoscale turbulence is gained from the relationship between vorticity versus strain and divergence (Figure 4.3). In region A, strong positive vorticity is associated with high strain rate and approached a pure shear relationship ($|\sigma = \zeta|$), indicating that cyclonic vorticity occurred predominantly in fronts. This is not observed in region B. The model (Figure 4.3b), does show this linear relationship ($|\sigma = \zeta|$) at region A but not as pronounced as in the observations but, in contrast, is mostly found in areas of negative vorticity. In both A and B, regions negative vorticity surface currents presented a more mesoscale eddy-like structure, with smaller divergence and strain. This is consistent with previous model studies (Mahadevan and Tandon 2006) where they predict weak positive divergence associated to negative vorticity.

4.4   Case study: Submesoscale cyclonic eddy

A positive vorticity filament detaching from Barbers Points was observed in both model and observations in March 2012 (Figure 4.1). The filament was parallel to the 500 m isobath and once it detached from the coast, a cyclonic vortex was formed. In this section, we explore the vortex generation and propagation mechanism.

From March 13 to March 19, a cyclonic vortex with Rossby $O(1)$ and strain larger

than 0.5 was observed moving from the south-west shore of Oahu towards Penguin Bank. Daily snapshots of observed and model vorticity and strain overlaid with surface currents are plotted in Figures 4.4 and 4.5. The ζ/f maximum increases strongly detaching from Barbers Point. The peak value is reached immediately were the flow loses contact with the coast. The filament became unstable 24 hours after generation. The vortex grew from ~11 km diameter on March 14 to a maximum of ~33 km diameter in March 17 (Figure 4.4c). At this time, the vortex had maximum Rossby numbers of 1.4 at the core and a translation speed of 5 km day^{-1} towards Penguin Bank.

A positive vorticity filament is also observed in the model off the coast of Barbers Point with strain rates larger than 0.5f (Figure 4.5). A southeast current flowing parallel to the west coast of Oahu is observed when the filament appears. After March 17 (Figure 4.5c), the filament detached from the coast and followed the 1000 m isobath and in March 19 (Figure 4.5d) the filament propagated southward maintaining its positive vorticity. The signature of the filament and vortex is also observed in the Okubo-Weiss parameter ($\sigma^2 - \zeta^2$) and strain (Figures 4.6 c-f). In March 13 at 0:00 the filament had negative Okubo-Weiss parameter and maximum strain of ~1.2f with positive vorticity of about 1.5f. A negative Okubo-Weiss parameter and positive vorticity is an indication of formation of cyclonic vortical structures.

One can estimate how gesotrophically balanced (Coriolis and pressure gradient are the dominant forces) the submesoscale vortex is by the level of agesotrophy of the flow (Capet et al. 2008; Chavanne et al. 2010). Through the balance in which Coriolis and pressure gradient plus an advective centrifugal force dominate the divergence of the horizontal momentum, viz:

$$g\nabla^2\eta = \nabla \cdot (\mathbf{u} \cdot \nabla\mathbf{u}) + f\zeta, \tag{4.1}$$

where $\mathbf{u}$ and ζ are the surface currents and vorticity, respectively, and η the sea level anomaly. The degree of ageostrophy (the degree to which a flow departs from geostrophic balance) is then given by:

$$\epsilon_{geo} = \frac{|-\nabla_h \cdot (\mathbf{u} \cdot \nabla\mathbf{u}) + f\zeta - g\nabla^2 h|}{|\nabla_h \cdot (\mathbf{u} \cdot \nabla_h \mathbf{u}_h)| + f|\zeta| + |g\nabla^2 h|} \tag{4.2}$$

where $g\nabla^2 h$ is estimated from the residual of the R.H.S of equation 4.1. When ϵ approaches 1 the flow is unbalanced and when ϵ approaches 0 the flow is geostrophically balanced.

In March 13 at 0:00 the filament of positive vorticity was surrounded at the north and south by an unbalanced flow (Figure 4.6g). This unbalanced flow kept surrounding the filament 12 hours later (Figure 4.6h) when the vortex was detached from the filament. Over the life cycle of the vortex, ϵ at the periphery of the vortex was closer to 1 while at the center of the vortex was closer to $\sim$0. In contrast, the filament observed in the model is only unbalanced downstream of the flow (Figure 4.10g).

4.4.1 Generation mechanism

The presence of large-scale strain can stabilize the horizontal shear instability of a vorticity filament in a barotropic flow (Dritschel et al. 1991). To distinguish the large scale strain induced by the non-divergent flow from the strain induced by the divergent flow, the flow and subsequent strain are decomposed into divergent and rotational components following a Helmholtz Decomposition (Smith 2008). The flow decomposition at the times of maximum instability is shown in Figure 4.7; the large scale rotational flow produced a strain field smaller than 0.6f while the divergent circulation produced the filament and the large strain therein. Furthermore, the vorticity of the filament (Figures 4.4(a-d)) was always larger than 1f, that is, larger than the background strain to meet any inflection-point criterion for filament stability (Dritschel et al. 1991). Negative regions of $(f + \zeta) - \sigma$ around the filament in March 13 (Figure 4.8) indicate a loss of balance in the vicinity of the filament (McWilliams et al. 1998) which is consistent with Figures 4.6 (g-h) where an ageostrophic circulation is observed at the periphery of the filament before it becomes unstable. Once the vortex was fully developed, the Okubo-Weiss parameter became negative at its core and positive at its periphery (Figure 4.6f) suggesting the filament was destroyed by the vortex generation.

Vertical profiles of model relative vorticity of the transect parallel to the filament (Figure 4.1, dashed line) are shown in Figure 4.9. On March 13, an area of positive vorticity of up

to 0.8f from the surface down to ~80 m is observed. The surface expression of vorticity at this time is shown in Figure 4.5a. The filament in the model propagates southeast ward at a speed of 10 km day^{-1} similarly observations but the instability and vortex formation is not observed in the model.

4.4.2 Instability and Vortex Formation

The sequence of ζ/f contours shows the positive vorticity filament becoming unstable and breaking into a submesoscale vortex (Figure 4.4). To identify the nature of the instability process, we compute the kinetic energy conversion terms between the filament and its perturbations in a local reference frame aligned with the filament (Figure 4.11a). The eddy kinetic energy (EKE) is written as EKE $= 0.5(\overline{u'}^2 + \overline{v'}^2)$, where (u, v) are the horizontal velocities perpendicular and parallel to the filament (x, y), positive in the onshore and upstream directions, respectively. The over bar denotes an along filament average (shown in Figure 4.1 as a dashed line) and the prime, fluctuations relative to that mean (Gula et al. 2015). Energy conversion terms are computed according to Harrison and Robinson (1978) where the rate of change of EKE is $\frac{\partial EKE}{\partial t} = HRS + VRS + VBF$. The conversion from mean to eddy kinetic energy is composed of HRS and VRS where:

$$HRS = -\overline{u'^2}\frac{\partial \overline{u}}{\partial x} - \overline{u'v'}\frac{\partial \overline{u}}{\partial y} - \overline{v'^2}\frac{\partial \overline{v}}{\partial y} - \overline{u'v'}\frac{\partial \overline{v}}{\partial x} \qquad (4.3)$$

is the conversion from mean kinetic energy to eddy kinetic energy due to horizontal shear stress (product of mean shear and Reynolds stresses) and

$$VRS = -\overline{u'w'}\frac{\partial \overline{u}}{\partial z} - \overline{u'w'}\frac{\partial \overline{v}}{\partial z} \qquad (4.4)$$

is the conversion from mean kinetic energy to eddy kinetic energy due to vertical shear stress. The eddy potential to eddy kinetic energy (eddy buoyancy flux) conversion is :

$$VBF = \overline{w'b'} \qquad (4.5)$$

where w is the vertical velocity anomaly and b the buoyancy anomaly. Predominance of $HRS > 0$ (assuming VRS is small) or $VBF > 0$ indicates the eddy generation mechanism is primarily a barotropic or baroclinic instability. If VRS is the predominant term it will indicate a Kelvin-Helmholtz instability.

The instantaneous along front integrated surface energy terms are shown in Figure 4.12a and 12b. When the filament appears on March 13 12:00, HRS was less than 0, it remained negative until 24 hours later when it became positive and grew to about 1×10^{-6} m^{3}s^{-3} throughout the cross-shore transect. From the vortex generation time on March 14 to March 17, the EKE grew to up ~0.20 m^{3}s^{-2}. At those times, the HRS was always positive on the east side of the cross-shore transect (east of 157.94^{o}W, Figure 12b) indicating the energy source for the eddy growth is the horizontal shear of the mean flow.

The surface energy budget terms calculated from the model are plotted in Figure 4.12d. HRS was always positive where the filament was observed (west side of the cross-shore transect), with magnitudes similar to observations (1×10^{-6} m^{2}s^{-3}). The EKE in the model was positive throughout the instability period but about half the magnitude of the observed EKE. The EKE and HRS grew to a maximum in March 14 12:00. Contrary to observations, HRS became negative in March 17, indicating EKE is decaying and the energy was transferred to the mean flow.

Although a full grown eddy was not observed in the model, it is useful to estimate the HRS, VRS and VBF over vertical layers. Instantaneous EKE budget terms integrated over the first 100 m and in the along shore direction are shown in Figure 4.13 at the time of instability observed in the HFR surface velocities. HRS became positive in March 14 (Figure 4.13b, solid line) while the EKE increased to about 0.7 m^{4}s-2 (Figure 4.13a, solid line). Other sources like the VRS and VBF are smaller and do not contribute to the balance, suggesting that a baroclinic instability is an unlikely process at the moment of instability. Instantaneous vertical transects of HRS integrated in the along shore direction are plotted in Figure 4.14. HRS is confined to the upper 20 m on March 14 with values of about 2.5×10^{-6} m^{3}s^{-3}. After March 14, HRS decreased and remained negative until March

17. Model results suggest that although the HRS is the lead contributor to the EKE in the upper 20 m, the barotropic shear instability forms a weaker vortex than the eddy seen in the observations, suggesting model diffusion could play a role in the development of the vortex. Therefore an implementation of the model with increased vertical and horizontal resolution could produce the observed vortex and thus confirm if is generated by a barotropic shear instability at the ocean surface.

The barotropic shear instability could have been triggered by frontogenesis. Strong frontogenic action can generate narrow regions in which lateral shear and relative vorticity become very large producing lager ageostrophic circulations (Capet et al. 2008). A strong ageostrophic circulation was observed at the periphery of the filament (Figure 4.6g-h) with regions of high strain and vorticity, indicating the possibility of surface density fronts (Capet et al. 2008). Observations in the vertical and a model with improved vertical and horizontal resolutions are necessary to calculate if frontogenesis triggered the barotropic shear instability described above.

Furthermore, a sequence of daily satellite SST snapshots shows the evolution and propagation of the eddy (Figure 4.15a-d). On March 13, when the filament appears in the HFR spatial domain, the south east ward surface current is advecting warmer water than the rest of the water downstream of the south-east flow, with a temperature difference between the filament and its periphery of about $0.6°C$. On March 14, when the vortex was fully formed, this "warmer" water is advected to the periphery of the vortex. Cold ($23.8°C$) upwelled water at the center of the eddy is observed with a shallow warm ($24.2°C$) area surrounding the vortex core. Maps of model temperature and density at the moment of maximum instability are shown in Figures 4.15e and 4.15f. The advection of warmer water from the northwest coast of Oahu is not observed off the coast of Barbers Point but at around 15 km south of it ($21.1°N$), indicating that, in the model, frontogenesis does not occur when the positive vorticity filament appears.

4.4.3 Topographic generation

Submesoscale currents observed close to the coast of Oahu are frequently in contact with the seafloor as observed from the model vertical transects of relative vorticity and surface velocities close to the shore. Currents tend to follow topographic contour lines to conserve potential vorticity (Pedlosky 1987). Oceanic currents can also separate behind an island, headland or submerged bump [e.g. Dong et al., 2007], as well as along a continuous coast because of the changing wind stress curl boundary curvature away from the downstream flow direction and also due to an internally generated adverse pressure gradient (Haidvogel et al. 1992; Kiss 2002).

The model showed the flow on the west side of Oahu is aligned with the coast when the positive vorticity filament appeared. This filament became unstable by the horizontal shear of the mean flow. Previous section suggested frontogenesis associated with this filament could have triggered the lateral strain necessary to produce a barotropic shear instability. We now investigate the influence of the coast and topography on the flow and the production of horizontal shear.

A boundary current moving cyclonically around an island can generate high positive relative vorticity close to the shore as is observed in the HFR and the model. The sloped turbulent bottom boundary layer also provides a source of potential vorticity (PV) (Rhines 1998), which can be stripped off by the current and injected in the ocean interior. PV can be defined as $q = \omega \cdot \nabla b$, the dot product of the absolute vorticity $\omega = f + \nabla \times \mathbf{u}$ with the gradient of buoyancy $b = -g\frac{\rho}{\rho_o}$, where f is the Coriolis parameter, ρ the in situ density, ρ_o the mean reference density and g the gravitational acceleration.

The bottom drag against the slope amplifies the cyclonic shear by generating large relative vorticity within the slope turbulent bottom boundary layer. The flow interacts with the topography through a vertical bottom boundary condition related to turbulent bottom stress, which exerts a drag on the lowest layer. If this vertical boundary layer is over a sloping boundary like the topography off Barbers Point, then the vertical shear also implies a horizontal shear. Figure 4.16 shows an instantaneous along filament vertical

transect of PV from the model at the moment of instability (March 14, 00:00). PV of around $1.5 \times 10^{-8} \text{s}^{-3}$ is observed close to the coast at 100 m depth. This region of large PV could have been generated by the vertical and horizontal shear from the slope interacting with the currents. An improved model with significant grid stretching near the bottom so that the boundary layer profile is reasonably well resolved as in Gula et al. (2015) would be necessary for a complete analysis of bottom vorticity generation in the area. At present, we suggest that frontogenesis in combination with PV generated by bottom drag off Barbers Point could have triggered the horizontal shear instability described above.

4.5 Kinetic Energy spectra

Theoretical predictions for the oceanic horizontal wavenumber spectra at scales between 1 and 200 km are reviewed in Callies et al. (2015), Soh and Kim (2018), and Rocha et al. (2016). We will summarize the most relevant theories to our results and the assumptions under which they are obtained.

The two turbulence theories invoked in the submesoscale range are interior QG (Quasigeostrophy) and SQG (surface quasigeostrophy). QG is the asymptotic theory for 3D atmospheric and oceanic flows with strong rotation and stratification. It predicts a k^{-3} slope for forward energy cascade (large to small scales) and a $k^{-5/3}$ for inverse energy cascade (small to large scales) for scales smaller than the injection scale (scale at which both forward and inverse processes occur, often taken to be the most unstable wavelength due to baroclinic instability) (Charney 1971; Vallis 2006). Under the same assumptions, SQG theory predicts a $k^{-5/3}$ for forward and a k^{-1} for inverse energy cascades. SGQ theory is primarily driven by density evolution processes at the boundaries and its concentrated in a single vertical level near the surface (Lapeyre and Klein 2006; Klein et al. 2009). In geostrophic turbulence (non-divergent to leading order), isotropic and one-dimensional wavenumber spectra should follow the same power law (Callies et al. 2015). Furthermore, Charney (1971) found a relationship between the v along shore ($\hat{S}_{va}$) and u cross shore ($\hat{S}_{uc}$) velocity variance spectra through the scaling exponent $\hat{S}_{uc} = n\hat{S}_{va}$ where n is extracted from

the power law k^{-n}. Thus, the ratio $R = \hat{S}_{uc}/\hat{S}_{va}$ is a simple diagnostic to interpret how divergent the flow is. In this section, this ratio, alongside the wavenumber KE spectra decay slope are used to interpret the submesoscale flow governing dynamics.

We present wavenumber spectral estimates for the HFR u and v surface velocity components. The spectra are averaged over the two year period (Figure 4.17) and over two seasons (winter-spring and summer-fall, Figure 4.18). The spectra are computed from the cross and along-shore transects depicted in Figure 4.1 (S^{ua}, S^{uc}, S^{va}, S^{vc}), where the subscripts denote the (u) and (v) surface components and the (a) along and (c) cross-shore transects. In the selected transects, HFR surface velocities had a low GDOP and more than 60% of the data over the two-year period was available.

The wavenumber spectra averaged over the two-year period (Figure 4.17) are steep at scales smaller than 35 km and flatten out at scales larger than that. This flattening is mostly due to the finiteness of the transects, i.e. a window effect. Rocha et al. (2016) found this flatness in ADCP wavenumber spectral estimates for scales larger than 200 km due to the instrument resolution. We therefore only discuss results at scales smaller than 25 km. The $\hat{S}_{uc}$ (green line) and $\hat{S}_{vc}$ (pink line) KE spectrum are flatter at scales larger than $\sim$20 km while the $\hat{S}_{ua}$ (blue line) and $\hat{S}_{va}$ (orange line) spectrum are flatter at scales larger than $\sim$30 km. All the spectra follow a slope closer to the k^{-3} power law. The $\hat{S}_{uc}$ spectra is the most energetic of all computed spectral estimates, while the $\hat{S}_{va}$ spectra is the less energetic of all.

The ratio (R) of $\hat{S}_{uc}$ to $\hat{S}_{va}$ wavenumber spectra is about 2.5 at scales of 20 km, 1.25 at scales of 10 km and increases to 10 at scales smaller than 10 km. In general, the spectra of all components is consistent with predictions of isotropic interior QG turbulence at scales between $\sim$20 to $\sim$10 km with slopes following a k^{-3} power law (Figure 4.17). Note that the $\hat{S}_{uc}$ slope is closer to following the $k^{-2.5}$ power law, consistent to the ratio of 2.5 at scales of around 20 km, indicating non-divergent flow is predominant at those scales.

To assess the effect of seasonal variability on the submesoscale dynamics, in particular the occurrence of the observed submesoscale eddies in winter and spring (of which the previ-

ous case study is an example of), the spectrum are averaged over winter-spring (January to June) and fall-summer (July to December) months (Figure 4.18). In winter-spring (Figure 4.18a), the spectra follow a decay slope closer to the k^{-3} power law. In both the winter-spring and fall-summer spectrum averages, the $\hat{S}_{uc}$ is the most energetic while the $\hat{S}_{va}$ is the less energetic of all. The fall-summer estimates are steeper than the winter-spring for all the four KE spectrum estimates.The main difference between seasons is found in the $\hat{S}_{ua}$ and $\hat{S}_{vc}$, where $\hat{S}_{ua}$ is more energetic than $\hat{S}_{vc}$ in the winter-spring average while the opposite is true for the fall-summer average.

In the winter-summer averages, the ratio between the $\hat{S}_{uc}$ and the $\hat{S}_{va}$ spectral estimates is 3 at 20 km and increases to 6 at all scales smaller than 20 km. This indicates that according to $\hat{S}_{uc} = n\hat{S}_{vc}$, at scales smaller than 20 km, the assumption under which QG and SQG are established might be invalid and other processes may be at play. It is therefore, unclear weather interior QG is an appropriate framework at scales smaller than 20 km and if the relatively shallow coastal setting might be influencing this behavior. The ratio of $\hat{S}_{uc}$ to $\hat{S}_{va}$ was 2.5 at scales of 20 km, and as with the winter-spring average estimates, it increased to around 6 for all scales smaller than 20 km. Although anisotropies may lead to a ratio different from 3 or 2, depending on the slope, differences in wavenumber spectral estimates are expected in isotropic turbulence. The decomposition of the flow into horizontally rotational and divergent components (Figure 4.7) indicates that horizontally divergent flows, which appear quite energetic in HFR current could be responsible for the discrepancies between R and n and thus confirms that ageostrophic motions contribute significantly to the upper ocean variability (Ferrari and Wunsch 2010; Wunsch 2013). In concert with this idea, we tend to observe ageostrophic currents associated with submesoscale eddies in winter and spring months, when the KE wavenumber spectra are flatter.

In summary, kinetic energy wavenumber spectra south shore of Oahu are reminiscent of predictions of isotropic interior QG turbulence, this may represent the oceanic responses to low-frequency and synoptic-scale forcing (wind-storms) (Callies et al. 2015). All of the spectral estimates follow slopes between k^{-2} and k^{-3} for scales between 20 and 5 km except

in fall and summer where the spectrum becomes steeper at scales shorter than 10 km. This activity suggests QG and SQG may be an inappropriate framework at these scales. Since the surface current decomposition indicates divergent motions are at play, the steep slope and power ratios could be associate to the presence of anisotropy. This anisotropy could be due to the influence of the coast on the mean flow. The $\hat{S}_{uc}$ has more variance that the rest of the estimated spectra in all seasons, suggesting the along-shore currents are dominant because coastal flows tend to be parallel with the isobaths (Pedlosky 1987).

Our observations suggest that the KE decay slope in winter and spring are flatter than the rest of the seasons due to regional submesoscale processes like the 10 km vortex formed by a barotropic instability. A model study by Richman et al. (2012) found that high-frequency motions such as low mode internal tides flatten the near-surface spectra such that the effect of ageostrophic motions can be more pronounced in well-known internal tides hot spots like the vicinity of the Hawaiian archipelago.

Furthermore, the ratio of $R = \hat{S}_{uc}/\hat{S}_{va}$ (R = n; if non-divergent) does not always follow the relationship found by Charney (1971), suggesting agesotrophic circulations are significant across all ranges of scales. A more accurate assessment of seasonality at those scales would require longer time series and HFRs with a spatial resolution larger than the ones used in this study (1.5 km). Callies et al. (2015) reported that the spectral decay slopes of KE become steeper in summer than in winter as the instabilities within the shallower mixed layer in the summer are easily damped out. He found the decay slope in summer close to k^{-3} between 20 to 200 km and k^{-2} in the length scale below 20 km. Kim et al. (2017) found from HFR observations decay slopes between k^{-3} and $k^{-2.5}$ and steeper decay slopes in winter than in summer due to a front associated with regional currents off the East coast of Korea.

4.6   Summary and Conclusions

Two years of HFR and ROMS surface ocean currents on the south shore of Oahu, Hawaii at spatial resolutions of less than 4 km provided the first evidence of the nature of submesoscale

variability around the Hawaiian Islands. The observed vorticity, divergence and strain probability density distributions were computed for two different areas 25 km apart (shown in Figure 4.1). In the region close to the south west coast of Oahu vorticity distribution was symmetric while 25 km away from the coast, the distribution was skewed towards negative vorticity.

This spatial variability was mainly due to the presence of positive vorticity filaments separating from Barbers Point and becoming unstable rolling up into vortices. The submesoscale vortices are important in this area since they will affect vertical and cross-shelf exchanges with the adjacent shelf water, with potentially important dynamical and ecological implications. For instance, SST observations showed a vortex transporting colder and warmer water from the west coast of Oahu towards Penguin bank.

These filaments of positive vorticity are routinely observed off the southwest coast of Oahu. They are produced by the cyclonic shear of the south eastward flow and the absence of significant large scale strain preventing their stabilization (Dritschel et al. 1991). A filament observed in March 2012 was investigated in detail. This filament rolled into a vortex and translated towards Penguin Bank at a speed of 5 km day^{-1}. It was generated at 158.1°W and 21.2°N on March 13 (Figure 4.4a), this filament became a full vortex 24 hours later (Figure 4.4b) with its center at 157.9°W and 21.15°N. From March 15 to March 17 the vortex was surrounded by negative vorticity of ∼-0.5f while at the center of the vortex, vorticity reached up to ∼1.5f. The eddy translated towards Penguin Bank after March 15 while increasing its size. After March 17, it was squeezed between the 50 m and 1000 m isobath and ultimately it was sheared apart at around 20.8°N (Figure 4.4d). According to your diagnostic energy budget, he vortex was formed by a barotropic shear instability and grew to about ∼30 km in diameter due to the loss of energy from the mean background flow to the vortex. The actual vortex generation mechanism likely combined boundary currents separation from the coast, frontogenesis and production of positive vorticity along the slope.

The submesoscale flows roughly scale with the mixed layer deformation radius (Thomas et al. 2008). For the region south of Oahu we estimate $L_{ml} = N_{ml} H_{ml}/f = 2.5 \times 10^{-5} \times$

$100/5.2 \times 10^{-5} = 50$ km were N_{ml} is the mean stratification frequency obtained from a 10 year average of temperature and salinity observations at station ALOHA (22.75^oN, 158^oW; (Karl and Lukas 1996)) and H_{ml} is the mean mixed layer depth calculated from ROMS and glider observations. Given this scale, the mixed layer submesoscale processes are resolved by the HFR and ROMS ocean currents used in this study.

Although the model did show a filament of positive vorticity south west coast of Oahu, an instability was not observed due to the model resolution and consequential use of horizontal diffusivity (4 km in model vs 1.5 km in observations). Gula et al. (2016) found that in a ROMS simulation with 1.5 km spatial resolution, cold filaments are damped by horizontal diffusion when the scale of the filaments and eddies comes close to the grid scale, they were not able to reproduce submesoscale frontal eddies in the Gulf Stream until they reduced the spatial scale of the model to 1 km. For this study, a model with an improved spatial resolution will produce sharper vorticity and strain gradients that can lead to more realistic levels of the horizontal shear instability as seen in the HFR observations.

The process of topographic vorticity generation can be viewed as generic for boundary slope currents moving anticyclonically around a basin with the flow having the coast on its left in the Northern Hemisphere, generating strong positive vorticity within the bottom boundary layer. The flow can then separate due to complex topography and can form coherent submesoscale cyclonic vortices as the ones observed in this study. The slope at the south west coast of Oahu is possibly a strong and sustained source of potential vorticity when the flow moves anticyclonically around Oahu. The model showed a region of positive vorticity from the surface down to 100 m where the filament was observed in the HFR surface velocities. A model with grid stretching near the bottom is needed to produce an accurate representation of vorticity induced by topography near the coast.

The wavenumber KE spectra estimates have decay slopes following a k^{-3} and k^{-2} power laws at length scales between 5 to 40 km, consistent with interior QG theory and previous numerical and observations studies. The ratio $R = \hat{S}_{uc}/\hat{S}_{va}$ does depart from geostrophic turbulence theory predictions at certain times of the year and as the length scale decreases.

Ageostrophic motions account for a significant percentage of the near-surface kinetic energy and this percentage increases at scales shorter than 10 km generated at the headland of barbers point. A slight seasonality is observed with stronger submesoscale activity in winter and spring. Although Callies et al. (2015) associated this seasonality to less stratification and deeper surface mixed layers in strong baroclinic currents, we believe, that for the south coast of Oahu, this increase in variance is due to the submesoscale eddies observed at scales of 10 km. These eddies are produced by a barotropic shear instability associated with shear produced by frontogenesis and the flow interacting with the coast at Barbers Point. We find that submesoscale coastal processes on the south shore of Oahu, Hawaii are influenced by a range of dynamical processes such as barotropic and baroclinic instabilities, frontogenesis and interaction with the inflection points of an island and topography. It is not clear what are the main factors of submesoscale variability around Hawaii. This problem deserves further investigation with higher resolution models than the one used in this study and a longer HFR time series.

Submesoscale eddies like the one described in this chapter have strong implications for the biological production south shore of Oahu, Hawaii. The cold core of cyclonic eddies is a result of upwelling of cold water. The upwelling in the core of the eddy pumps nutrient-rich deeper waters towards the surface, resulting in high levels of ocean productivity. The eddy can also dominate cross shelf exchange processes transporting water from the northwest coast of Oahu towards Penguin Bank.
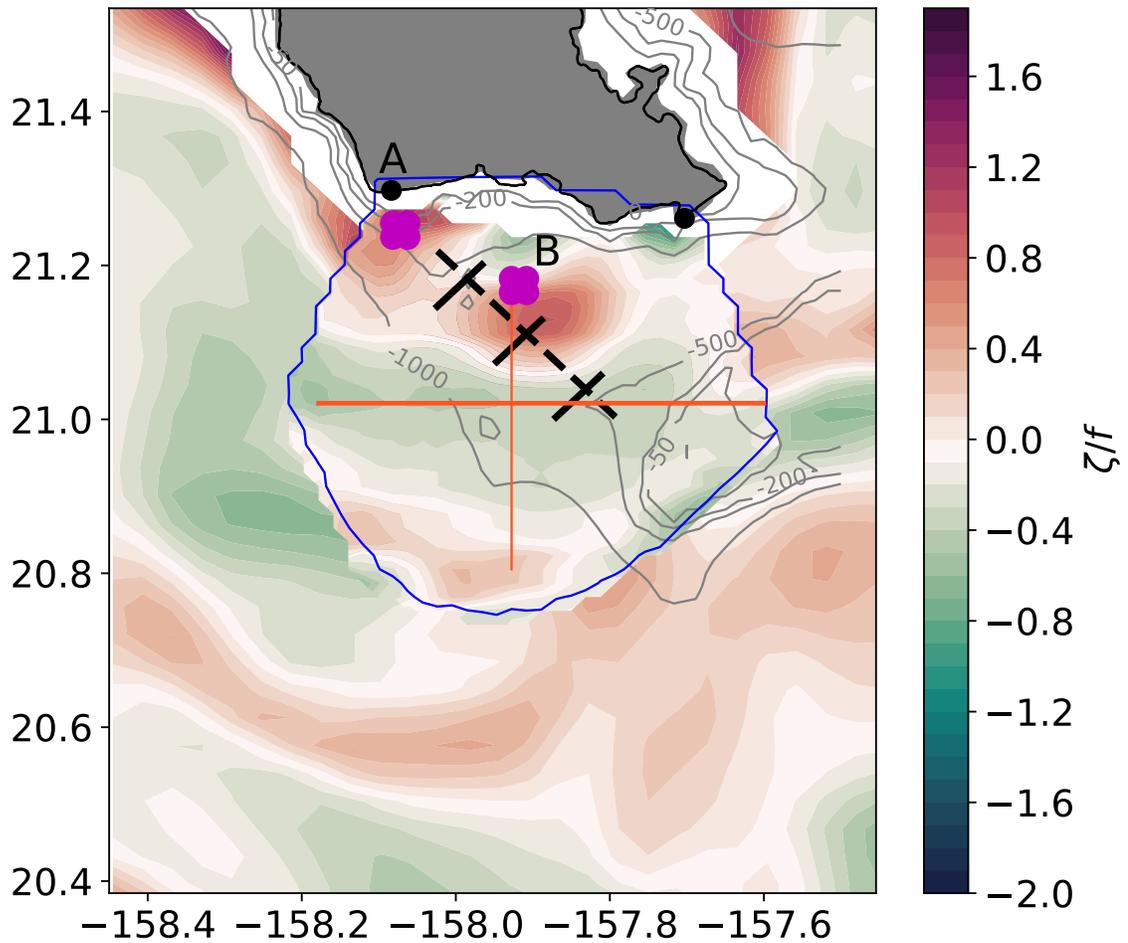
Figure 4.1: Map of instantaneous model (only outside blue line) and observed (inside blue line) surface vorticity south shore of Oahu Hawaii on March 14 2012. The blue line indicates the spatial coverage where 60% of the two-year HFR data is available. Topography is shown by the grey contours for the 50 m, 500 m and 1000 m isobaths. The black dashed thick line indicates the area where barotropic instability occurs. The black solid lines perpendicular to the filament show the locations of the vertical sections plotted in Figure 4.9 and the transect where the EKE budget is computed in Figures 4.12 and 4.13.
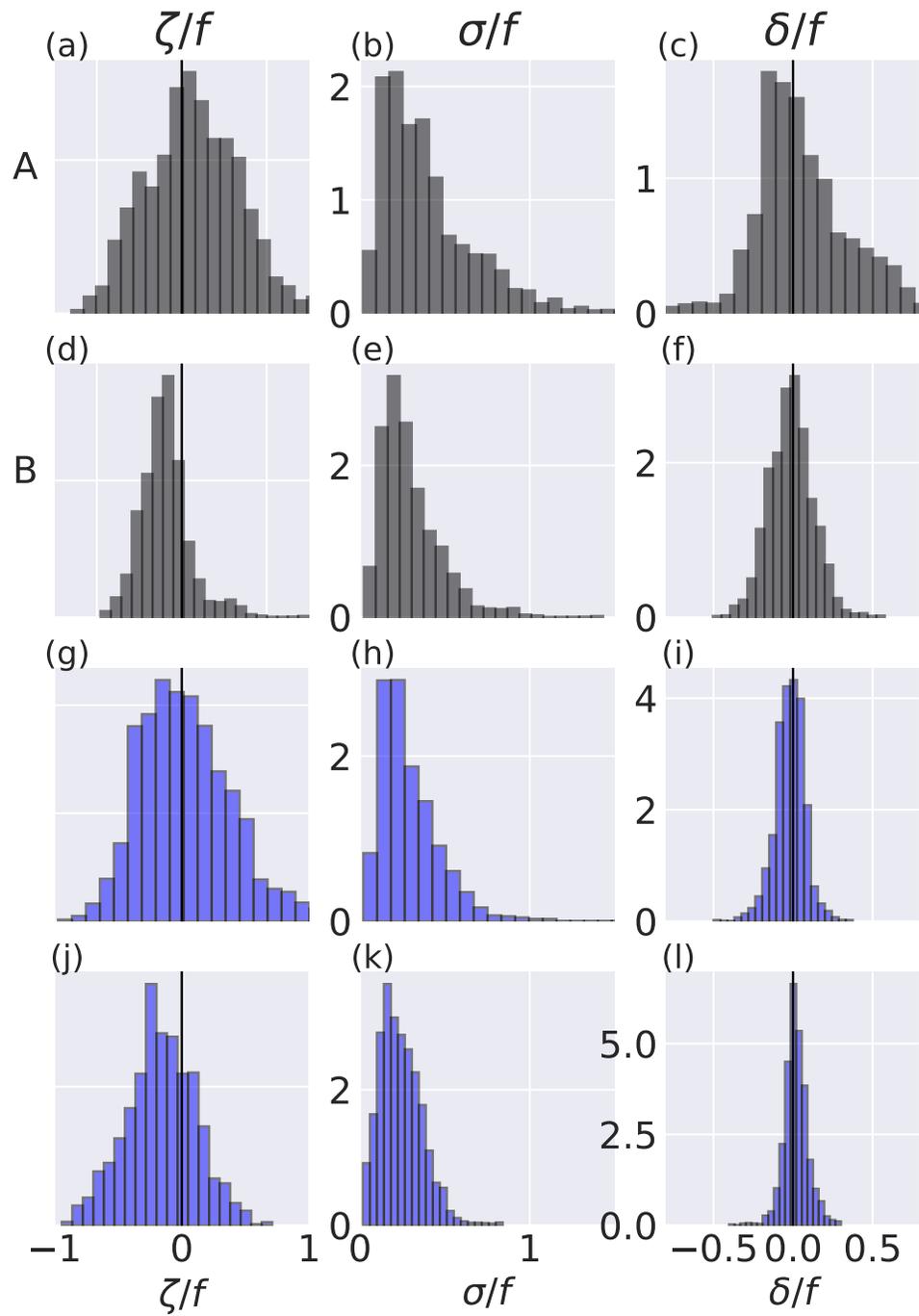
Figure 4.2: Histograms of normalized surface (a)(d)(g)(j) vorticity, (b)(e)(h)(k), strain and (c)(f)(i)(l) divergence using HFRs (top two rows) and ROMS (bottom two rows) surface velocities from regions A and B depicted in Figure 4.1.
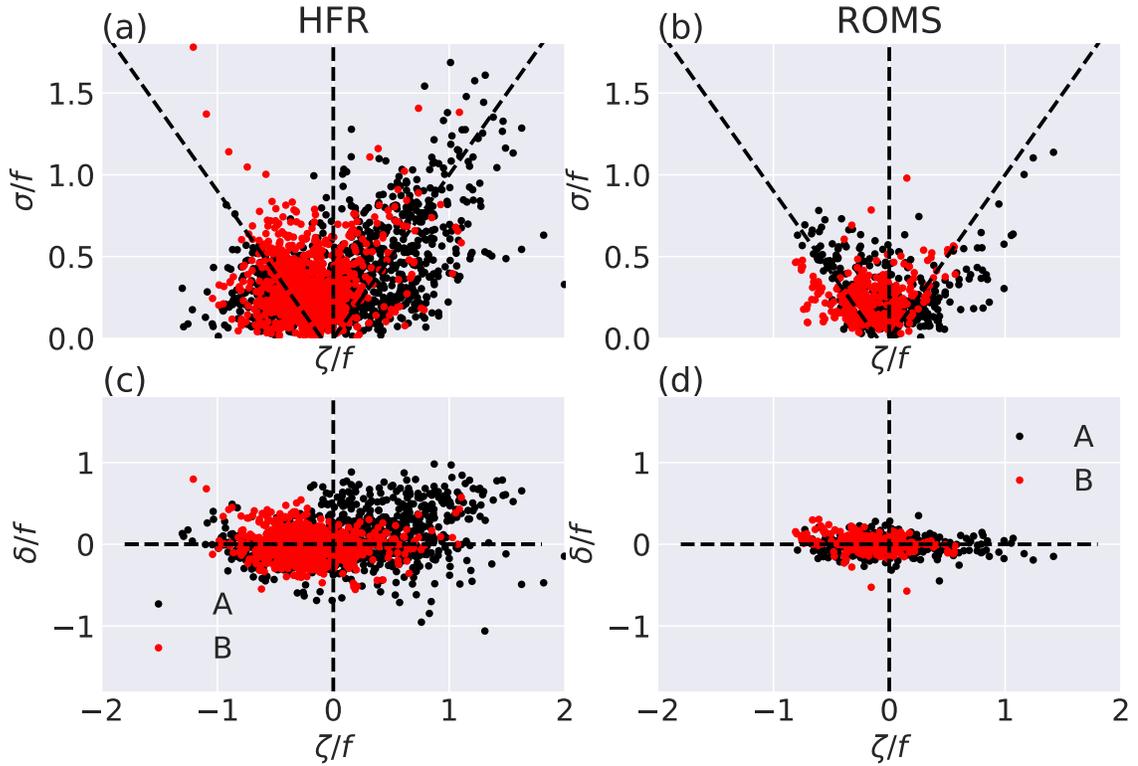
Figure 4.3: Scatter plots of surface (a)-(b) vorticity vs strain and (c)-(d) vorticity vs divergence, from regions A (black dots) and B (red dots) using HFR (left column) and ROMS (right column) surface currents. The black 45° lines in Figures 4.3a and 4.3b correspond to one-dimensional shear flow ($\sigma = |\zeta|$) while values close to the zero strain line $\sigma = 0$ correspond to a solid body rotation flow.
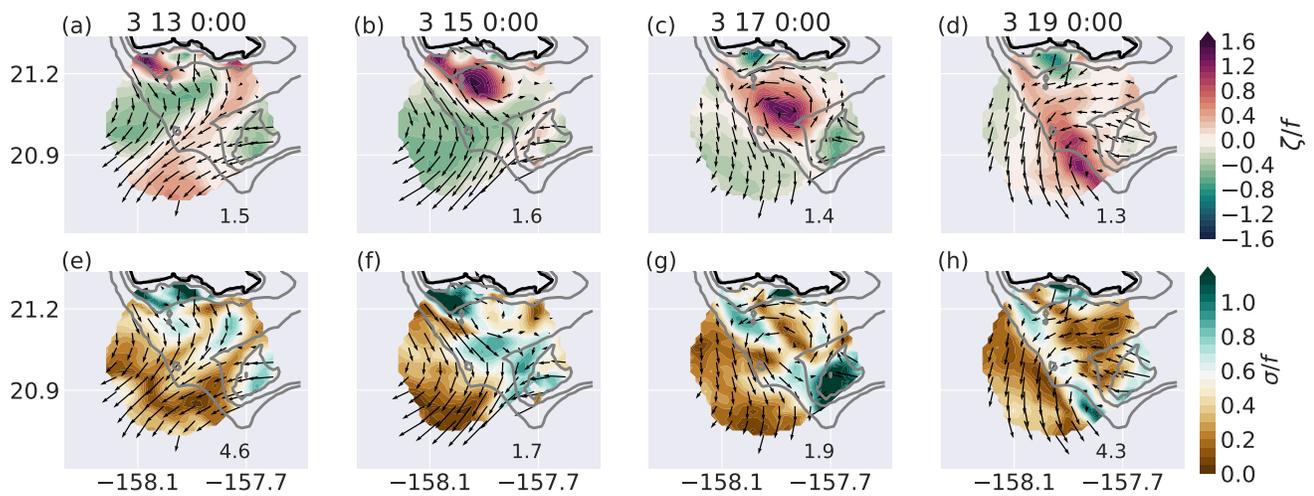
Figure 4.4: Snapshots of surface relative vorticity (a)-(d) and strain (e)-(h) normalized by f. Instantaneous surface velocities are overlaid on each panel. Time interval between panels is 48 hours. Topography is shown in grey contours for the 50 m, 500 m and 1000 m isobaths. Maximum relative vorticity and strain are plotted on each panel. All figures are calculated from the HFR surface velocities.
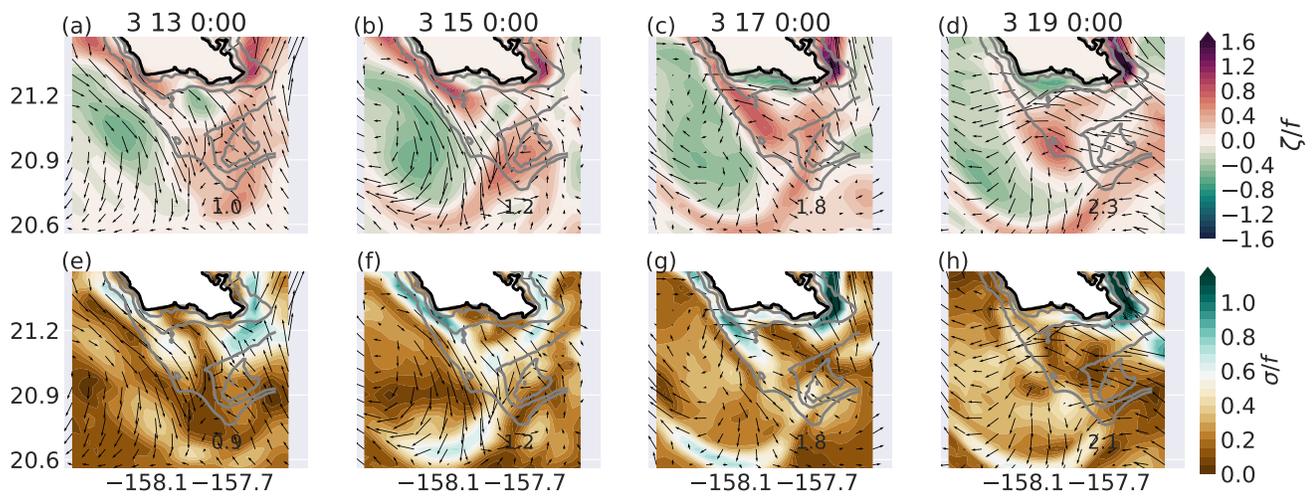
Figure 4.5: As with Figure 4.4 but using ROMS surface velocities.
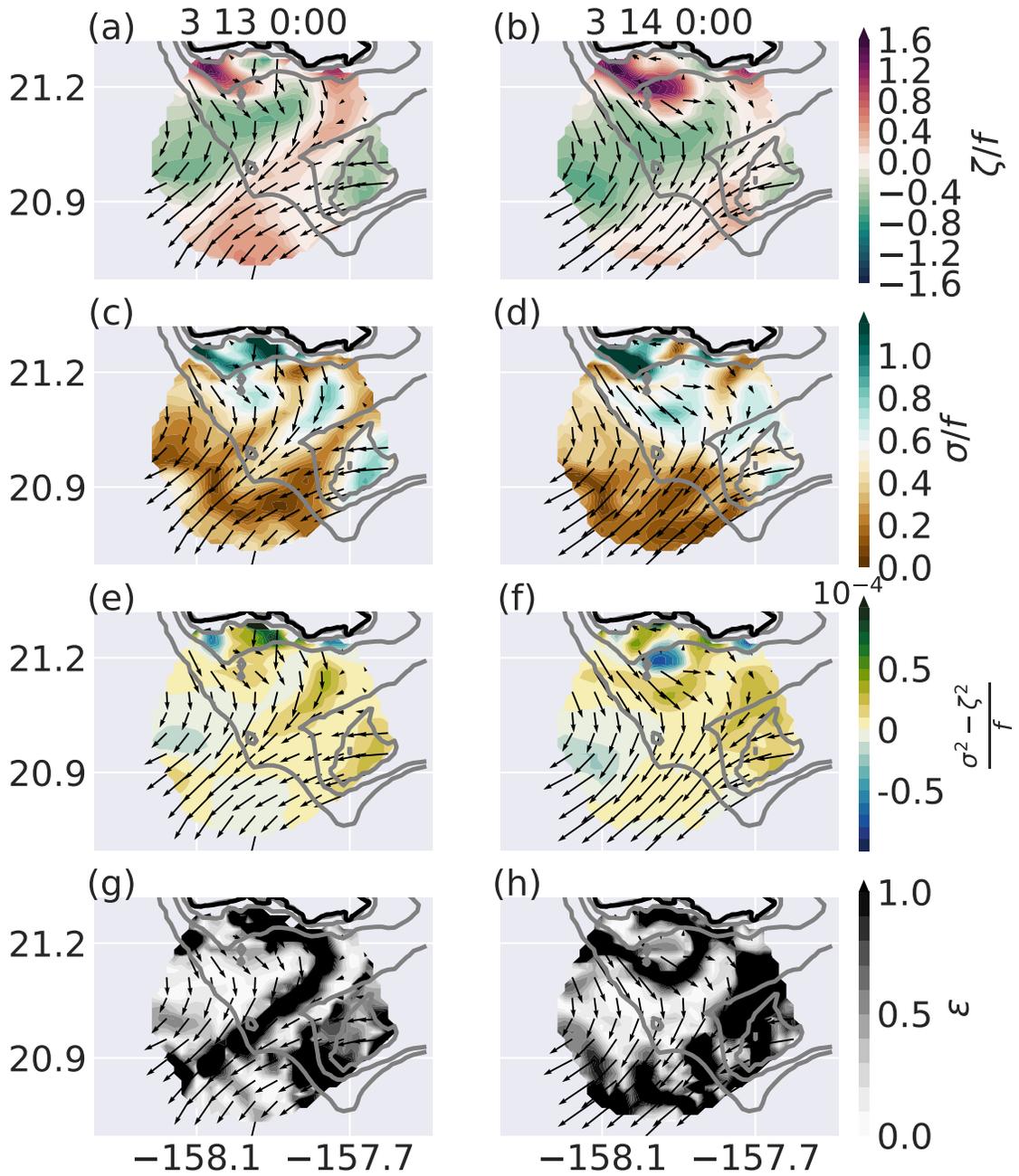
Figure 4.6: Snapshots of surface (a)-(b) relative vorticity, (c)-(d) strain and (e)-(f) the Okubo-Weiss parameter normalized by f. (g)-(h) Parameter of the level of ageostrophy where a value of ϵ 1 indicates the flow is unbalanced. Time interval between each column is 24 hours. The left column panels are computed at the time of filament generation (March 13, 2012) and the right column panels are computed at the time of maximum instability (March 14, 2012). All quantities are calculated using HFR surface velocities.
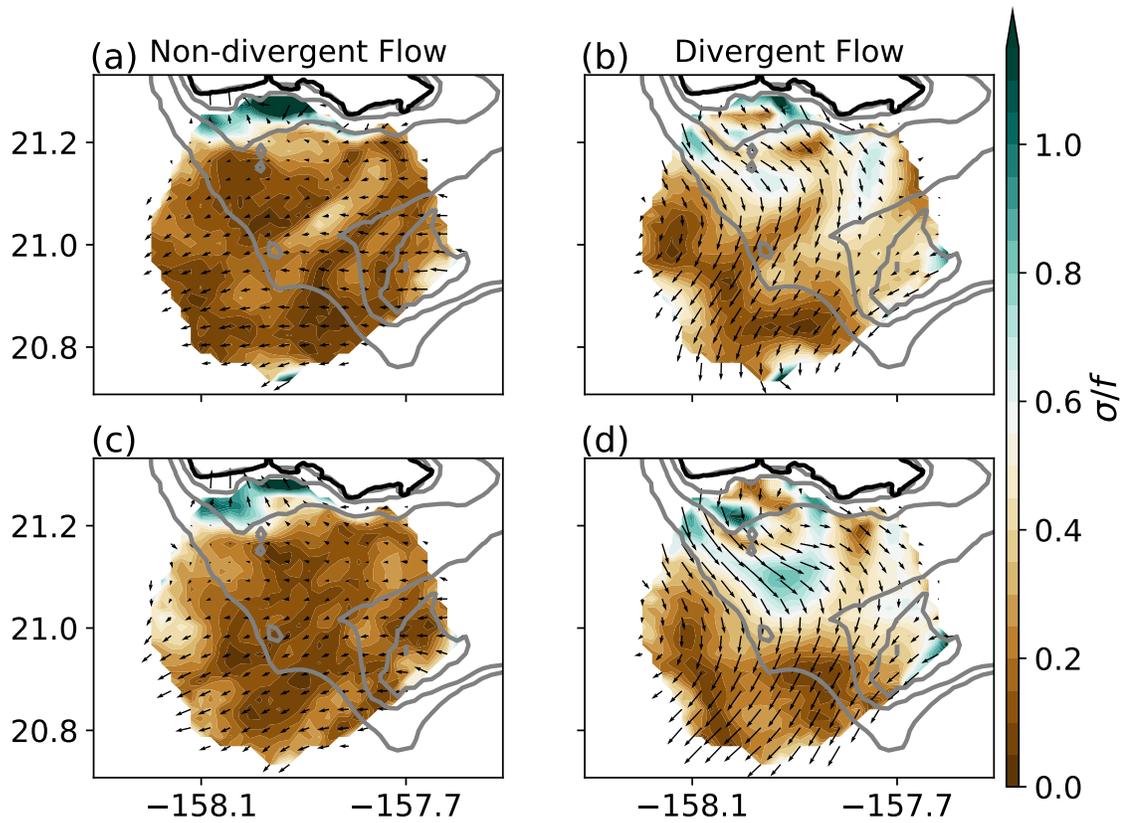
Figure 4.7: Snapshots of strain and surface currents vectors from the HFR flow decomposed into (a)-(c) non-divergent and (b)-(d) divergent components at the time of filament instability. Top row; March 13, 2012 and bottom row; March 14, 2012.
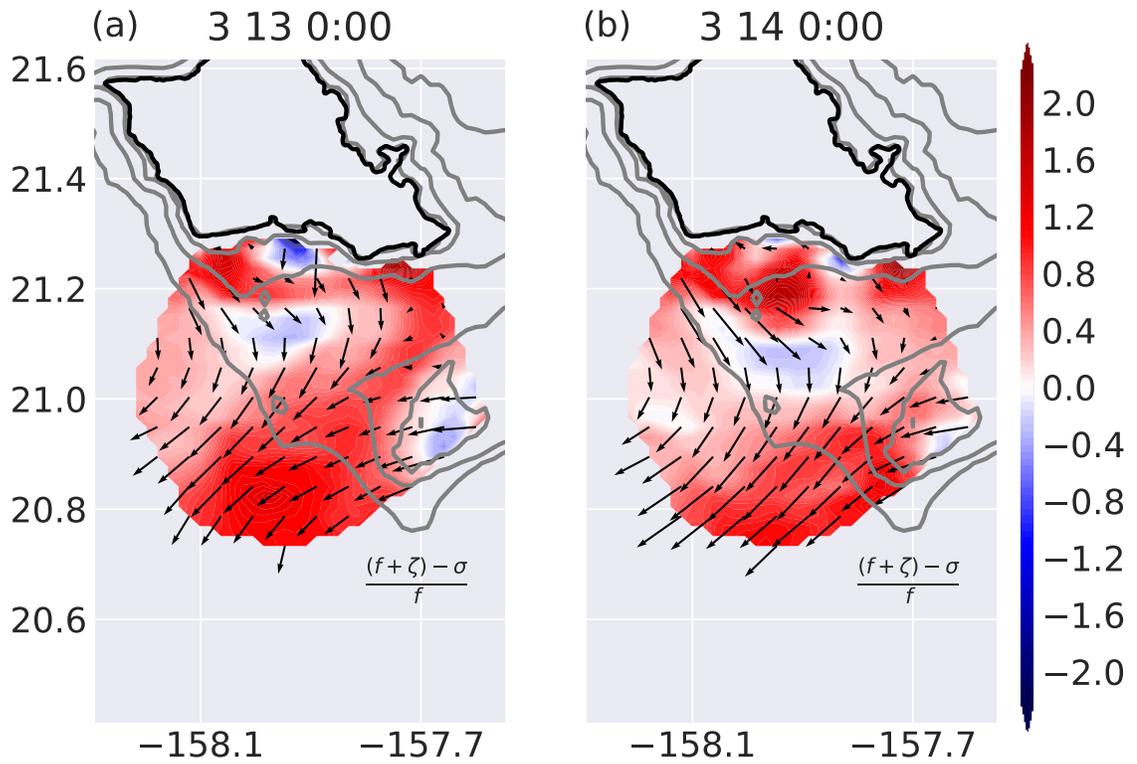
Figure 4.8: Snapshost of $(f + \zeta) - \sigma$ normalized by f at the times of filament maximum instability.
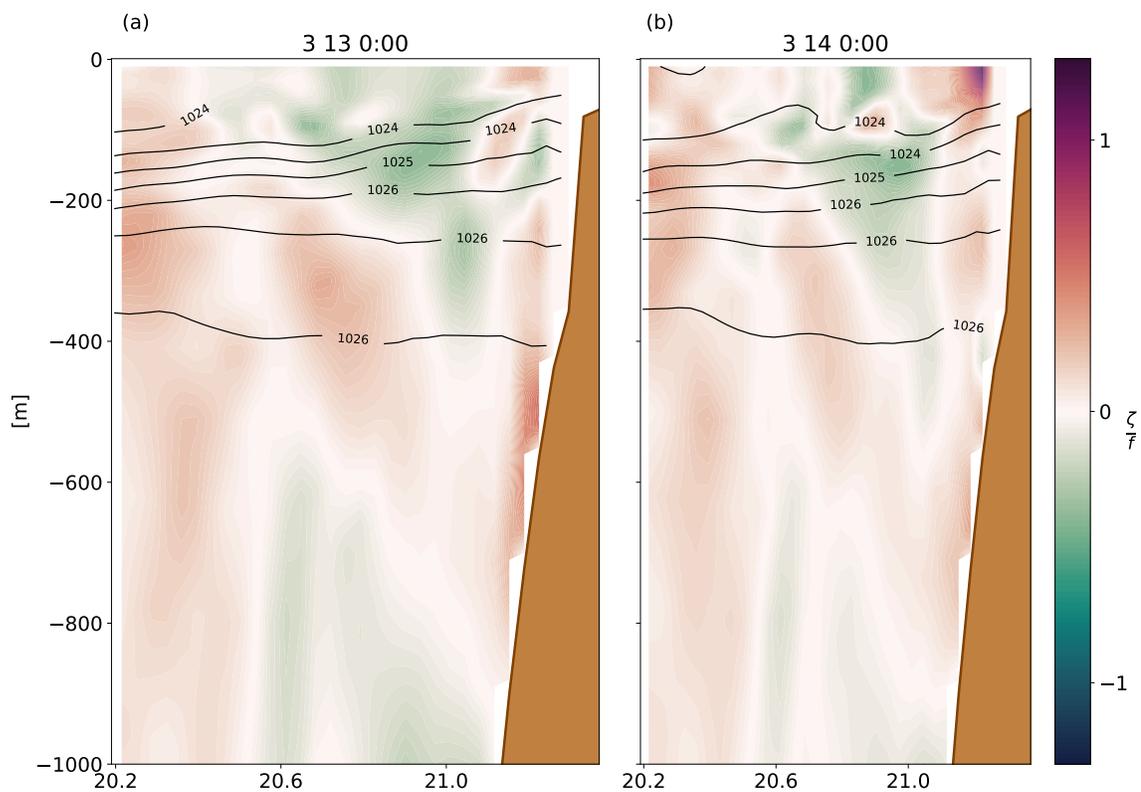
Figure 4.9: Vertical transects of instantaneous relative vorticity normalized by f (shading) at the times shown in Figure 4.6 along the surface transect marked as a black dashed line in Figure 4.1. Density is shown as black contours in kg m^{-3}. Vorticity and density are from the ROMS output.
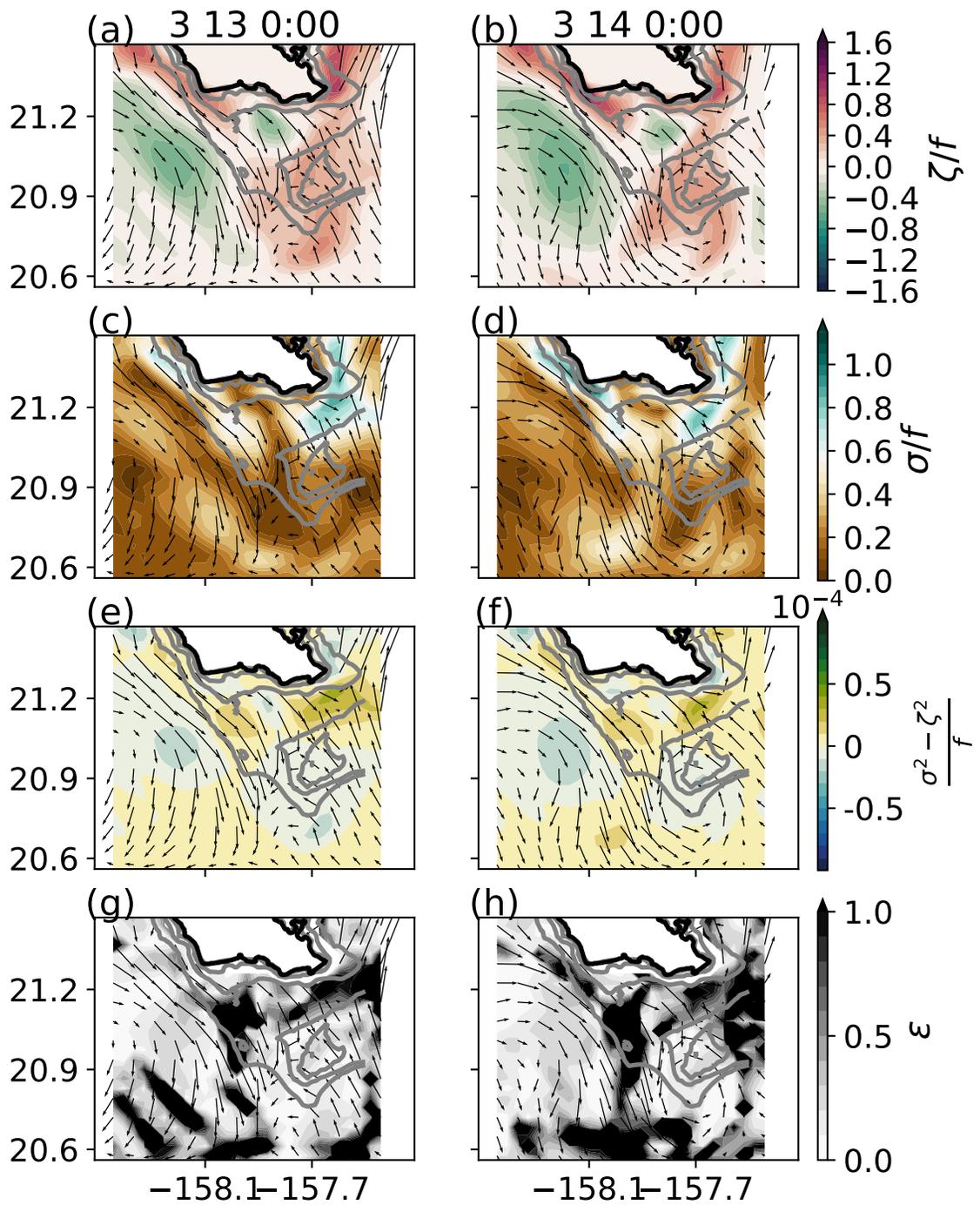
Figure 4.10: As with Figure 4.6 but using ROMS surface velocities.
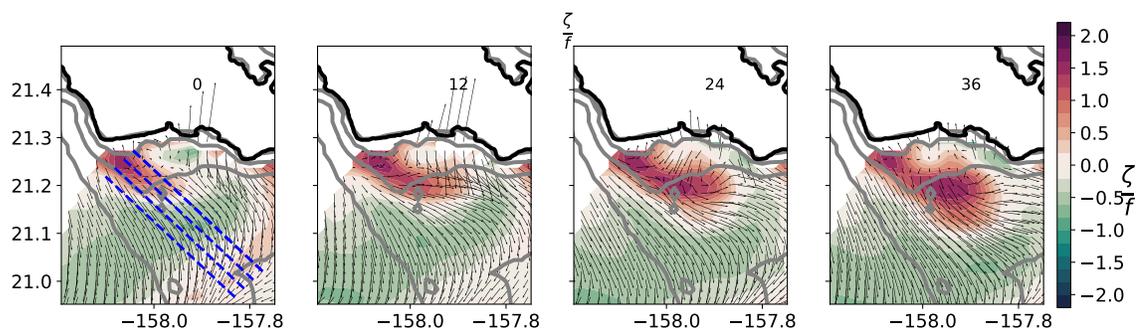
Figure 4.11: Snapshots of surface relative vorticity normalized by f and surface velocities calculated using HFR. Time interval between panels is 12 hours. Topography is shown in grey contours for 50 m, 500 m and 1000 m isobaths. The dashed blue line indicates the grid points where the energy budget is computed in Figures 4.12 and 4.13.
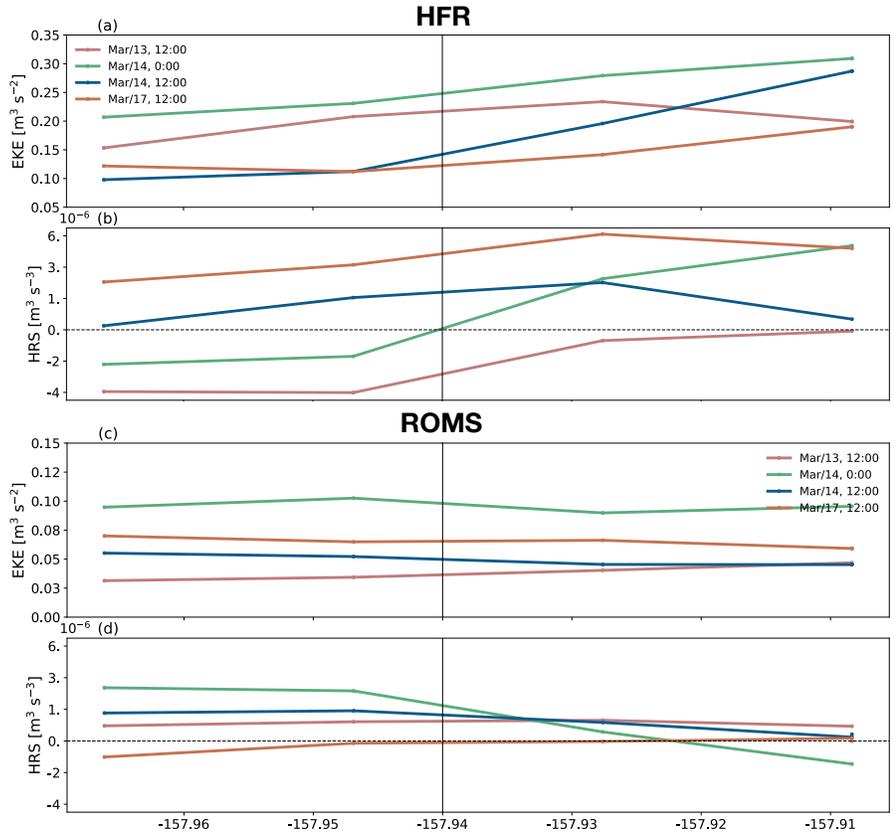
Figure 4.12: Instantaneous surface (a) EKE and (b) the local mean to EKE conversion term due to horizontal shear stress (HRS) integrated in the along-filament direction shown in Figure 4.11. The black solid line on each panel indicates the transect where the vortex detaches from the filament. The energy budget terms are calculated using HFRs (a and b) and ROMS (c and d) surface velocities interpolated into the HFR grid points. Note that, for visualization purposes, there is a different scale on the y axis of each panel.
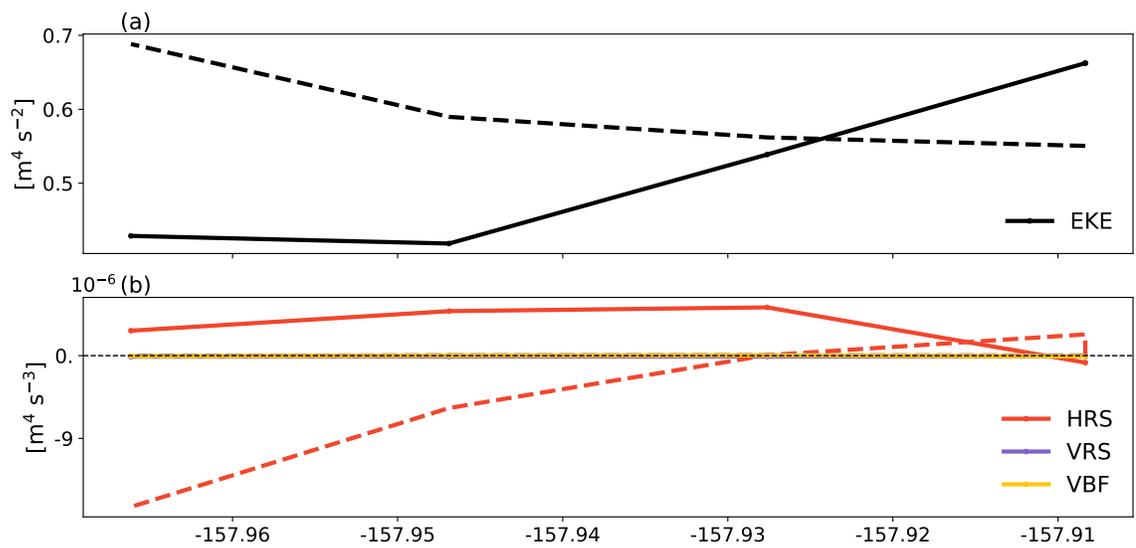
Figure 4.13: Instantaneous (a) EKE and (b) local energy conversion profiles (HRS,VRS and VBF) integrated in the along-filament direction (shown in Figure 4.11) and the upper 100 m using ROMS velocities. The dashed (March 13, 2012) and solid (March 14, 2012) lines indicate times where the instability occurs.
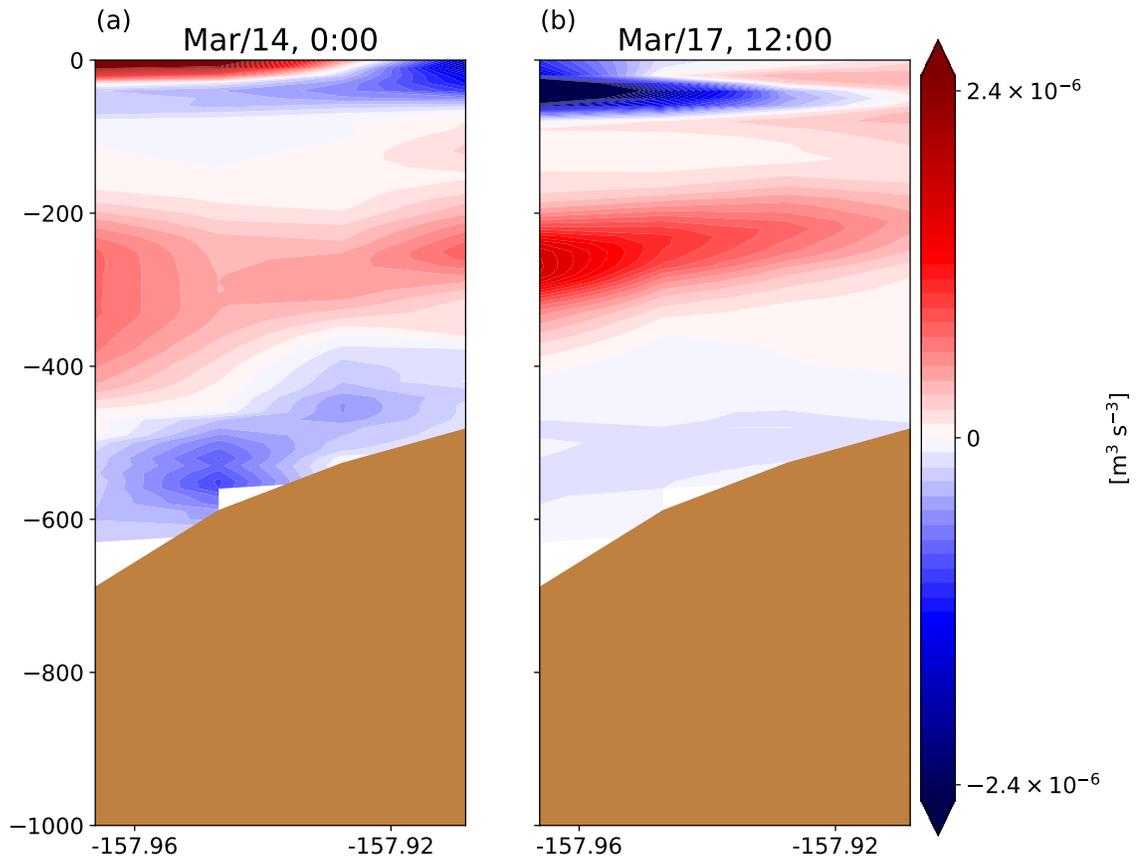
Figure 4.14: Vertical transect of eddy conversions terms (HRS) integrated in the along-filament direction (VBF and VRS are not contributing to the EKE balance therefore they are not plotted) at the moment of (a) maximum instability and (b) when the observed vortex is at its maximum size. Both (a) and (b) are calculated using ROMS velocities.
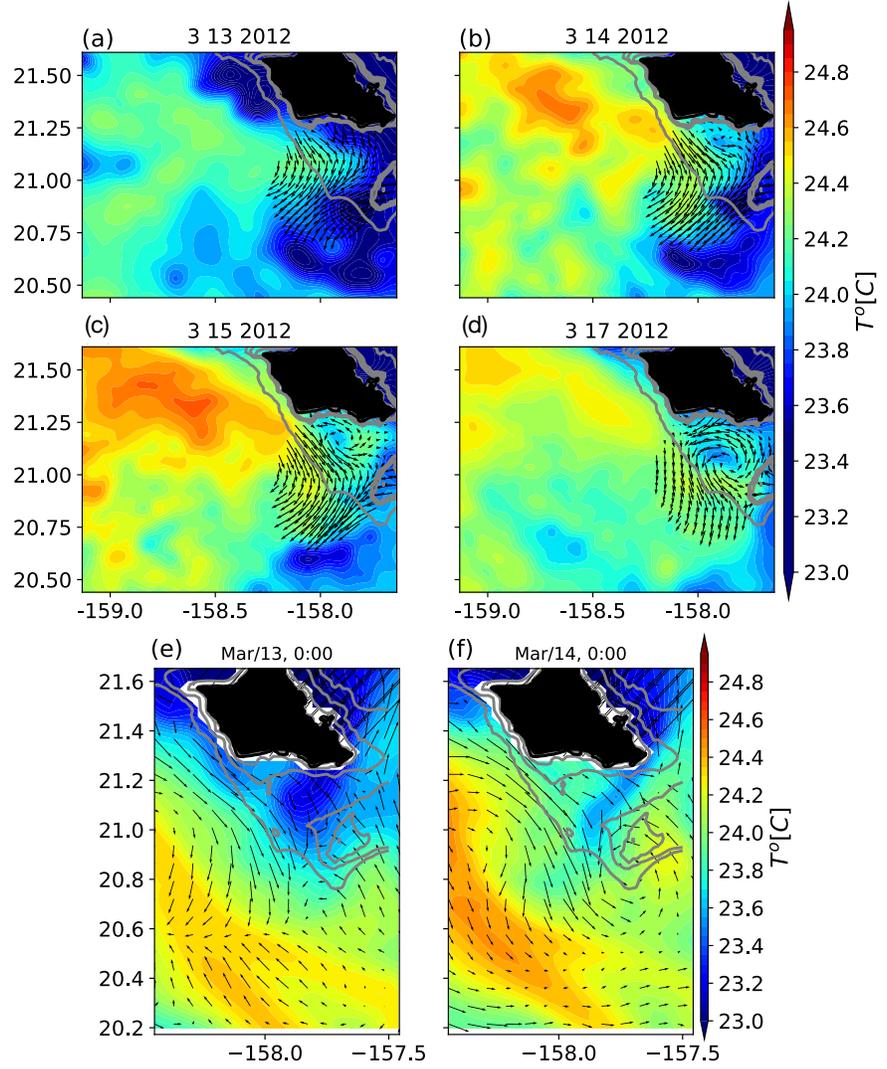
Figure 4.15: Snapshots of instantaneous (a)-(d) daily satellite SST overlaid with daily averaged HFR surface velocities at the moment of vortex formation. (e)(f) Snapshots of ROMS SST and surface velocities at the times shown in Figure 4.15a and 4.15b.
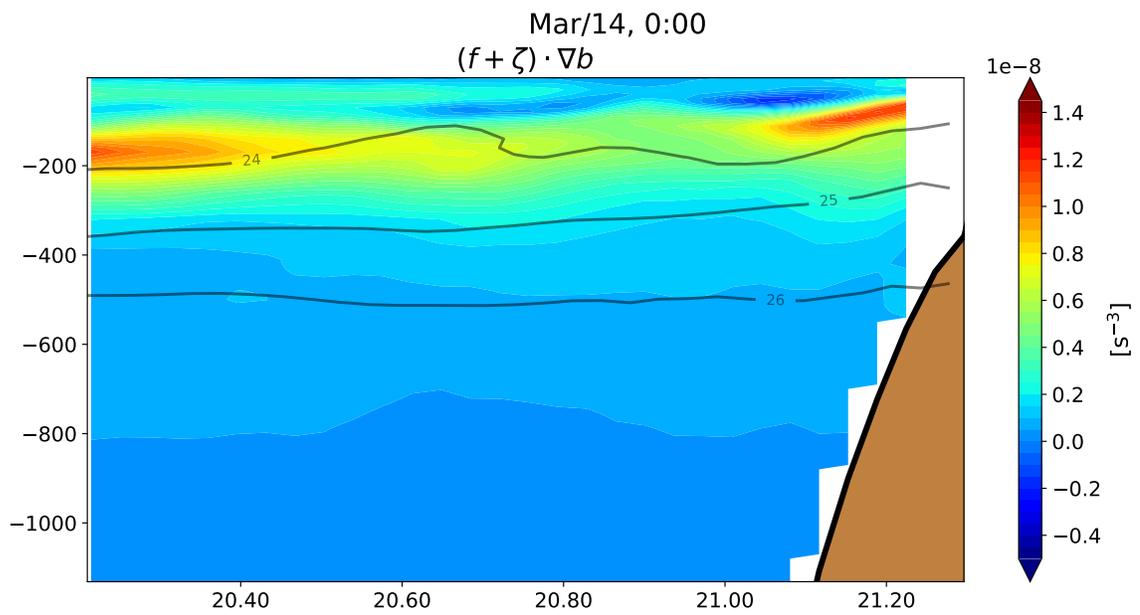
Figure 4.16: Vertical along filament transect (shown in Figure 4.1) of instantaneous potential vorticity $(f + \zeta) \cdot \nabla b$ at the moment of maximum instability. Grey lines indicate the density contours in kg m^{-3} - 1000.
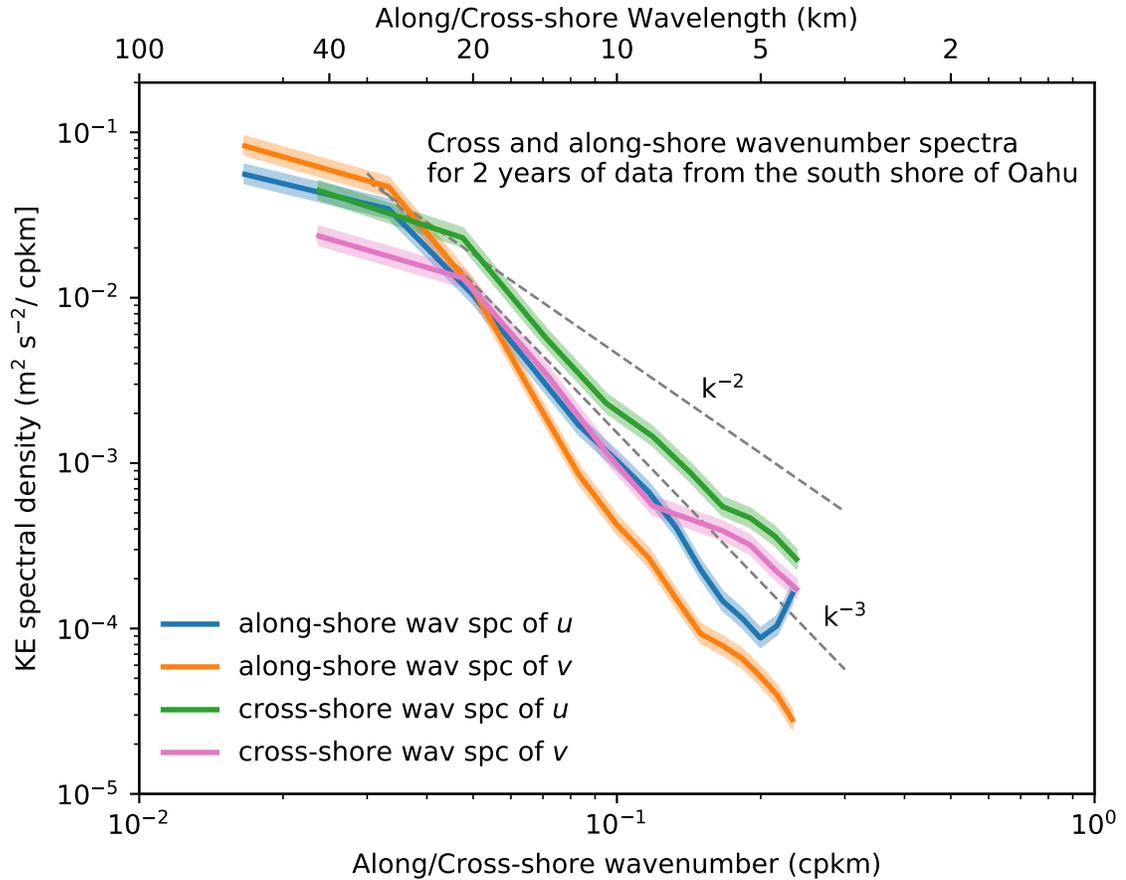
Figure 4.17: KE wavenumber spectra averaged over the two years of available data from September 2010 to September 2012 for the along and cross-shore transects shown in Figure 4.1. Depicted are KE spectra calculated for the along-shore (u and v blue line $\hat{S}_{ua}$ and orange line, $\hat{S}_{va}$) and cross-shore transects (green line, $\hat{S}_{uc}$ and pink line, $\hat{S}_{vc}$) surface currents derived using HFR. For reference k^{-2} and k^{-3} are curves are plotted (dashed black lines). Color shades on each spectra represent the 95% confidence levels.
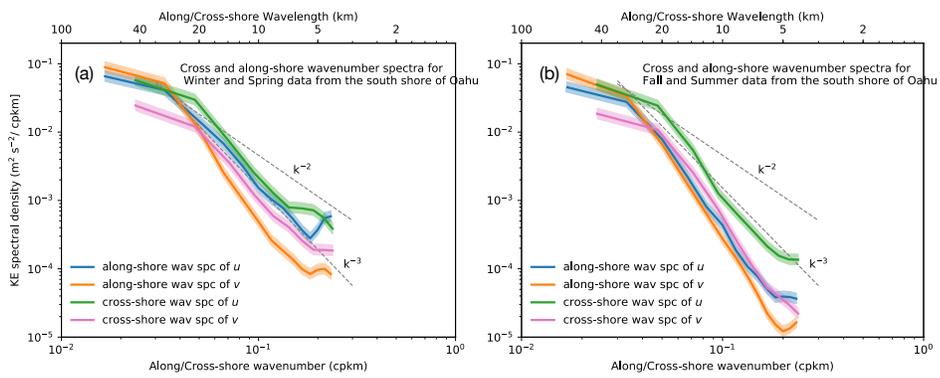
Figure 4.18: As with figure 4.17 but averaged over winter and spring (a) and summer and fall (b) months.

CHAPTER 5
DATA PROCESSING AND VALIDATION

5.1 Data processing

5.1.1 Instrument setting

HFRs map surface currents by detecting slow changes in Bragg-scattered radio wave phase due to changes in ocean conditions. The two HFRs location (KAL 21°18N and KAL 158°5W) are shown in Figure 5.1. An HFR consists of a direct digital synthesizer (DDS) that produces the transmit signal (Tx); a power amplifier (PA) that amplifies the Tx signal; a square array of four Tx antennas to transmit the signal; a linear array of receive (Rx) antennas with filters to demodulate the Rx signals; an analog to digital converter (ADC) to convert the analog Rx signals to digital output and a computer to perform the processing.

The DDS produces a sinusoidal radio wave signal with a frequency of which changes linearly in time following a continuous saw-tooth pattern. The Tx signal is referred to by the center frequency of the chirp (each wave in frequency space). KOK and KAL have a center frequency of 16 MHz. The HFRs are frequency-modulated continuous wave (FMCW) beamforming. The Tx signal is continuously broadcast, and modulated in frequency, hence the name FMCW. One Tx signal is sent to the PA, two signals are sent to the Rx for demodulation of the Rx signals. The Rx receives two Tx signals shifted by 90° to separate the direct Tx signal and ocean modulation.

The PA increases the signal of the Tx received from the DDS while also band pass filtering the Tx signal to remove any contaminating harmonics of the desired signal. The PA boosts the signal to a maximum strength of 52 Watts. The PA then sends the signal to the Tx antenna array. The signal needs to be large since the coaxial cable between Tx and Rx attenuates the signal (i.e 2.6 (0.9) db per 100 m in RGB 213 (1/2" Andrew Heliax Cable)).

The Tx antenna array is arranged in a rectangle to shape the Tx signal pattern. Two

Tx antennas with half of the length of the radio wavelength of spacing between them form a null in the direction of the common axis which in this case is towards land. An extra set of two antennas with the same spacing and a quarter of the length of the radio wavelength distance from the first pair are arranged in a rectangle. This arrangement will allow for a strong signal in the direction of the delayed antennas, in this case towards the ocean. The Tx antennas are designed to be monopoles resonant at the Tx frequency (Figure 5.2a).

The Tx antenna array is located as far as logistically possible from the Rx array in order to reduce the direct-path signal and the direct signal from the Tx. The linear array of Rx antennas is situated parallel to the shoreline in order to allow beamforming. The spacing between the antennas is less than L/2 (where L is the radio wavelength) (Figure 5.2b).

The Tx signal is sent over to the ocean and received by the Rx with the ocean modulation. The Rx signal is received through Bragg scattering of the Tx signal off ocean surface waves. The sea state includes a broad spectrum of waves with various different wavelengths. The radio waves from the Tx array are backscattered off these waves, and are then picked up by the Rx array. The strongest signal will have the most constructive backscatter which is half of the radio wavelength. For the HFRs frequency range, Bragg scattering occurs on ocean waves of wavelength 5-50 m. For the KAL and KOK HFR the Bragg scattering occurs on ocean waves of 9 m since the the EM wave sent from the Tx is of 19 m.

Coastal shadowing and regional noise due to the environmental condition of each specific radar signal may represent additional factors that can alter the performance of the surface current observation. A post processing of the radial and vector currents is therefore necessary to improve the quality of the surface currents.

5.1.2 Radial currents processing

The two HFR used in this work have 16 Rx antennas in a linear array and the beam-forming is performed by adding the antennas signals with the appropriate phase shifts to steer the beam in the desired direction using a Hamming window to reduce the side lobes (Gurgel et al. 1999). The azimuthal resolution depends on the aperture of the receive array, which is

$\frac{2cos(\theta)}{(N-1)}$ for N antennas linearly spaced at half the electromagnetic wavelength and a steering angle θ relative to the normal array. For 16 antennas, it varies from $7°$ for $\theta=0°$ to $15°$ for $\theta=60°$. This angular resolution is not constant with poorer resolution at larger beamforming angles. Sorting a single chirp into range cells via Fourier Transform (FT) resolves the range. This FT is limited in resolution by the sample time of a chirp because it is a discrete FT as $dr = \frac{c}{2B}$ where dr is the range resolution and B is the bandwidth of the Tx chirp. For a given direction and range, the energy spectrum of the echoes contains two peaks due to Bragg scattering of waves advancing to and from the receiver. The radial current is determined from the offset of the peak frequencies from the theoretical Doppler shift for deep water waves (Paduan and Graber 1997). Spectral lines around the peak frequencies, weighted by their signal to noise ratio, are used to compute the average radial current and its standard deviation as a measure of accuracy. Radial currents with standard deviation larger than 4 cm s^{-1} and with less than 60% of the total time coverage were removed.

Figure 5.3b and 3d show the standard deviation of radial currents for KAL and KOK as a function of the steering angle shown in Figure 5.3a and 5.3c. In the transect near to the HFR sites (transect A) standard deviation is smaller than 20 cm s^{-1} while away from the HFR sites (transect C) the standard deviation reached up to 35 cm s^{-1}. KAL has more variability than KOK, this can be seen in the standard deviation at the A and B transects where KOK standard deviation varies as a function of the angle. Furthermore the lowest standard deviation is found at the edges of the KOK spatial domain ($160°$ and $285°$). In KAL, this modulation is not observed in the A and B transects since the standard deviation is lowest at $120°$ and maximum at $160°$. As expected, a larger standard deviation in both KAL and KOK are observed in the farther transect from the coast (C) due to the beamforming of the HFR.

Each HFR is an independent instrument, the quality of the radial currents can be assessed by the correlation between radial currents from both sides which should approach -1 along the baseline joining the two HFR sites and +1 far offshore were the radials are almost collinear. If along-baseline and across-baseline current components were uncorrelated

with equal variance, the correlation pattern should follow that of the cosine of the angle between radials from the two sites (Chavanne et al. 2007; Castillo-Trujillo 2014). The differences between the cosine function and the real correlation are likely due to the violation of assumptions and to measurement errors which should increase toward the edges of the azimuthal sectors. Correlations and RMSD between KOK and KAL radial currents for overlapped space and time periods are shown on Figure 5.4. An anti correlation of -1 is observed close to the shore while a correlation of 1 is found away from the sites. The largest anticorrelation and RMSD are found close to the KOK site while the largest positive correlation and lowest RMSD are observed at 157.50°W and 20.80°N. Larger than 50 cm s^{-1} RMSD are observed at the edge of the azimuthal sector at 158.25°W, this is likely due to a hardware error in KAL.

5.1.3 Vector currents processing

The non-orthogonally and irregularly sampled radial velocities contain sufficient information to reconstruct vector currents with more than 2 HFRs (Soh et al. 2018). Vector currents were estimated on a 2 km Cartesian grid by least square fitting the zonal and meridional component to all radial measurements from the two sites within a 2 km search radius (Lipa and Barrick 1983). The shorter search radius results in a better estimation of the real vector currents (Soh et al. 2018). The normal component is poorly constrained near the baseline (close to the coast) between the two sites and the azimuthal component is poorly constrained away from the sites yielding a Geometric Dilution of Precision (Chavanne et al. 2007). (Soh et al. 2018) found out that the degree of distribution of the radial velocities does not affect the GDOP of the estimated vector currents and the least square fit estimation only depends on the number of radial velocities used in the fit. They also found that regardless of the vector current estimation method (least square fit versus optimal interpolation) the standard deviation of the misfits between the estimates and true values of known surface currents ranges from 2 to 10 cm s^{-1}.

Because the least square fit assumes an infinite SNR, the mapping error is assumed be

very small or zero and the GDOP is considered as the uncertainty of the vector currents. The uncertainty of the vector currents can propagate through the final outcomes (Soh et al. 2018) and can be incorporated as a random variable in the processing. For this work, vector currents where GDOP is greater than 1.5 were removed after the least square fit was performed. GDOP ellipses and HFR vector current variance ellipses over the two year time period are shown on Figure 5.5a and 5.5b. The HFR variance mimics the GDOP noise with largest ellipses close to the shore (meridional component) and away (zonal component) from the HFR sites.

Hourly mean surface velocities were made from the evenly spaced 15 minute vector time series. A second processing was made were surface current amplitudes larger than —2— m s^{-1} and and with less than 60% of the time coverage were also removed from the hourly vector current time series.

5.1.4   Temporal and Spatial Coverage

The maximum range of good measurements depends on the signal propagation conditions and on the ambient electromagnetic noise. During the two years of overlapped data between KAL and KOK, the maximum day and night ranges of 50% data return were 55 km for KOK and 65 for KAL (Figure 5.6 and 5.7). The D layer of the ionosphere is more dissipative and inhibits the propagation of distant electromagnetic signals in daytime but disappears at night, leaving the more reflective E layer to propagate distant electromagnetic noise. This diurnal modulation was not observed in the data coverage. Temporal coverage of the HFR total spatial coverage where Kol and KAL radial currents overlap is shown on Figure 5.6a and 5.7a. Throughout the two year period KAL had a spatial coverage of around 60% of the total coverage observed in Figure 5.1 while KOK of 50% of the total coverage shown in Figure 5.1.

5.2 HFRs validations

5.2.1 Comparison with gliders

Surface currents from gliders designed at the University of Washington (Eriksen et al. 2001) with 1.8 m long and 52 kg of weight are used to compare their surface velocities to the HFRs. The Seaglider motion is controlled by i) pumping oil between the pressure case and an external bladder therefore changing the glider's volume and hence the buoyancy, ii) moving the battery along the glider axis to change pitch and iii) pivoting the battery asymmetrically to turn the glider (roll). Seagliders are programmed to navigate in a sawtooth pattern at about half a knot and have a maximum diving pressure of 1000 m. Seagliders can measure temperature, conductivity, fluorescence, sound or velocity shear, chlorophyll, salinity and surface and depth averaged currents. The Seaglider repeats the same following steps until it is recovered:

- At the surface the Seaglider downloads any new instructions including way points using the Iridium network.

- A GPS position is taken.

- Based on estimated currents, the Seaglider calculates the best heading and dive slope to make progress towards the target way point.

- The Seaglider begins the dive cycle by decreasing its volume and adjusting the battery position to achieve the required glide slope. Since sometimes the Seaglider is pushed by currents, at intervals it checks its heading and target and makes corrections as needed.

- At the target depth, the glider pumps oil in the external bladder and adjusts the battery position to be nose up. Two Seagliders are used to compare the currents; the PacIOOS Seaglider which reached depths of 450 m and the ALOHA Seaglider which reached depths of 800 m.

- On reaching the surface, the glider orientates itself to have the antenna pointing skyward, where a GPS position is taken before sending and receiving data via satellite. Typical dives last 3 hours and 4.5 hours for the PacIOSS and ALOHA Seagliders respectively.

The difference between the two GPS positions, before and after the data transfer, gives an estimate of the surface current and the difference between the actual surfacing location and one predicted by a flight model algorithm gives an estimate of the depth-averaged current. Eriksen et al. (2001) found errors in horizontal speeds of around 1-1.5 cm s^{-1}. The Seagliders trajectories were chosen to compare real time assimilation in the ROMS described in this work. The route off the south shore of Oahu was chosen to avoid Penguin Bank and main shipping lanes (Figure 5.1). From the twelve missions conducted from 2008 to 2011, 4 missions overlapped with the HFR temporal coverage (Figure 5.8). The surface currents from these missions are compared to the HFR radial and vector surface current components.

Scatter plots of HFR radials for KAL and KOK and Seagliders currents projected into the HFR radial components at the HFR grid points closest to the Seagliders velocities are shown on Figure 5.9. Correlations range from 0.79 to 0.90 (significant at 95% confidence level) and root mean square differences (RMSD) between 9 cm s^{-1} and 13 cm s^{-1} when radial velocities are compared. In contrast, the correlation is not significant when Seagliders and HFRs vector currents are correlated, while the RMSD increased to $\sim$25 $^{-1}$.

5.2.2 Comparison with ROMS

Radial components

The ROMS surface currents interpolated into the HFR spatial grid are projected into the Kak and Kol radials. RMSD between model and observed radial currents for both HFRs are shown in Figure 5.10. In general, RMSD were larger close to the coast and away from the HFR sites. When the ROMS projected currents are compared to KOK, larger than 20 cm s^{-1} RMSDs are observed close to the KOK site, this is also the case when model

currents are compared to the KAL site (larger RMSD close to the KAL site). The RMSD between model radial currents projected into KAL and KAL radials were overall lower than when the model radials was compared to KOK radials. The spectra of model radials versus radials from KAL and KOK at the grid point with the lowest RMSD between model and observations is shown on Figure 5.11. There is a better agreement between model and KAL radial currents, specially for frequencies higher than f.

Vector components

The 2 year time-averaged surface current magnitude of the HFRs and ROMS vector surface currents is shown on Figure 5.12. Larger amplitudes are found away from the coast in both model and observations. The largest discrepancies as expected are observed close to the shore and away from the HFR sites due to the GDOP. In general, the magnitude increases in areas deeper than the 1000 m isobath with average amplitudes of $\sim$30 cm s^{-1}. The standard deviation of the surface vector currents is shown on Figure 5.13. Due to the GDOP, amplitudes greater than 20 cm s^{-1} are found close to the shore in the meridional component and away from the coast in the zonal component. The smallest amplitudes are found in both the zonal and meridional components close to the KAL and KOK sites and in the Kaiwi channel. The standard deviation of the model zonal and meridional components increased away from the coast in both components with the zonal component having the largest surface currents at $\sim$20 cm s^{-1} in areas deeper than 1000 m isobath. The meridional component is less variable than the zonal component due to the HLC (Castillo-Trujillo 2014) and has the largest amplitudes at around 12 cm s $^{-1}$. This is also observed in the standard deviation of the HFR surface velocities. ROMS and HFR time series of 3 day low pass zonal surface currents at regions A and B (shown in Figure 5.1, Chapter 2) are shown in Figure 5.14. There is a good correspondence in both regions, RMSD are shown in Table 1.

Spectra of ROMS and HFR averaged surface vector and radial currents are shown on Figures 5.15. The largest discrepancy is found in the near inertial band where the model near-inertial clockwise variance is ten times larger than the observations due to the

assimilation process (more details on Chapter 3). The vorticity and divergence spectra are similar with more vorticity variance close to the inertial band in the model data.

Table 5.1: RMSD between model and observed zonal and meridional surface velocities from averaged regions A and B shown in Figure 5.1 Units are in m s^{-1}. Subscripts raw and low indicate the 3-day low pass and every 3 hours surface velocities.

REGION	u_{raw}	u_{low}	v_{raw}	v_{low}
A	0.17	0.05	0.16	0.04
B	0.17	0.02	0.15	0.01
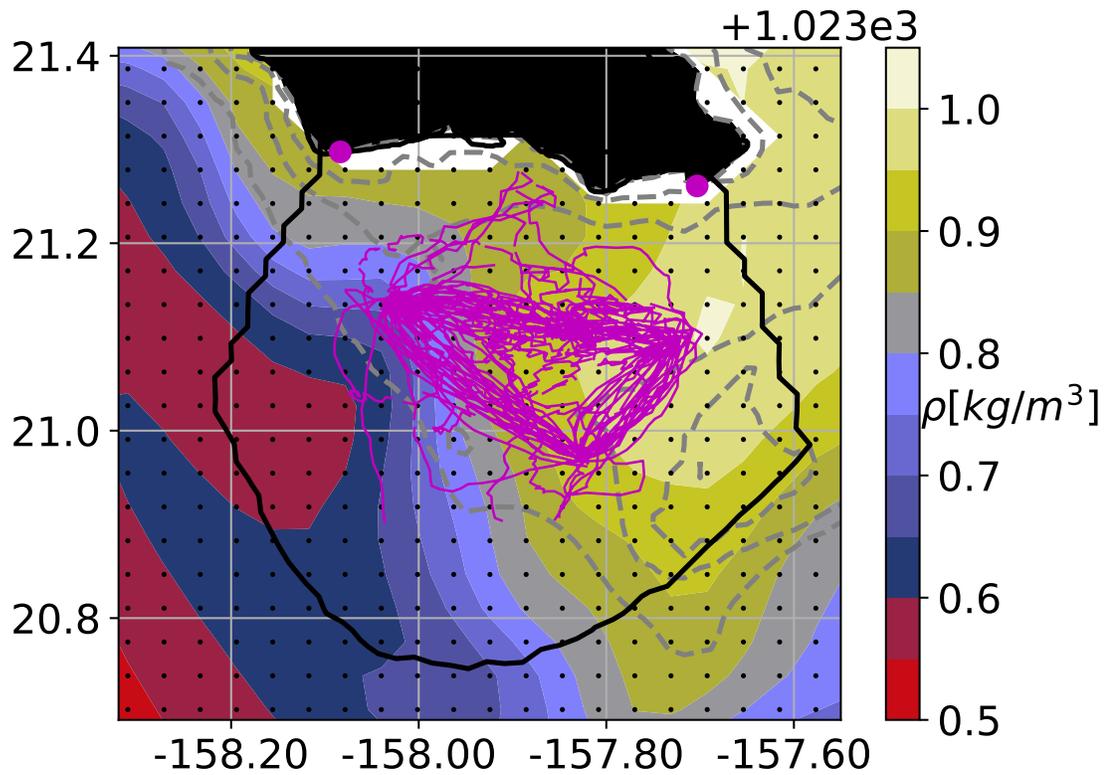
Figure 5.1: Snapshot of density on March 14 00:00 using ROMS surface temperature and salinity. The black solid line indicates the area where 60% of the total two-year data is available. Magenta dots indicate the two HFR locations KAL and KOK. The magenta solid thin lines indicate the gliders transects.

(a) OCEAN
LAND
TX SIGNAL
ANTENNA
ANTENNA
L/2
NULL
L/4
L/4
NULL
L/2
ANTENNA
ANTENNA
NULL
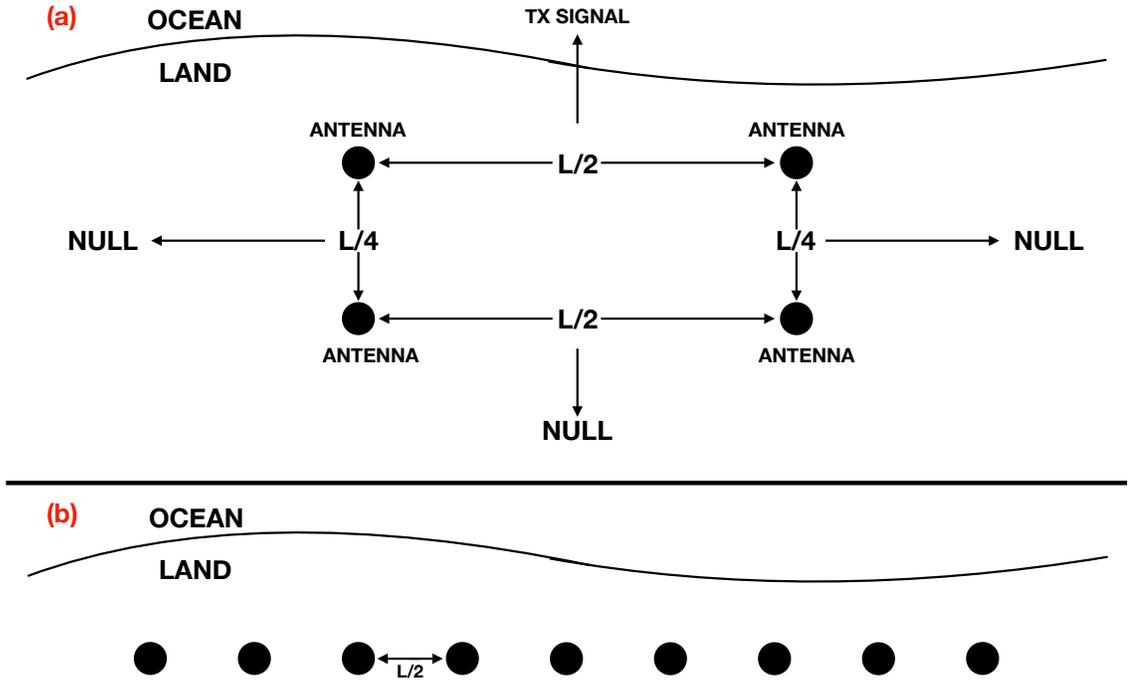
(b) OCEAN
LAND
L/2

Figure 5.2: (a) Transmit antenna array showing distances between antennas, cable delays, and orientation with respect to the ocean to create three directional-nulls and amplify the signal over the ocean. (b) Receive antennas array for HFRs with spacing less than half the radio wavelength (L). Array is oriented parallel to coastline.

128
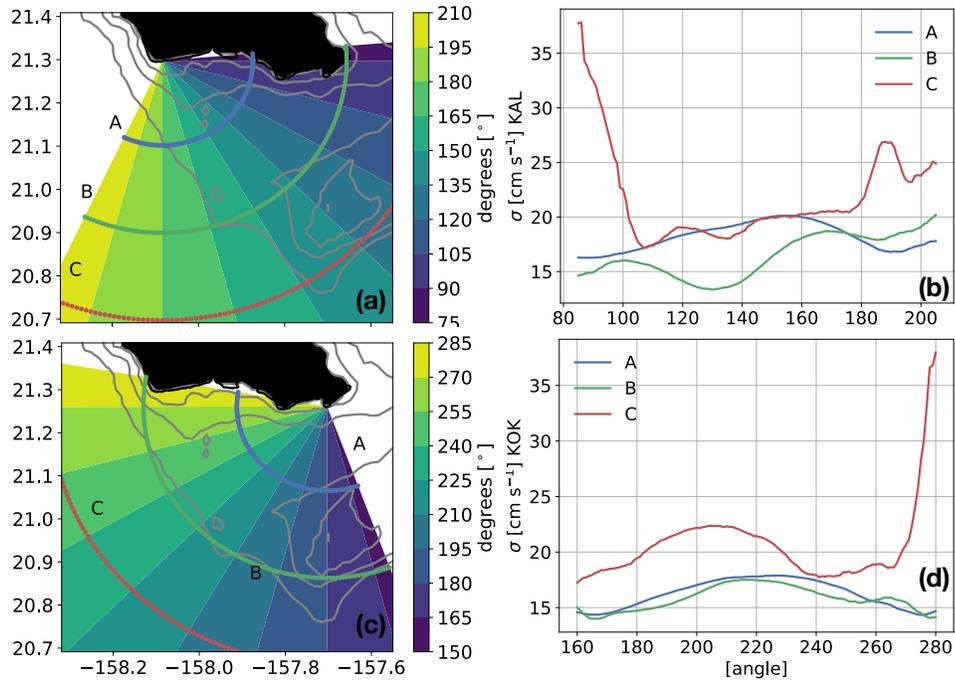
Figure 5.3: Azimuthal angle (colors) for (a) KAL and (c) KOK in degrees. Standard deviation during the period shown in Figures 5.6 and 5.7 as a function of the azimuthal angle over the transects shown in (a) and (c) for (b) KAL and (d) KOK.
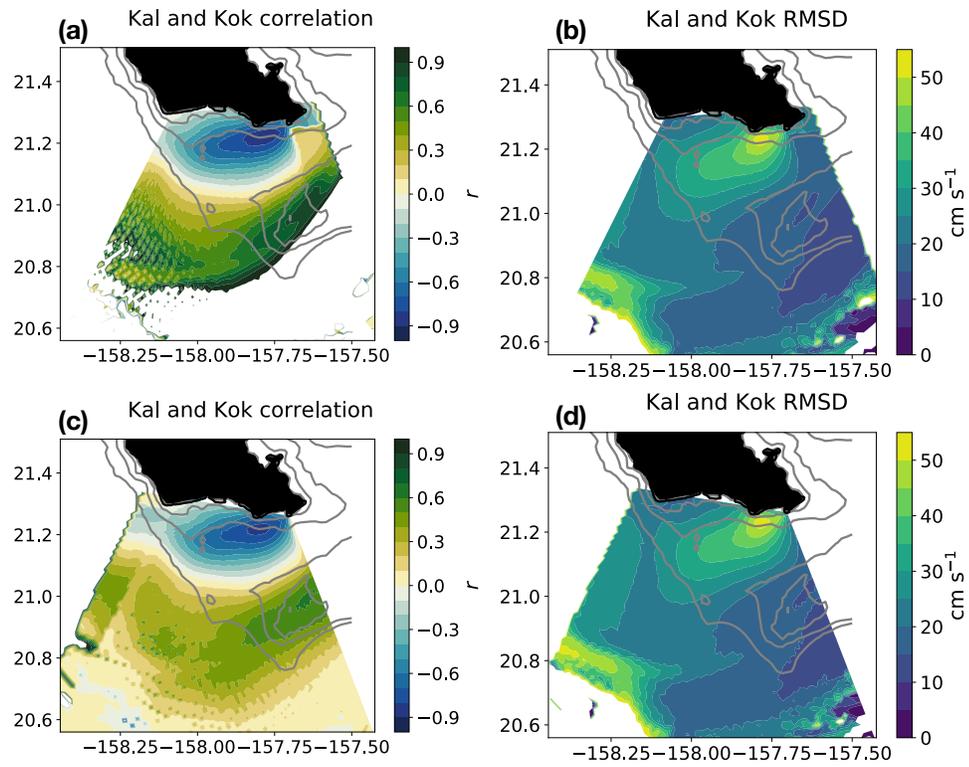
Figure 5.4: KAL and KOK radial currents (a) and (c) correlation and RMSD (b) and (d) during the periods when KAL and KOK data is simultaneously available over the spatial areas where both HFRs coverage overlap.
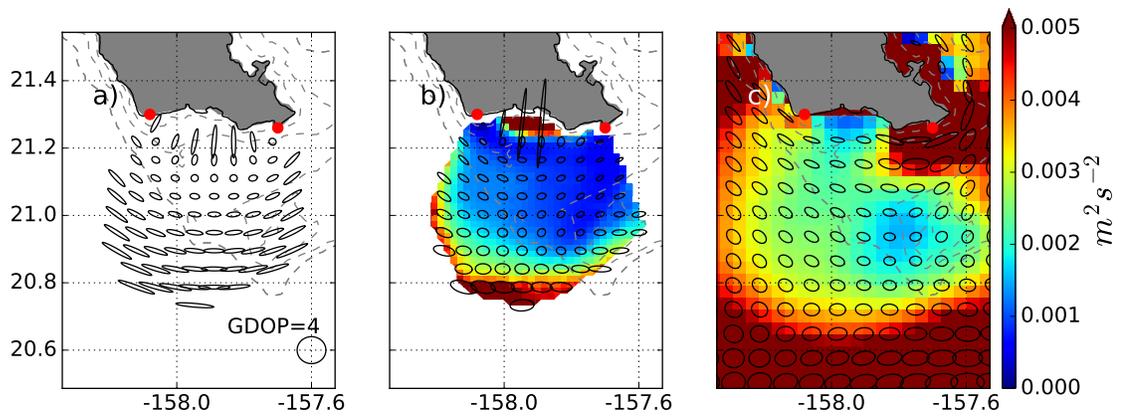
Figure 5.5: (a) GDOP estimated from the KAL and KOK locations. Kinetic Energy color maps overlaid over surface current variance ellipses from (b) HFR and (c) ROMS surface currents. Red dots indicate the KAL and KOK location. A GDOP of 4 is shown in (a) as a reference.
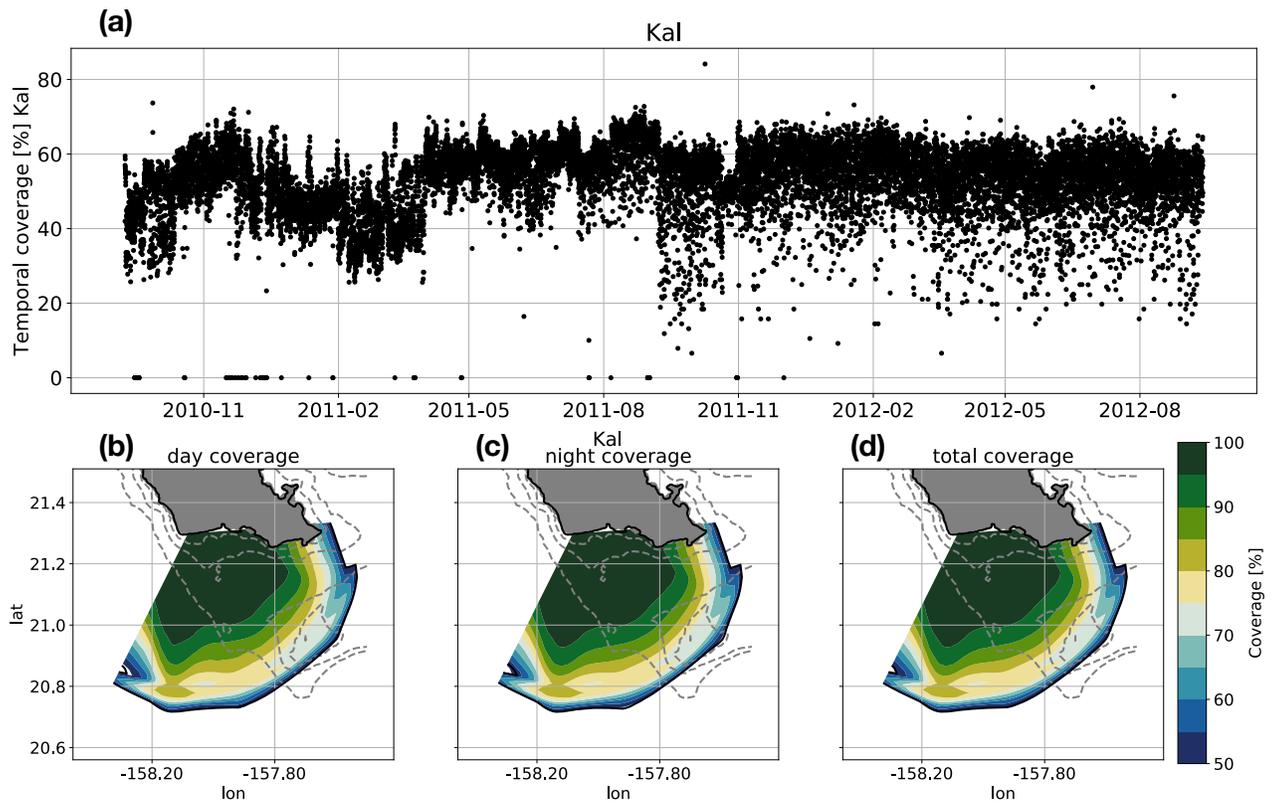
Figure 5.6: KAL (a) time series of the percentage of spatial coverage of the area shown in (b) for the period of data available from November 2010 to August 2012. Colormaps of (b) daily (6:00 to 16:00) (c) nightly (16:00 to 6:00) and (d) total percentage of available data from November 2010 to August 2012.
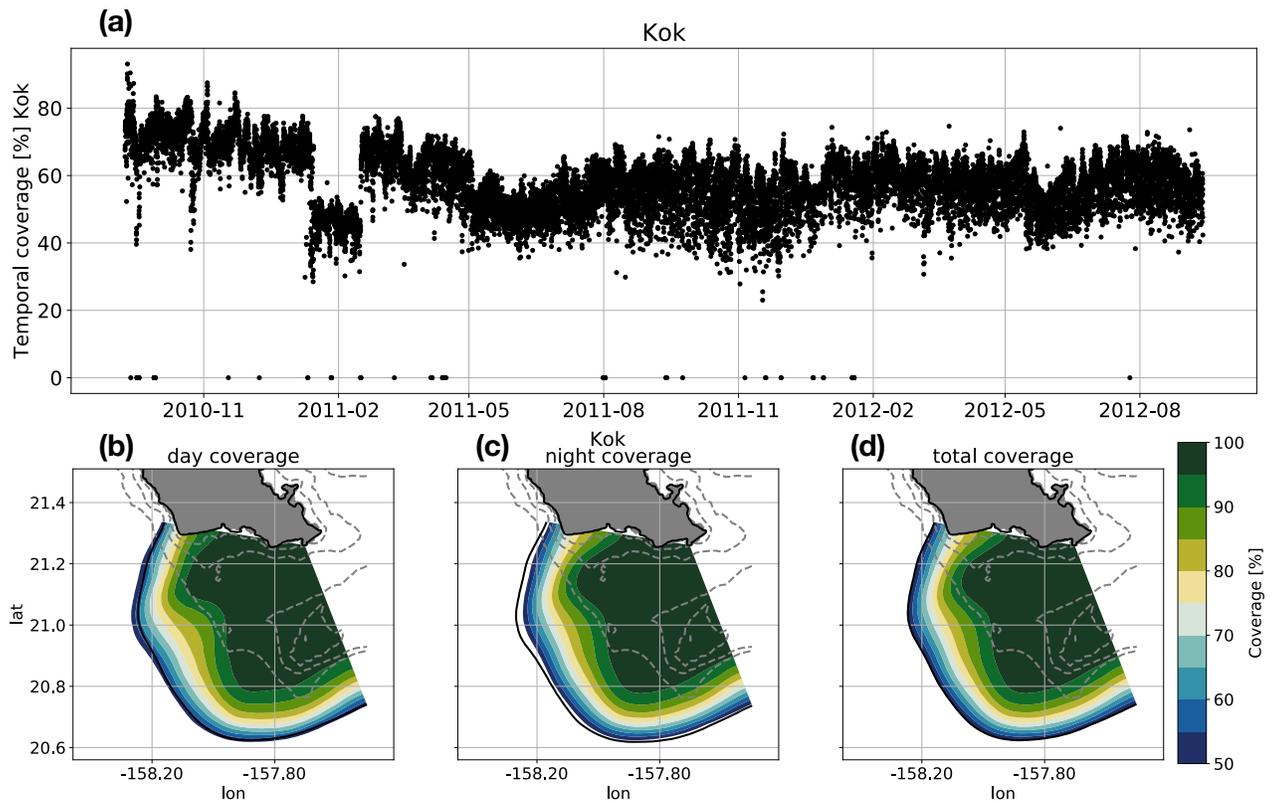
Figure 5.7: KOK (a) Time series of the percentage of spatial coverage of the area shown in (b) for the period of data available from November 2010 to August 2012. Colormaps of (b) daily (6:00 to 16:00) (c) nightly (16:00 to 6:00) and (d) total percentage of available data from November 2010 to August 2012.
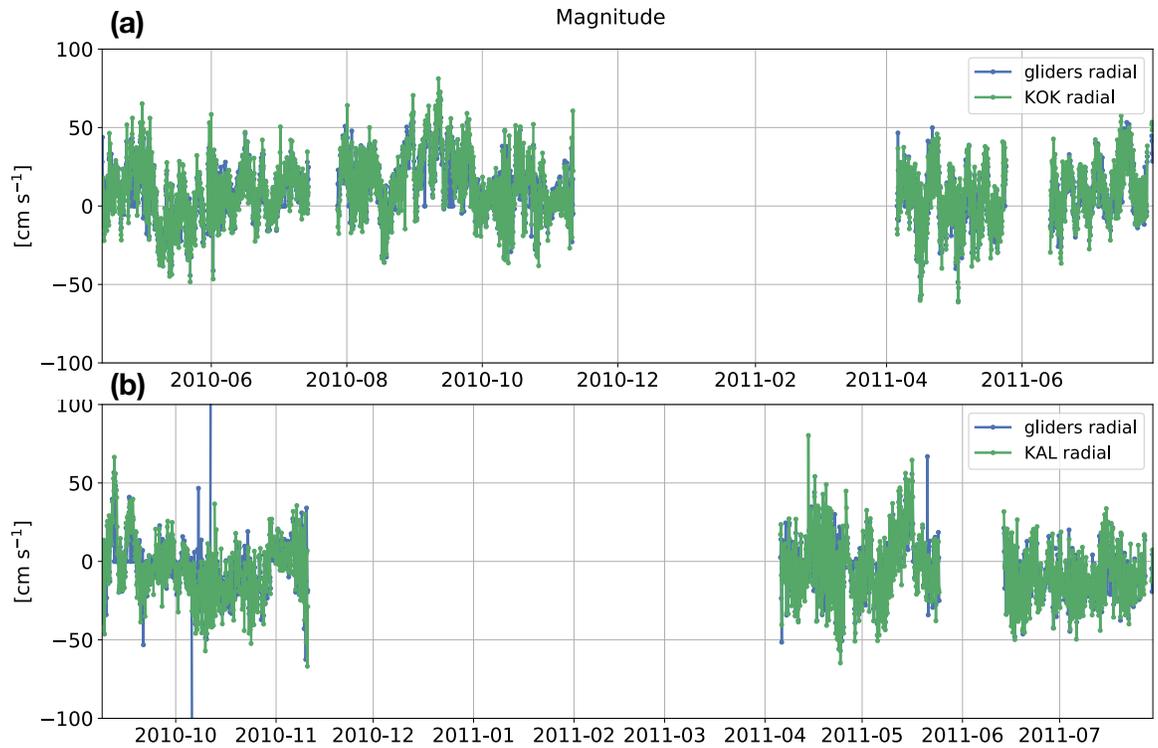
Figure 5.8: Time series of magnitude of surface velocities using gliders and (a) KOK and (b) KAL radial measurements. The radial surface velocities plotted are chosen as the closest radial grid point to the glider location when measured simultaneously.
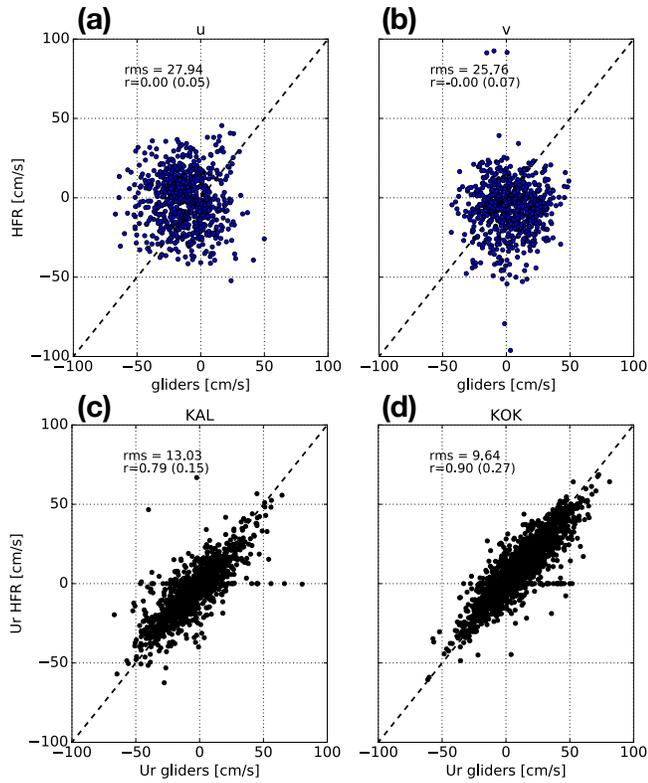
Figure 5.9: Scatter plots of gliders vs HFR (a) zonal and (b) meridional surface velocities and glider velocities projected into the (c) KAL and (d) KOK radial components vs the corresponding HFR radial velocities.

135
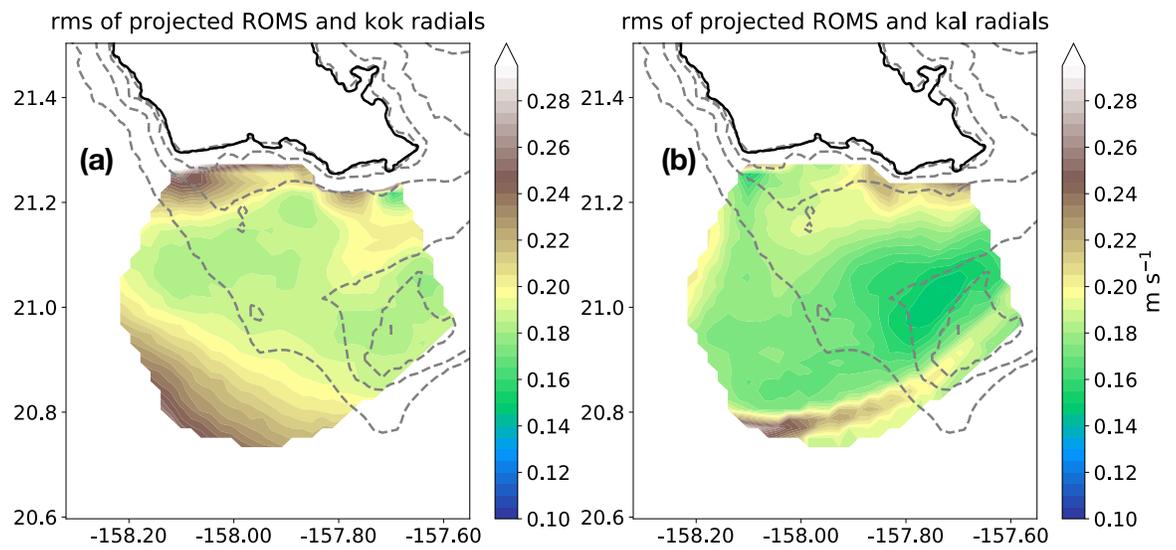
Figure 5.10: RMSD of ROMS radial currents projected into (a) KOK radials and (b) KAL radials vs the corresponding HFR radial velocities.
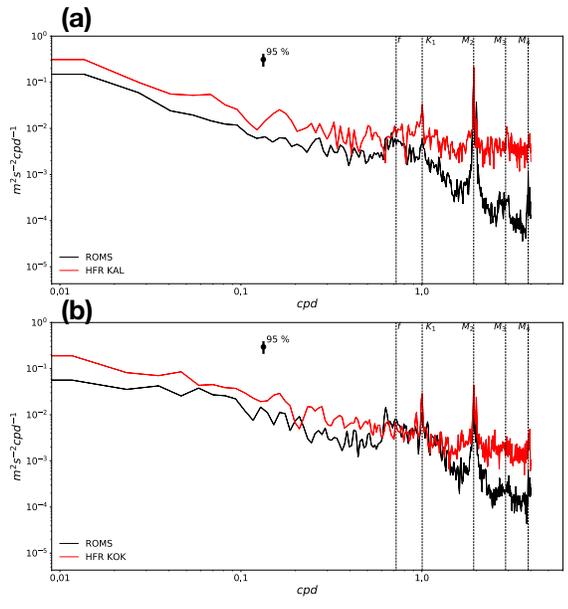
Figure 5.11: Spectra of (a) KAL and (b) KOK radial currents at the grid points with the lowest RMSD value in Figure 5.10. The black line in both figures denotes the ROMS spectra of the projected radial into the KAL and KOK radial respectively.
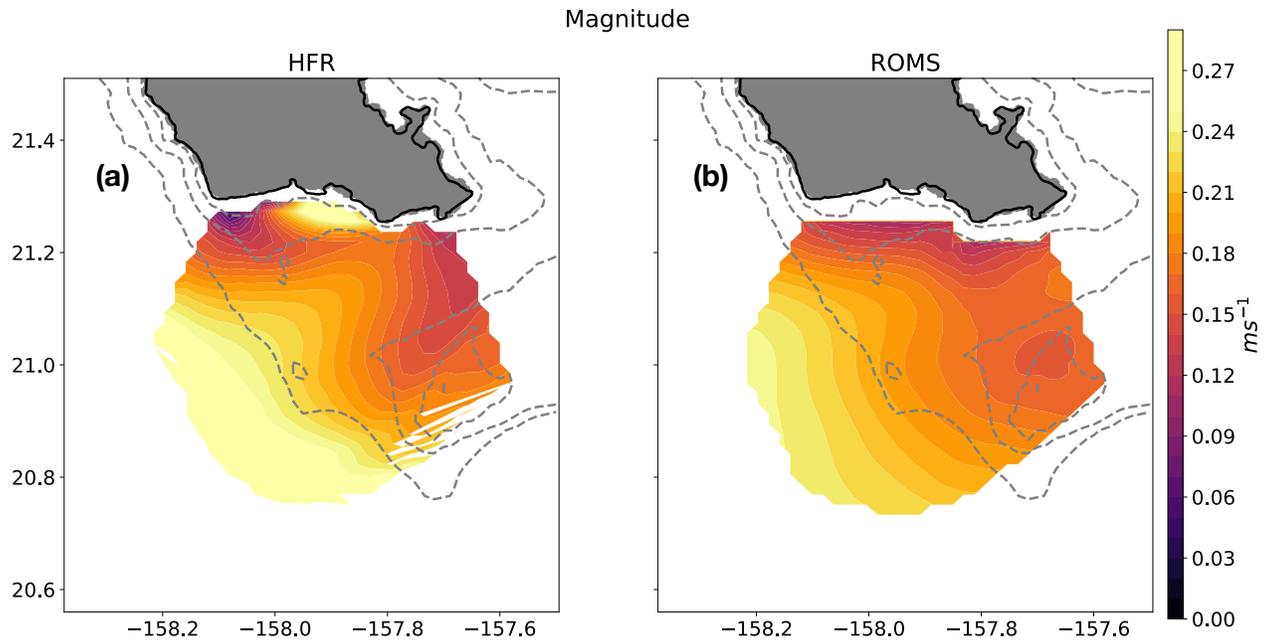
Figure 5.12: Time-averaged surface current magnitude from September 2010 to September 2012 computed using (a) HFRs and (b) ROMS vector currents interpolated into the HFR grid points.
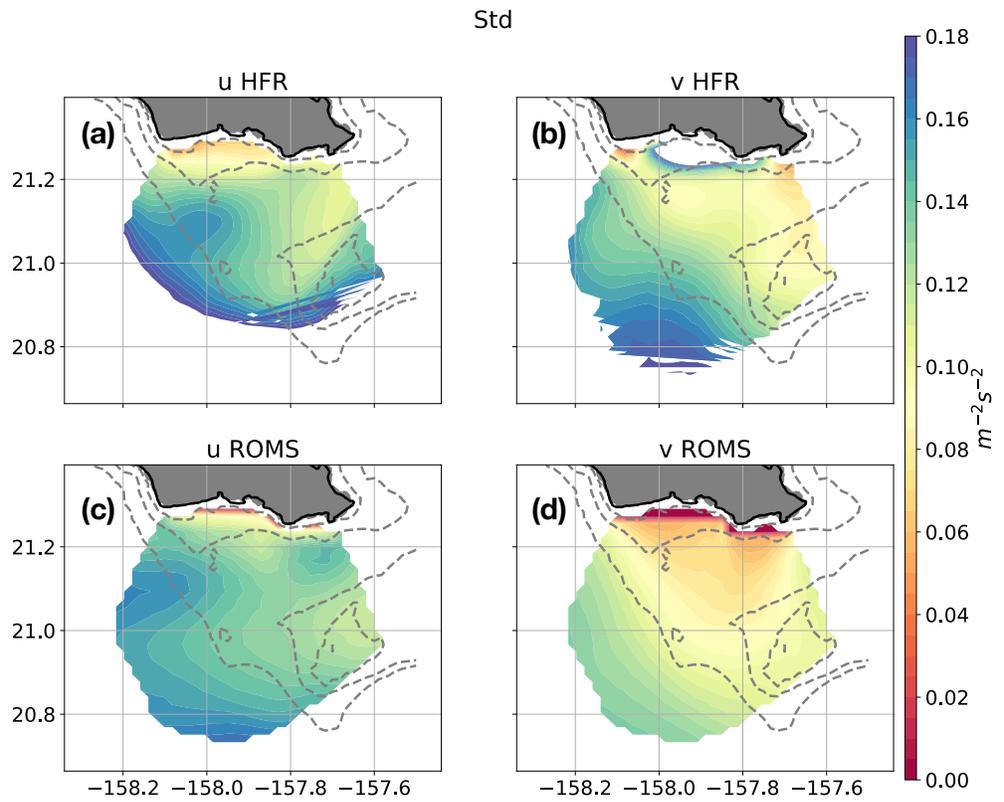
Figure 5.13: Standard deviation of (a) **u** and (b) **v** HFR surface velocities and (c) **u** and (d) **v** ROMS surface velocities interpolated into the HFR grid points from September 2010 to September 2012.
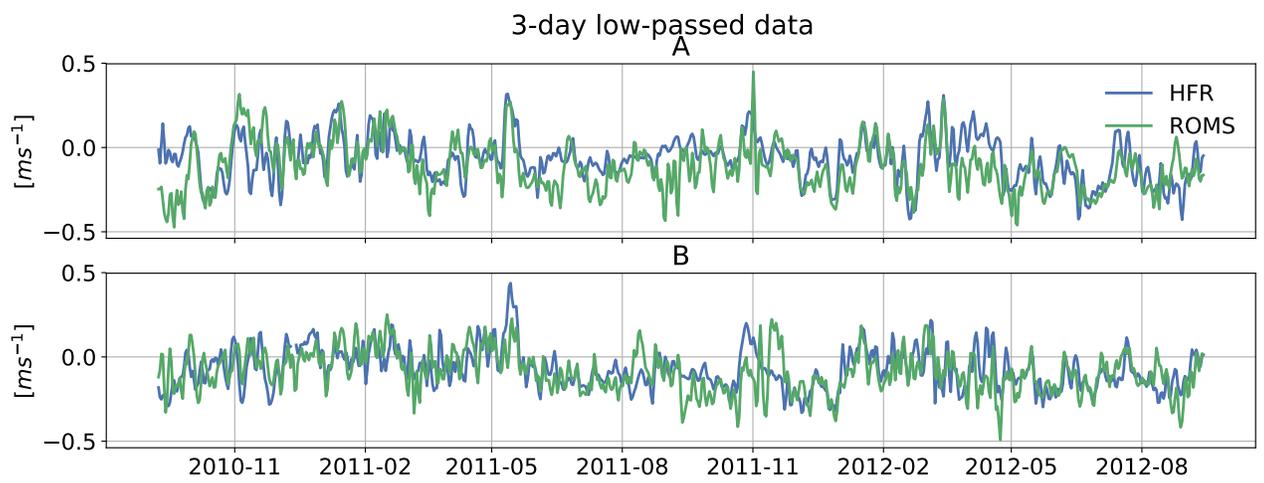
Figure 5.14: Time series of 3 day low pass **u** surface velocity averaged over regions A (top row) and (b) B (bottom row). Regions are depicted in Figure 1.1, Chapter 2.
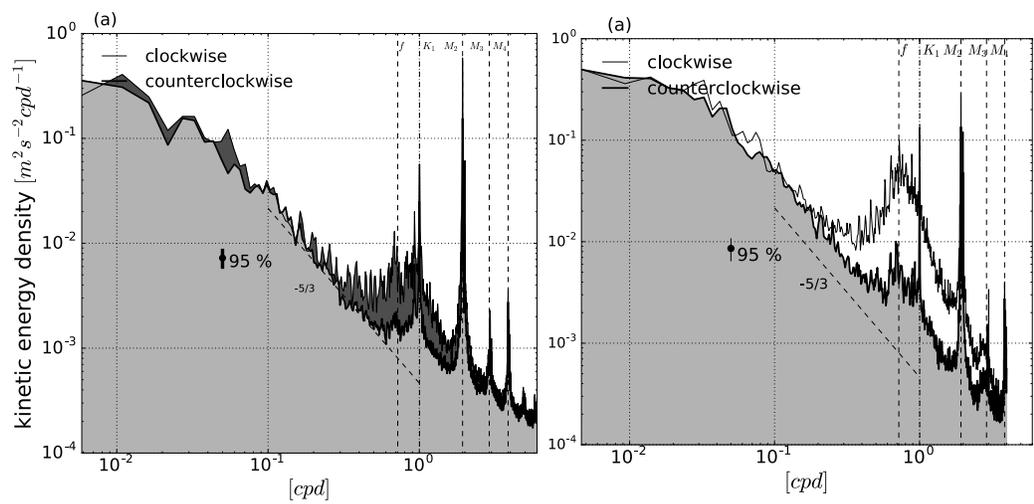
Figure 5.15: Clockwise and counterclockwise spectra of (a) HFR and (b) ROMS vector surface velocities averaged over the HFR effective coverage shown in Figure 5.1 as a black solid line.

CHAPTER 6
CONCLUSIONS

This thesis provided the first long-term time series study of submesoscale observations south shore of Oahu, Hawaii. HFR surface velocities alongside a ROMS implementation for the Hawaiian Archipelago allowed the exploration of ocean processes around the island of Oahu at spatial scales down to 1.5 km. The main outcomes of this dissertation are:

- The mean circulation off the south shore of Oahu Hawaii is characterized by the westward Hawaiian Lee Current (HLC) and the ocean responses to wind and bathymetry. The two-year mean surface vorticity budget was balanced by advection and stretching of vorticity. Bathymetry such as the 50 m Penguin Bank and wind stress curl due to the island chain blocking the trade winds modify the mean HLC.

- The spatial and temporal variability of Near Inertial Oscillations is dependent on the mean background flow and the wind. These variations can have an impact on the vertical propagation of Near Inertial Waves from the south shore of Oahu, thus modifying the energy budget between the mixed layer and the ocean interior.

- Barbers Point acts as a headland when the surface currents west coast of Oahu move southward, producing filaments of positive vorticity and vortices with Rossby numbers larger than 1. The submesoscale dynamics described here could potentially impact the biological production in Penguin Bank by increasing the supply of nutrients brought from the coastal advected submesoscale eddies. Figure 6.1 shows a map of satellite chlorophyll at the time where an eddy was observed in the HFR surface velocities. Chlorophyll at the eddy core is about two times larger than at its periphery. These routinely observed eddies could contribute to the "enhancement in phytoplankton near an island-reef ecosystem" or Island Mass Effect (IME) documented in Gove et al. (2016) around Hawaii.

- The main contributors of submesoscale ocean variability near a coast are still un-

known. In an open-ocean context, studies have shown it is dependent on baroclinic instabilities which grow according to the mixed layer depth. In a coastal-ocean context, this study has shown that it is dependent on barotropic instabilities, coastal circulation and mesoscale straining. Further studies are needed to understand the energy interactions between the submesoscale regime and larger scales flows. Longer HFR time series with spatial resolutions of at least 1 km are recommended for the island of Oahu alongside an implantation of ROMS with improved horizontal and vertical resolution at the ocean surface and bottom.

- Only instruments like HFR allow a more detail exploration of these submesoscale processes and their impact on the IME around islands.
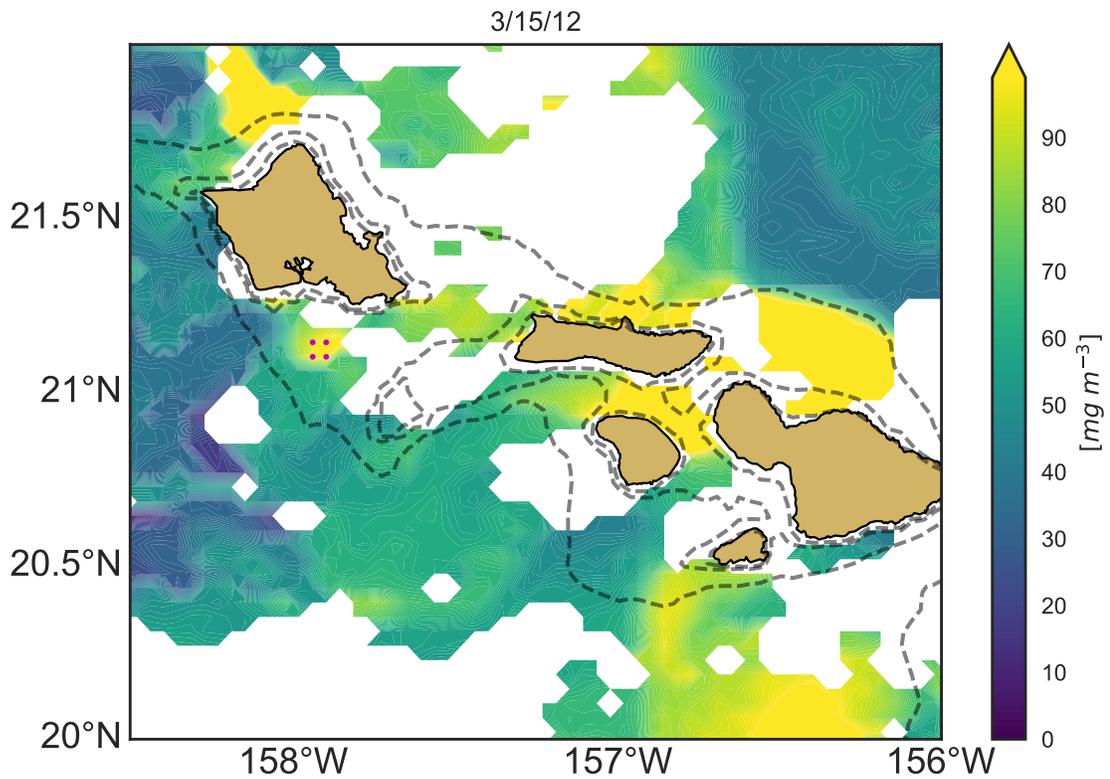
Figure 6.1: Daily satellite chlorophyll $[mg/m^3]$ on March 15, 2012. The magenta dots mark the area where the submesoscale eddy described in Chapter 4 is observed. Topography is shown in dashed grey contours at 50 m, 200 m and 1000 m.

Bibliography

ALFORD, M. H. 2003. Redistribution of energy available for ocean mixing by long-range propagation of internal waves. Nature **423**: 159–162.

ALFORD, M. H., AND M. C. GREGG. 2001. Near-inertial mixing: Modulation of shear, strain and. Journal of geophysical research **106**: 16–947.

ALFORD, M. H., AND M. WHITMONT. 2007. Seasonal and spatial variability of near-inertial kinetic energy from historical moored velocity records. Journal of Physical Oceanography **37**: 2022–2037.

AZEVEDO CORREIA DE SOUZA, J. M., B. POWELL, A. C. CASTILLO-TRUJILLO, AND P. FLAMENT. 2015. The vorticity balance of the ocean surface in Hawaii from a regional reanalysis. Journal of Physical Oceanography **45**: 424–440.

BRINK, K. H., AND J. ALLEN. 1978. On the effect of bottom friction on barotropic motion over the continental shelf. Journal of Physical Oceanography **8**: 919–922.

CALIL, P. H., K. J. RICHARDS, Y. JIA, AND R. R. BIDIGARE. 2008. Eddy activity in the lee of the Hawaiian Islands. Deep Sea Research Part II: Topical Studies in Oceanography **55**: 1179–1194.

CALLIES, J., R. FERRARI, J. M. KLYMAK, AND J. GULA. 2015. Seasonality in submesoscale turbulence. Nature communications **6**: 6862.

CAPET, X., J. C. MCWILLIAMS, M. J. MOLEMAKER, AND A. SHCHEPETKIN. 2008. Mesoscale to submesoscale transition in the California Current System. Part I: Flow structure, eddy flux, and observational tests. Journal of physical oceanography **38**: 29–43.

CASTILLO-TRUJILLO, A. 2014. Low frequency currents south of Oahu, Hawaii. Master. thesis. Sch. of Ocean and Earth Sci. and Technol. Univ. of Hawaii at Manoa p. 56.

CHARNEY, J. G. 1971. Geostrophic turbulence. Journal of the Atmospheric Sciences **28**: 1087–1095.

CHAVANNE, C., P. FLAMENT, R. LUMPKIN, B. DOUSSET, AND A. BENTAMY. 2002. Scatterometer observations of wind variations induced by oceanic islands: Implications for wind-driven ocean circulation. Canadian Journal of Remote Sensing **28**: 466–474.

CHAVANNE, C., I. JANEKOVIĆ, P. FLAMENT, P.-M. POULAIN, M. KUZMIĆ, AND K.-W. GURGEL. 2007. Tidal currents in the northwestern Adriatic: High-frequency radio observations and numerical model predictions. Journal of Geophysical Research: Oceans (1978–2012) **112**.

CHAVANNE, C., P. FLAMENT, G. CARTER, M. MERRIFIELD, D. LUTHER, E. ZARON, AND K. GURGEL. 2010a. The Surface Expression of Semidiurnal Internal Tides near a Strong Source at Hawaii. Part I: Observations and Numerical Predictions*. Journal of Physical Oceanography **40**: 1155–1179.

CHAVANNE, C., P. FLAMENT, AND K.-W. GURGEL. 2010b. Interactions between a Submesoscale Anticyclonic Vortex and a Front. Journal of Physical Oceanography **40**: 1802–1818.

CHAVANNE, C. P., E. FIRING, AND F. ASCANI. 2012. Inertial oscillations in geostrophic flow: is the inertial frequency shifted by $\zeta/2$ or by ζ? Journal of Physical Oceanography **42**: 884–888.

CHERESKIN, T., M. D. LEVINE, A. HARDING, AND L. REGIER. 1989. Observations of near-inertial waves in acoustic Doppler current profiler measurements made during the Mixed Layer Dynamics Experiment. Journal of Geophysical Research: Oceans **94**: 8135–8145.

CSANADY, G. 1978. The arrested topographic wave. Journal of Physical Oceanography **8**: 47–62.

DANIOUX, E., P. KLEIN, AND P. RIVIÈRE. 2008. Propagation of wind energy into the deep ocean through a fully turbulent mesoscale eddy field. Journal of Physical Oceanography **38**: 2224–2241.

D'ASARO, E. A. 1985. The energy flux from the wind to near-inertial motions in the surface mixed layer. Journal of Physical Oceanography **15**: 1043–1059.

D'ASARO, E. A. 1995*a*. Upper-ocean inertial currents forced by a strong storm. Part II: Modeling. Journal of physical oceanography **25**: 2937–2952.

D'ASARO, E. A. 1995*b*. Upper-ocean inertial currents forced by a strong storm. Part III: Interaction of inertial currents and mesoscale eddies. Journal of physical oceanography **25**: 2953–2958.

D'ASARO, E. A., C. C. ERIKSEN, M. D. LEVINE, C. A. PAULSON, P. NIILER, AND P. VAN MEURS. 1995. Upper-ocean inertial currents forced by a strong storm. Part I: Data and comparisons with linear theory. Journal of Physical Oceanography **25**: 2909–2936.

DAUHAJRE, D. P., J. C. MCWILLIAMS, AND Y. UCHIYAMA. 2017. Submesoscale Coherent Structures on the Continental Shelf. Journal of Physical Oceanography **47**: 2949–2976.

DE BOYER MONTÉGUT, C., G. MADEC, A. S. FISCHER, A. LAZAR, AND D. IUDICONE. 2004. Mixed layer depth over the global ocean: An examination of profile data and a profile-based climatology. Journal of Geophysical Research: Oceans (1978–2012) **109**.

DRITSCHEL, D., P. HAYNES, M. JUCKES, AND T. SHEPHERD. 1991. The stability of a two-dimensional vorticity filament under uniform strain. Journal of Fluid Mechanics **230**: 647–665.

EGBERT, G. D., AND S. Y. EROFEEVA. 2002. Efficient inverse modeling of barotropic ocean tides. Journal of Atmospheric and Oceanic Technology **19**: 183–204.

EICH, M. L., M. A. MERRIFIELD, AND M. H. ALFORD. 2004. Structure and variability of semidiurnal internal tides in Mamala Bay, Hawaii. Journal of Geophysical Research: Oceans **109**.

ELIPOT, S., R. LUMPKIN, AND G. PRIETO. 2010. Modification of inertial oscillations by the mesoscale eddy field. Journal of Geophysical Research: Oceans **115**.

ERIKSEN, C. C., T. J. OSSE, R. D. LIGHT, T. WEN, T. W. LEHMAN, P. L. SABIN, J. W. BALLARD, AND A. M. CHIODI. 2001. Seaglider: A long-range autonomous underwater vehicle for oceanographic research. IEEE Journal of oceanic Engineering **26**: 424–436.

FERRARI, R., AND C. WUNSCH. 2009. Ocean circulation kinetic energy: Reservoirs, sources, and sinks. Annual Review of Fluid Mechanics **41**.

FERRARI, R., AND C. WUNSCH. 2010. The distribution of eddy kinetic and potential energies in the global ocean. Tellus A **62**: 92–108.

FIRING, E., R.-C. LIEN, AND P. MULLER. 1997. Observations of strong inertial oscillations after the passage of tropical cyclone Ofa. Journal of Geophysical Research: Oceans **102**: 3317–3322.

FRANKS, P. J. 1995. Thin layers of phytoplankton: a model of formation by near-inertial wave shear. Deep Sea Research Part I: Oceanographic Research Papers **42**: 75–91.

FU, L.-L. 1981. Observations and models of inertial waves in the deep ocean. Reviews of Geophysics **19**: 141–170.

GOUGH, M. K., N. GARFIELD, AND E. MCPHEE-SHAW. 2010. An analysis of HF radar measured surface currents to determine tidal, wind-forced, and seasonal circulation in the Gulf of the Farallones, California, United States. Journal of Geophysical Research: Oceans (1978–2012) **115**.

GOVE, J. M., M. A. MCMANUS, A. B. NEUHEIMER, J. J. POLOVINA, J. C. DRAZEN, C. R. SMITH, M. A. MERRIFIELD, A. M. FRIEDLANDER, J. S. EHSES, C. W.

YOUNG, ET AL. 2016. Near-island biological hotspots in barren ocean basins. Nature communications **7**: 10581.

GULA, J., M. J. MOLEMAKER, AND J. C. MCWILLIAMS. 2014. Submesoscale cold filaments in the Gulf Stream. Journal of Physical Oceanography **44**: 2617–2643.

GULA, J., M. MOLEMAKER, AND J. MCWILLIAMS. 2015. Topographic vorticity generation, submesoscale instability and vortex street formation in the Gulf Stream. Geophysical Research Letters **42**: 4054–4062.

GULA, J., M. J. MOLEMAKER, AND J. C. MCWILLIAMS. 2016. Submesoscale dynamics of a Gulf Stream frontal eddy in the South Atlantic Bight. Journal of Physical Oceanography **46**: 305–325.

GURGEL, K.-W., G. ANTONISCHKI, H.-H. ESSEN, AND T. SCHLICK. 1999*a*. Wellen Radar (WERA): a new ground-wave HF radar for ocean remote sensing. Coastal Engineering **37**: 219–234.

GURGEL, K.-W., H.-H. ESSEN, AND S. KINGSLEY. 1999*b*. High-frequency radars: physical limitations and recent developments. Coastal Engineering **37**: 201–218.

HAIDVOGEL, D. B., J. C. MCWILLIAMS, AND P. R. GENT. 1992. Boundary current separation in a quasigeostrophic, eddy-resolving ocean circulation model. Journal of Physical Oceanography **22**: 882–902.

HARRISON, D., AND A. ROBINSON. 1978. Energy analysis of open regions of turbulent flows. Mean eddy energetics of a numerical ocean circulation experiment. Dynamics of Atmospheres and Oceans **2**: 185–211.

HUGHES, C. W. 2005. Nonlinear vorticity balance of the Antarctic Circumpolar Current. Journal of Geophysical Research: Oceans (1978–2012) **110**.

JANEKOVIĆ, I., B. POWELL, D. MATTHEWS, M. MCMANUS, AND J. SEVADJIAN. 2013.

4D-Var data assimilation in a nested, coastal ocean model: A Hawaiian case study. Journal of Geophysical Research: Oceans **118**: 5022–5035.

JING, Z., L. WU, AND X. MA. 2016. Energy Exchange between the Mesoscale Oceanic Eddies and Wind-Forced Near-Inertial Oscillations. Journal of Physical Oceanography .

JING, Z., L. WU, AND X. MA. 2017. Energy Exchange between the Mesoscale Oceanic Eddies and Wind-Forced Near-Inertial Oscillations. Journal of Physical Oceanography **47**: 721–733.

JOCHUM, M., B. P. BRIEGLEB, G. DANABASOGLU, W. G. LARGE, N. J. NORTON, S. R. JAYNE, M. H. ALFORD, AND F. O. BRYAN. 2013. The impact of oceanic near-inertial waves on climate. Journal of Climate **26**: 2833–2844.

KARL, D. M., AND R. LUKAS. 1996. The Hawaii Ocean Time-series (HOT) program: Background, rationale and field implementation. Deep Sea Research Part II: Topical Studies in Oceanography **43**: 129–156.

KIM, S. Y., AND P. M. KOSRO. 2013. Observations of near-inertial surface currents off Oregon: Decorrelation time and length scales. Journal of Geophysical Research: Oceans **118**: 3723–3736.

KIM, S. Y., P. M. KOSRO, AND A. L. KURAPOV. 2014. Evaluation of directly wind-coherent near-inertial surface currents off Oregon using a statistical parameterization and analytical and numerical models. Journal of Geophysical Research: Oceans **119**: 6631–6654.

KIM, S. Y., A. L. KURAPOV, AND P. M. KOSRO. 2015. Influence of varying upper ocean stratification on coastal near-inertial currents. Journal of Geophysical Research: Oceans **120**: 8504–8527.

KIM, S. Y., J. G. YOO, AND H. S. KIM. 2017. Spectral descriptions of submesoscale surface circulation in a coastal region off the East Coast of Korea, p. 44. *In* EGU General Assembly Conference Abstracts, vol. 19.

Kiss, A. E. 2002. Potential vorticity. Journal of marine research **60**: 779–803.

Klein, P., B. L. Hua, and X. Carton. 2003. Emergence of cyclonic structures due to the interaction between near-inertial oscillations and mesoscale eddies. Quarterly Journal of the Royal Meteorological Society **129**: 2513–2525.

Klein, P., S. L. Smith, and G. Lapeyre. 2004. Organization of near-inertial energy by an eddy field. Quarterly Journal of the Royal Meteorological Society **130**: 1153–1166.

Klein, P., J. Isern-Fontanet, G. Lapeyre, G. Roullet, E. Danioux, B. Chapron, S. Le Gentil, and H. Sasaki. 2009. Diagnosis of vertical velocities in the upper ocean from high resolution sea surface height. Geophysical Research Letters **36**.

Kunze, E. 1985. Near-inertial wave propagation in geostrophic shear. Journal of Physical Oceanography **15**: 544–565.

Kunze, E., and T. B. Sanford. 1984. Observations of near-inertial waves in a front. Journal of physical oceanography **14**: 566–581.

Kunze, E., and T. B. Sanford. 1986. Near-inertial wave interactions with mean flow and bottom topography near Caryn Seamount. Journal of physical oceanography **16**: 109–120.

LaCasce, J., O. Nøst, and P. Isachsen. 2008. Asymmetry of free circulations in closed ocean gyres. Journal of Physical Oceanography **38**: 517–526.

Lapeyre, G., and P. Klein. 2006. Impact of the small-scale elongated filaments on the oceanic vertical pump. Journal of marine research **64**: 835–851.

Large, W., and S. Pond. 1981. Open ocean momentum flux measurements in moderate to strong winds. Journal of physical oceanography **11**: 324–336.

Lipa, B., and D. Barrick. 1983. Least-squares methods for the extraction of surface currents from CODAR crossed-loop data: Application at ARSLOE. Oceanic Engineering, IEEE Journal of **8**: 226–253.

Lucas, A. J., G. C. Pitcher, T. A. Probyn, and R. M. Kudela. 2014. The influence of diurnal winds on phytoplankton dynamics in a coastal upwelling system off southwestern Africa. Deep Sea Research Part II: Topical Studies in Oceanography **101**: 50–62.

Lumpkin, C. 1998. Eddies an currents of the Hawaiian Islands. Ph.D. thesis. Sch. of Ocean and Earth Sci. and Technol. Univ. of Hawaii at Manoa p. 282.

Lumpkin, R., and P. J. Flament. 2013. Extent and Energetics of the Hawaiian Lee Countercurrent. Oceanography **26**: 58–65.

Mahadevan, A., and A. Tandon. 2006. An analysis of mechanisms for submesoscale vertical motion at ocean fronts. Ocean Modelling **14**: 241–256.

Matthews, D., B. Powell, and I. Janeković. 2012. Analysis of four-dimensional variational state estimation of the Hawaiian waters. Journal of Geophysical Research: Oceans (1978–2012) **117**.

McWilliams, J. C. 2016. Submesoscale currents in the ocean. Proc. R. Soc. A **472**: 20160117.

McWilliams, J. C., I. Yavneh, M. J. Cullen, and P. R. Gent. 1998. The breakdown of large-scale flows in rotating, stratified fluids. Physics of Fluids **10**: 3178–3184.

Mensa, J., M.-L. Timmermans, I. Kozlov, W. Williams, and T. Özgökmen. 2018. Surface Drifter Observations From the Arctic Ocean's Beaufort Sea: Evidence for Submesoscale Dynamics. Journal of Geophysical Research: Oceans .

Millot, C., and M. Crépon. 1981. Inertial oscillations on the continental shelf of the Gulf of Lions; Observations and theory. Journal of Physical Oceanography **11**: 639–657.

Molemaker, M. J., J. C. McWilliams, and W. K. Dewar. 2015. Submesoscale instability and generation of mesoscale anticyclones near a separation of the California Undercurrent. Journal of Physical Oceanography **45**: 613–629.

Niiler, P. P. 1975. Deepening of the wind-mixed layer. J. mar. Res **33**: 405–421.

Paduan, J. D., and H. C. Graber. 1997. Introduction to high-frequency radar: reality and myth. Oceanography **10**: 36–39.

Pawlowicz, R., B. Beardsley, and S. Lentz. 2002. Classical tidal harmonic analysis including error estimates in MATLAB using T_TIDE. Computers & Geosciences **28**: 929–937.

Pedlosky, J. 1987. Geophysical fluid mechanics.

Pettigrew, N. R. 1981. The dynamics and kinematics of the coastal boundary layer off Long Island. Ph.D. thesis, Massachusetts Institute of Technology.

Plueddemann, A., and J. Farrar. 2006. Observations and models of the energy flux from the wind to mixed-layer inertial currents. Deep Sea Research Part II: Topical Studies in Oceanography **53**: 5–30.

Pollard, R. 1980. Properties of near-surface inertial oscillations. Journal of Physical Oceanography **10**: 385–398.

Pollard, R. T., and R. Millard Jr. 1970. Comparison between observed and simulated wind-generated inertial oscillations, pp. 813–821. *In* Deep Sea Research and Oceanographic Abstracts, vol. 17. Elsevier.

Powell, B., A. Moore, H. Arango, E. Di Lorenzo, R. Milliff, and R. Leben. 2009. Near real-time ocean circulation assimilation and prediction in the Intra-Americas Sea with ROMS. Dynamics of Atmospheres and Oceans **48**: 46–68.

Price, J. F., R. A. Weller, and R. Pinkel. 1986. Diurnal cycling: Observations and models of the upper ocean response to diurnal heating, cooling, and wind mixing. Journal of Geophysical Research: Oceans **91**: 8411–8427.

Rhines, P. 1998. Circulation, Covection and Mixing in Rotating, Stratified Basins with Sloping Topography. Physical processes in lakes and oceans pp. 209–226.

RICHMAN, J. G., B. K. ARBIC, J. F. SHRIVER, E. J. METZGER, AND A. J. WALLCRAFT. 2012. Inferring dynamics from the wavenumber spectra of an eddying global ocean model with embedded tides. Journal of Geophysical Research: Oceans **117**.

ROCHA, C. B., T. K. CHERESKIN, S. T. GILLE, AND D. MENEMENLIS. 2016. Mesoscale to submesoscale wavenumber spectra in Drake Passage. Journal of Physical Oceanography **46**: 601–620.

RÖHRS, J., A. K. SPERREVIK, K. H. CHRISTENSEN, G. BROSTRÖM, AND Ø. BREIVIK. 2015. Comparison of HF radar measurements with Eulerian and Lagrangian surface currents. Ocean Dynamics **65**: 679–690.

SHCHEPETKIN, A. F., AND J. C. MCWILLIAMS. 2005. The regional oceanic modeling system (ROMS): a split-explicit, free-surface, topography-following-coordinate oceanic model. Ocean Modelling **9**: 347–404.

SHCHERBINA, A. Y., E. A. D'ASARO, C. M. LEE, J. M. KLYMAK, M. J. MOLEMAKER, AND J. C. MCWILLIAMS. 2013. Statistics of vertical vorticity, divergence, and strain in a developed submesoscale turbulence field. Geophysical Research Letters **40**: 4706–4711.

SHEARMAN, R. K. 2005. Observations of near-inertial current variability on the New England shelf. Journal of Geophysical Research: Oceans **110**.

SMITH, J. A. 2008. Vorticity and divergence of surface velocities near shore. Journal of Physical Oceanography **38**: 1450–1468.

SOARES, S., A. NATAROV, AND K. RICHARDS. 2016. Internal swells in the tropics: Near-inertial wave energy fluxes and dissipation during CINDY. Journal of Geophysical Research: Oceans **121**: 3297–3324.

SOH, H. S., AND S. Y. KIM. 2018. Diagnostic characteristics of submesoscale coastal surface currents. Journal of Geophysical Research: Oceans .

SOH, H. S., S. Y. KIM, P. M. KOSRO, AND A. L. KURAPOV. 2018. Do non-orthogonally and irregularly sampled scalar velocities contain sufficient information to reconstruct an orthogonal vector current field? Journal of Atmospheric and Oceanic Technology .

STERN, M. E. 1965. Interaction of a uniform wind stress with a geostrophic vortex, pp. 355–367. *In* Deep Sea Research and Oceanographic Abstracts, vol. 12. Elsevier.

STERN, M. E. 1975. Ocean circulation physics. Academic Press, Inc.

STEWART, R. H., AND J. W. JOY. 1974. HF radio measurements of surface currents, pp. 1039–1049. *In* Deep Sea Research and Oceanographic Abstracts, vol. 21. Elsevier.

THOMAS, L. N., A. TANDON, AND A. MAHADEVAN. 2008. Submesoscale processes and dynamics. Ocean modeling in an Eddying Regime pp. 17–38.

THOMSON, R. E., AND H. J. FREELAND. 2003. Topographic steering of a mid-depth drifter in an eddy-like circulation region south and east of the Hawaiian Ridge. Journal of Geophysical Research: Oceans **108**.

TORRENCE, C., AND G. P. COMPO. 1998. A practical guide to wavelet analysis. Bulletin of the American Meteorological society **79**: 61–78.

TU, C.-C., AND Y.-L. CHEN. 2011. Favorable conditions for the development of a heavy rainfall event over Oahu during the 2006 wet period. Weather and Forecasting **26**: 280–300.

VALLIS, G. K. 2006. Atmospheric and oceanic fluid dynamics: fundamentals and large-scale circulation. Cambridge University Press.

VAN MEURS, P. 1998. Interactions between near-inertial mixed layer currents and the mesoscale: The importance of spatial variabilities in the vorticity field. Journal of physical oceanography **28**: 1363–1388.

WELLER, R. A. 1982. The relation of near-inertial motions observed in the mixed layer during the JASIN (1978) experiment to the local wind stress and to the quasi-geostrophic flow field. Journal of Physical Oceanography **12**: 1122–1136.

WELLER, R. A. 1985. Near-surface velocity variability at inertial and subinertial frequencies in the vicinity of the California current. Journal of physical oceanography **15**: 372–385.

WHITT, D. B., AND L. N. THOMAS. 2015. Resonant generation and energetics of wind-forced near-inertial motions in a geostrophic flow. Journal of Physical Oceanography **45**: 181–208.

WUNSCH, C. 2013. Baroclinic motions and energetics as measured by altimeters. Journal of Atmospheric and Oceanic Technology **30**: 140–150.

YANG, B., AND Y. HOU. 2014. Near-inertial waves in the wake of 2011 Typhoon Nesat in the northern South China Sea. Acta Oceanologica Sinica **33**: 102–111.

YOSHIDA, S., B. QIU, AND P. HACKER. 2011. Low-frequency eddy modulations in the Hawaiian Lee Countercurrent: Observations and connection to the Pacific Decadal Oscillation. Journal of Geophysical Research: Oceans (1978–2012) **116**.

YOUNG, W., AND M. B. JELLOUL. 1997. Propagation of near-inertial oscillations through a geostrophic flow. Journal of marine research **55**: 735–766.